

University of Warwick institutional repository: <http://go.warwick.ac.uk/wrap>

A Thesis Submitted for the Degree of PhD at the University of Warwick

<http://go.warwick.ac.uk/wrap/77687>

This thesis is made available online and is protected by original copyright.

Please scroll down to view the document itself.

Please refer to the repository record for this item for information to help you to cite it. Our policy information is available from the repository home page.

AUTHOR: **Francisco A. Calderon** DEGREE: **Ph.D.**

TITLE: **Non-linear Instabilities in the Edge of Tokamak Plasmas: Characterization of Edge Localized Modes and Numerical Simulation of Blob Dynamics using a Hybrid Model.**

DATE OF DEPOSIT:

I agree that this thesis shall be available in accordance with the regulations governing the University of Warwick theses.

I agree that the summary of this thesis may be submitted for publication.

I **agree** that the thesis may be photocopied (single copies for study purposes only).

Theses with no restriction on photocopying will also be made available to the British Library for microfilming. The British Library may supply copies to individuals or libraries. subject to a statement from them that the copy is supplied for non-publishing purposes. All copies supplied by the British Library will carry the following statement:

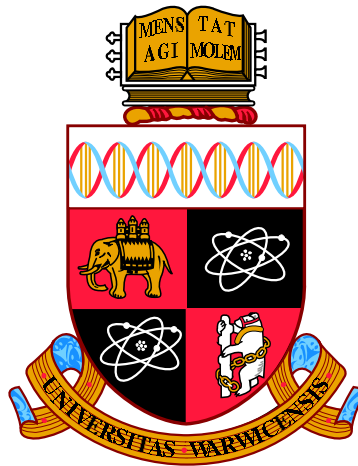
“Attention is drawn to the fact that the copyright of this thesis rests with its author. This copy of the thesis has been supplied on the condition that anyone who consults it is understood to recognise that its copyright rests with its author and that no quotation from the thesis and no information derived from it may be published without the author’s written consent.”

AUTHOR’S SIGNATURE:

USER’S DECLARATION

1. I undertake not to quote or make use of any information from this thesis without making acknowledgement to the author.
2. I further undertake to allow no-one else to use this thesis while it is in my care.

DATE	SIGNATURE	ADDRESS
.....
.....
.....
.....



**Non-linear Instabilities in the Edge of
Tokamak Plasmas: Characterization of
Edge Localized Modes and Numerical
Simulation of Blob Dynamics using a
Hybrid Model.**

by

Francisco A. Calderon

Thesis

Submitted to the University of Warwick

for the degree of

Doctor of Philosophy

Physics Department

September 2015

THE UNIVERSITY OF
WARWICK

Contents

Acknowledgements	iv
Declarations	vi
Abstract	viii
Chapter 1 Introduction	1
1.1 Motivation	1
1.2 Thesis overview	2
1.3 Fusion Energy	2
1.4 Plasma physics	5
1.4.1 Debye length	5
1.4.2 Plasma frequency	6
1.4.3 A fusion plasma	7
1.4.4 Single particle motion	8
1.4.5 Guiding centre drifts	12
1.4.6 Vlasov equation	13
1.4.7 Waves in a cold plasma	15
1.5 Tokamaks	18
1.6 Edge localized modes	24
1.6.1 L-H transition and ELMs	27
1.6.2 ELM measurements	27
1.7 Blobs and filaments	29
1.7.1 Sheath-limited model of blobs	31
1.7.2 Simulation of blobs	33

Chapter 2	Methods	37
2.1	Introduction	37
2.1.1	Standard test for linear signals	37
2.2	ELMs Methods	39
2.2.1	ELM detection	39
2.2.2	JET data system	46
2.3	Hybrid Simulation Methods	47
2.3.1	Introduction	47
2.3.2	Equations system and approximations	47
2.3.3	Normalization	51
2.3.4	Numerical scheme	52
2.3.5	Current Advance Method	55
2.3.6	Cyclic Leapfrog	57
2.3.7	Particle loading	60
2.3.8	Stability and CFL condition	61
Chapter 3	Characterization of ELMs in JET plasmas	64
3.1	Parameter space and dimensionality	64
3.2	Characterization of ELMs in low dimensional space	66
3.2.1	Results and discussion	68
3.2.2	Conclusions	74
Chapter 4	Modelling and evolution of Blob dynamics	76
4.1	Introduction	76
4.2	Hybrid model	77
4.2.1	Initial conditions: plasma parameters	77
4.2.2	Blob Initialization	78
4.3	Results	82
4.3.1	Simulations of filaments in 3D	84
4.3.2	Simulation of blob dynamics in 2D	90
4.4	Conclusions	94
Chapter 5	Conclusions	96
5.1	Conclusions of ELMs analysis	96
5.2	Conclusions of blob simulations	97

Appendix	98
Appendix A The next step for fusion: ITER	99
List of Figures	102

Acknowledgements

I am very thankful to Sandra Chapman and Richard Dendy for their kind supervision during my PhD and all people partly involved in my doctoral training in the Centre for Fusion, Space, and Astrophysics of the physics department, at the University of Warwick. I also want to thank D. Burgess of the Queen Mary University of London, for providing the hybrid code used in this thesis.

I acknowledge the great efforts from both my supervisors to introduce me early on my career into full time plasma and fusion research. Increasing the scientific network through continued participation in conferences, summer schools, and seminars. I have embraced plasma physics as well as the warm welcome from the community and I will continue to offer my own contribution as long as time and health permits.

I am thankful to the many people who became my second family during the past twelve years, most of them have been fellows student during undergraduate, master and doctorate studies. Also, thanks to my beloved wife with whom sharing the dream was a lot of fun and that we came together to Warwick University and we both were PhD students along with the company of our smiley son. It has been a beautiful moment in our life that we have enjoyed and will remember fondly. This is the culmination of twelve years of continuous study, and yet it seems just the beginning. As I heard it once, ‘one must pay the price to talk physics and allow himself to venture into the deepest of mind’.

Finally, I want to thanks the friendship of Ersilia, Giuseppe, James and Leopoldo all from CFSA, also my friends in the Warwick world music group and specially to Ruairi for the lovely music and friendship. Nonetheless, thanks to those who have shared this journey with me, share a moment, and a smile and that they will have a special place in my heart forever.

Declarations

I declare that the work presented in this thesis is my own except where stated otherwise, and was carried out entirely at the University of Warwick, during the period October 2011 to September 2015, under the supervision of Sandra Chapman and Richard Dendy. The research reported here has not been submitted, either wholly or in part, in this or any other academic institution for admission to a higher degree. Some parts of the work reported here and other work not reported in this thesis have been published, as listed below:

Publications

- Calderon, F. A., R. O. Dendy, S. C. Chapman, A. J. Webster, B. Alper, R. M. Nicol, and JET EFDA Contributors. “Identifying low-dimensional dynamics in type-I edge-localised-mode processes in JET plasmas”. In: *Physics of Plasmas* **20**(4), 042306, (2013)
- Webster, A. J., R. O. Dendy, F. A. Calderon, S. C. Chapman, E. Delabie, D. Dodt, R. Felton, T. N. Todd, F. Maviglia, J. Morris, V. Riccardo, B. Alper, S. Brezinsek, P. Coad, J. Likonen, M. Rubel, and JET EFDA Contributors. “Time-resonant tokamak plasma edge instabilities?” In: *Plasma Physics and Controlled Fusion* **56**(7), p. 075017, (2014).
- Chapman, S. C., R. O. Dendy, T. N. Todd, N. W. Watkins, A. J. Web-

ster, F. A. Calderon, J. Morris, and JET EFDA Contributors. “Relationship of edge localized mode burst times with divertor flux loop signal phase in JET”. In: *Physics of Plasmas* **21**(6), 062302, (2014).

- Chapman, S. C., R. O. Dendy, T. N. Todd, N. W. Watkins, F. A. Calderon, J. Morris, and JET Contributors. “The global build-up to intrinsic edge localized mode bursts seen in divertor full flux loops in JET”. In: *Physics of Plasmas* **22**(7), 072506, (2015).

Copyright

All images reproduced from *www.iter.org* are used accordingly under the terms of use, section 2: ‘that technical images are provided for illustrative purposes only’. All the copyrighted material remain distributed under ITER’s site terms of use.

Abstract

Characterization of edge tokamak plasma instabilities by measuring emergent phenomena within a range of frequencies above the ion cyclotron frequency have been explored in two ways: using the inter-event waiting times of Edge Localized Modes (ELMs) occurrences in measured time series of JET plasmas and by performing 2D/3D simulations of filamentary structures dynamics using a hybrid model plasma description, i.e. kinetic ion particles and massless charge neutralizing electron fluid.

The analysis of ELMs time series using characteristic emission lines D_α of JET tokamak in otherwise similar plasmas was performed with only a minimal number of drivers such as the gas puffing rate. They have shown a key role in changing the underlying system mode cycle where a threshold value revealed its transition from single harmonic behaviour to a transitioning phase into a total lost of the state and born of a higher frequency resonant mode.

Hybrid simulations of blobs/filaments are performed in 2D/3D to observe the kinetic evolution of these plasma structures over several ion gyroperiods. Novel 3D simulations represent the first kinetic simulations of these structures along the parallel direction using a kinetic description. We have investigated the evolution and the internal density currents which provide insight of the effects of finite Larmor radius in the blobs dynamics and evolution.

Chapter 1

Introduction

1.1 Motivation

Nuclear fusion holds the potential for a reliable, long term, and clean power source. The amount of energy that fusion will produce will exceed by far the current capacity of fossil fuels, combined with any other green alternative [Freidberg, 2007]. It has been predicted that global energy demands will increase by one-third from 2010 to 2035, with China and India accounting for the 50% of the growth according to IEA [2011]. In addition, our demographic expansion is accompanied by an increase in energy consumption [Ongena and Oost, 2012], and therefore increasing the possibility of any near future energy shortage.

Fusion possess several benefits over traditional sources [Freidberg, 2007; Ongena and Oost, 2012]; and it will provide the energy needed as new technologies adapt and evolve for electrical consumption. Fusion also produces less toxic waste reducing the dangers attributed to fission energy. Every major fission disaster has left a strong public distrust. In 2011 after the ‘Energiewende’, Germany decided to bring to a complete stop all nuclear power plants by 2022 [WNA, 2015], with the immediate closure of eight reactors that year. The reasons motivating fusion development are many, and nowadays the field has evolved into a technology driven one with real impact for both science and society. More about the next generation fusion project, ITER, is given in Appendix A.

1.2 Thesis overview

The main focus of this thesis is to increase understanding of the edge phenomena in tokamak plasmas through the use of experimental data characterization and numerical simulations of the non-linear physics of edge instabilities. The main topic of discussion here is only a small proportion of the numerous instabilities seen in tokamak plasmas [Wesson, 2004]. There is a growing interest, spanning across theory and modelling, to use High Performance Computer (HPC) simulations and connect their results with data analysis of the measured phenomena [Pamela et al., 2011; Fenstermacher et al., 2013].

Since plasmas are required for the fusion process, we need to cover some basic concepts for plasmas in this chapter. In the following sections we will first discuss the concept of fusion energy, and some of the plasma most important definitions. Then, we describe single particle motion and drifts, and we continue with a brief description of the MHD waves in the cold plasma approximation. Subsequently, we define the tokamak most relevant concepts and the instabilities of interest for this thesis, introducing Edge Localized Modes (ELMs) [Zohm, 1996; Kamiya et al., 2007] and blob/filaments [Krasheninnikov et al., 2008; D'Ippolito et al., 2011], and their role in tokamak plasmas.

In Chapter 2 we explain the methods used to characterize the ELMs phenomenology, and the methods used to describe the blob/filament dynamics and their numerical evolution using particle-in-cell (PIC) with a Hybrid model of plasma. In Chapter 3 we present the results of the analyses in experimental data from the JET tokamak. In Chapter 4 we present the results of numerical simulations of general blob/filament plasma structures typically present in the edge of tokamak plasmas as well as other linear devices. Finally, in Chapter 5 a summary of the main results, conclusions, and suggestions for future work are given.

1.3 Fusion Energy

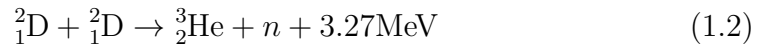
Fusion can be achieved through the use of a mixture of deuterium-deuterium gas (D-D) or deuterium-tritium (D-T) gas. The easiest fusion reaction to initiate is the D-T reaction [Freidberg, 2007]. This reaction releases 17.6 MeV in

energy or heat, converting with the Einstein energy relation, of which 14.1MeV is deposited in the neutron, and the other 3.5MeV in the alpha particle. One limitation of the D-T reaction is that tritium is not naturally available on Earth, and it has a half-life decay of 12.26 years. The reaction is as follows,



This is macroscopically equivalent to 338×10^6 MJ/kg. The D-T reaction is the central focus of the fusion research to achieve fusion energy. Experiments using D-T mixed plasma have been carried in TFTR [Strachan et al., 1997] and JET during the 1997 [Jacquinot et al., 1999; Thomas et al., 1998] and 2003 campaign, with a record energy in the 1997 campaign reaching a fusion power of 16.1 MW and Q (gain ratio) of 0.65. JET is currently under preparation for the next D-T campaign, schedule for start during the period 2017-18 [CCFE, 2014]. Although tritium is not easily found, there are some methods to obtain tritium, for instance, breeding tritium from lithium in the vessel walls or in divertor blankets.[Raffray et al., 2002].

Lets consider now the chemical reactions of the D-D plasma[Freidberg, 2007]. This is the most common plasma in current experiments and most of the research that exist is based on this reaction. The deuterium nuclei needs closer distances to overcome the Coulomb repulsive potential, and they require sufficiently high energies as well. The D-D reaction produces fusion energy via the nuclear interaction of two deuterium nuclei, from one of the following chemical reactions,



Probability distribution function

The averaged velocity cross-section of the nuclear reactions above can be estimated by using their thermal velocity distribution. First, we define the probability distribution function of particles as $f(\mathbf{x}, \mathbf{v}, t)$ with each ion species having its own distribution. Particularly in this case, we can describe both thermal deuterium and tritium with Maxwellian distribution of velocities as

follows,

$$f(\mathbf{x}_s, \mathbf{v}_s, t) = n(\mathbf{x}_s, t) \left(\frac{m_s}{2\pi T} \right)^{3/2} e^{-m_s v_s^2 / 2T} \quad (1.4)$$

here s denotes D or T and $n(\mathbf{x}_s, t)$ and T are the number density and temperature respectively, with $v^2 = v_x^2 + v_y^2 + v_z^2$. The following quantities: density and velocity are defined as moments of the probability distribution function, with a general expectation value $\langle W \rangle$ defined as follows,

$$n(\mathbf{x}, t) = \int f d\mathbf{v} \quad (1.5)$$

$$\mathbf{u}(\mathbf{x}, t) = \frac{1}{n} \int \mathbf{v} f d\mathbf{v} \quad (1.6)$$

$$\langle W \rangle = \frac{1}{n} \int W f d\mathbf{v} \quad (1.7)$$

We can finally evaluate the reaction rates R_{ij} using the following equation,

$$R_{ij} = \int f_i(\mathbf{v}_i) f_j(\mathbf{v}_j) \sigma_{ij}(|\mathbf{v}_j - \mathbf{v}_i|) |\mathbf{v}_j - \mathbf{v}_i| d\mathbf{v}_i d\mathbf{v}_j \quad (1.8)$$

so that,

$$R_{12} = n_1 n_2 \langle \sigma_{12} v \rangle \quad (1.9)$$

$$R_{11} = \frac{1}{2} n_1^2 \langle \sigma_{11} v \rangle \quad (1.10)$$

where R_{12} is the reaction rate for D-T, and R_{11} for D-D. The factor $1/2$ appears because in the integral over the two velocities v_1, v_2 each collision is counted twice. Assuming that the cross section $\sigma(v)$ is known, the reaction rate can be calculated. For a Maxwellian distribution (1.4) the values for $\langle \sigma v \rangle$ vs. T are illustrated in Fig. 1.1. We can observe that D-T has a peak value at $9 \times 10^{-22} \text{m}^3/\text{s}$ at a temperature of 70keV, much higher than that of D-D, or any other reaction. We can also see that the energy needed for a D-T plasma reaction is of the order of 70keV, which is more than a 1000 times the ionization factor making this gas fully ionized. Interestingly, the collisions in a power-balanced tokamak plasma will not necessarily need the peak value of $\langle \sigma v \rangle$, because most of the fusion reactions occur for particles on the tail of the distribution function resulting lower temperatures of the order of 15keV [Freidberg, 2007].

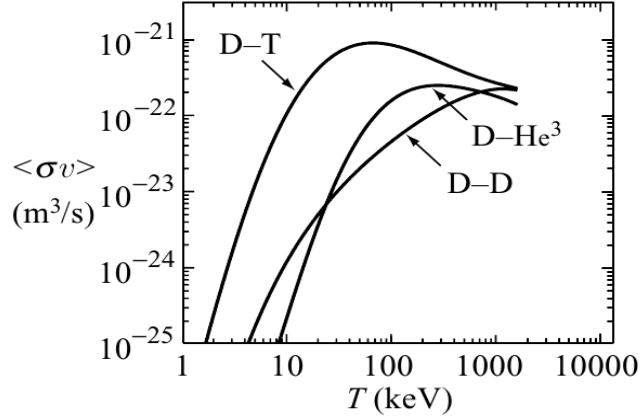


Figure 1.1: Velocity averaged cross section ($\langle \sigma v \rangle = R_{ij}/n_i n_j$) for the D-T, D-D, and D-He³ fusion reactions as a function of temperature, reproduced from Wesson [2004].

1.4 Plasma physics

A plasma is a gas of charged particles where the number of positive and negative particles are equally maintaining charge neutrality. It is also a hot and highly ionized gas. Because of the collective nature of plasma properties, such as quasi-neutrality, a plasma must contain a sufficient number of electrons within a spatial scale where the plasma behave in a stationary state and particles can interact.

1.4.1 Debye length

For a test charge Q , the electron cloud creates a sphere around the positive charge. Using the Boltzmann's equation, $n(E) = n_0 \exp(-E/k_B T)$, where k_B is the Boltzmann constant, n_0 is the particle number density, and T the temperature. The potential ϕ , that is produced by Q repels the ions and attract the electrons. The ion and electron densities are then described by,

$$n_i = n_0 e^{-e\phi/k_B T} \quad (1.11)$$

$$n_e = n_0 e^{e\phi/k_B T} \quad (1.12)$$

The charge density is then,

$$\rho = e(n_i - n_e) = -2n_0e \sinh(e\phi/k_BT) \quad (1.13)$$

Using Poisson's equation and $\mathbf{E} = -\nabla\phi$, with the charge density, we obtain,

$$\nabla^2\phi = \frac{2n_0e}{\varepsilon_0} \sinh(e\phi/k_BT) \quad (1.14)$$

Near the limit where the potential decreases up to $e\phi/k_BT \ll 1$ and we can approximate $\sinh(e\phi/k_BT) \approx e\phi/k_BT$. Eq. (1.14) is then,

$$\nabla^2\phi = -\frac{2}{\lambda_D^2}\phi \quad (1.15)$$

where λ_D is the Debye length,

$$\lambda_D = \left(\frac{\varepsilon_0 k_B T}{n_0 e^2} \right)^{1/2} \quad (1.16)$$

For typical parameters of a tokamak, see Table 1.1, $T = 1keV$, $n_0 = 10^{19}m^{-3}$, so that the Debye length is $7.4 \times 10^{-5}m$. Finally, the potential for the Debye shielding sphere is,

$$\phi = \frac{e}{4\pi\varepsilon_0 r} e^{-\sqrt{2}r/\lambda_D} \quad (1.17)$$

1.4.2 Plasma frequency

We also need to define another important plasma parameter, the plasma frequency. In a quasi neutral plasma, any perturbation creating a small charge separation d will give rise to a strong restoring force eE . The electrons have a fast response to the changes in the electric field E while the ions remained approximately motionless. The kinetic energy gained by the electrons and the force eE can be expressed in a single dimension as follows,

$$m\ddot{x} = -eE \quad (1.18)$$

Integrating E using Gauss' theorem $\oint_S E \cdot dS = Q/\varepsilon_0$, where $Q = -Ldn_0e$ for a plane of area (Ld) , with L the plasma length, we obtain $E = n_0ed/\varepsilon_0$. Then,

$$\ddot{x} = -\omega_{pe}^2 x \quad (1.19)$$

where ω_{pe} is the plasma frequency,

$$\omega_{pe} = \left(\frac{n_0 e^2}{m \varepsilon_0} \right)^{1/2} \quad (1.20)$$

For typical tokamak parameters, see Table 1.1, $n_0 = 10^{19} \text{m}^{-3}$, the plasma frequency time is $\omega_{pe}/2\pi = 3.5 \times 10^{-11} \text{s}$.

1.4.3 A fusion plasma

A fusion plasma is an ionized gas with densities in the order of 10^{19}m^{-3} and temperatures between 1-40keV. At these temperatures the thermal motion exceeds the electrical binding forces in the atoms and the gas becomes ionized. The electrons and ions will move freely unless other external force is applied. The different particles will continue to interact under Coulomb forces through collisions for lengths in the limit $\lambda_D \sim 10^{-4} \text{m}$. In fusion, strong magnetic fields are applied to confined the particles changing their fundamental free motion accordingly to the applied forces, this motion is explained in Section 1.4.4. In Table 1.1 some of the most important parameters in a tokamak are summarized by existing ranges[Wesson, 2004]. Temperature and density are both very important parameters, and traditionally most plasmas in the known universe can be organized according to their value.

If we consider an externally applied magnetic field $\mathbf{B} = B_0 \mathbf{b}$ where \mathbf{b} is the unit vector chosen to follow the z -direction. In the presence of this magnetic field each particle will follow a prescribed path, and the particles will move principally under the action of the Lorentz force. In the next section we study the single particle motion, in which the particles gyrate in Larmor orbits due to magnetic field and drifts under the combined effect of both E and B fields.

Plasma volume	1	- 100	m ³
Total plasma mass	10 ⁻⁴	- 10 ⁻²	gm
Ion concentration	10 ¹⁹	- 10 ²⁰	m ⁻³
Temperature	1	- 40	keV
Pressure	0.1	- 5	atm
Ion thermal velocity	100	- 1000	km s ⁻¹
Electron thermal velocity	0.01	- 0.1	<i>c</i>
Magnetic field	1	- 10	T
Total plasma current	0.1	- 7	MA

Table 1.1: Typical tokamak plasma parameters, reproduced from [Wesson, 2004].

1.4.4 Single particle motion

The motion of particles is constrained by the electromagnetic forces and the changes in global electromagnetic fields. At the same time the electromagnetic fields are changing, and so does the particle motion. The particles will gyrate and translate forming a complex and intrinsic connection with the local fields. This is known as a self-consistent motion which satisfy the particles equation of motion and the Maxwell's equation. To simply understand the basic particle motion we need first to analyse the following cases.

Particle motion for $\mathbf{B} = 0$

Consider the following equation of motion of a particle moving under the action of an electric field \mathbf{E} .

$$m \frac{d\mathbf{v}}{dt} = q\mathbf{E} \quad (1.21)$$

If we take the time integral of Eq. (1.21) and choose the constant of integration to be \mathbf{v}_0 at time $t = t_0$, we find then the equation of velocity Eq. (1.22).

$$\mathbf{v}(t) = \frac{q}{m} \mathbf{E} t + \mathbf{v}(0) \quad (1.22)$$

The particle will move with an uniform acceleration $q\mathbf{E}/m$ in the direction of the electric field \mathbf{E} . The direction is subject to the changes of the sign for different species. The sign is negative for electrons and positive for ions.

Gyro-motion for $\mathbf{E} = 0$

The equation of motion of a single particle under the action of the Lorentz force in the presence of a magnetic field $\mathbf{B} = B_0 \hat{z}$ is,

$$m \frac{d\mathbf{v}}{dt} = q (\mathbf{v} \times \mathbf{B}) \quad (1.23)$$

where q is the charge of a test particle of positive sign, so that

$$m \frac{dv_x}{dt} = q v_y B_0 \quad (1.24)$$

$$m \frac{dv_y}{dt} = -q v_x B_0 \quad (1.25)$$

$$\frac{dv_z}{dt} = 0. \quad (1.26)$$

The last equation solution is simply a constant velocity along the magnetic field. The rest can be combined into one equation if we take the time derivative of Eq. (1.24) and then substitute dv_y/dt from Eq. (1.25) to obtain,

$$\frac{d^2 v_x}{dt^2} + \Omega^2 v_x = 0 \quad (1.27)$$

This is the homogeneous differential equation for a harmonic oscillator of frequency Ω , often called cyclotron frequency, or gyrofrequency, or Larmor frequency:

$$\Omega = \frac{q B_0}{m} \quad (1.28)$$

The solution for the velocity is then,

$$v_x(t) = v_\perp \sin(\Omega t + \theta_0) \quad (1.29)$$

$$v_y(t) = v_\perp \cos(\Omega t + \theta_0) \quad (1.30)$$

$$v_z(t) = v_{z0} \quad (1.31)$$

where v_\perp is the constant speed of the particle in the plane normal to \mathbf{B} and is geometrically $v_\perp^2 = v_x^2 + v_y^2$. The constant of integration is obtained from $\tan(\theta_0) = v_{x0}/v_{y0}$. A second time integration of Eqs. (1.29) to (1.31) will return the equations of a cylindrical helix of constant pitch angle. The angle between

\mathbf{B} and the direction of motion of the particle is called the pitch angle and is given by,

$$\alpha = \sin^{-1} \left(\frac{v_{\perp}}{v} \right) \quad (1.32)$$

where v is the total speed of the particle $v^2 = v_{\parallel}^2 + v_{\perp}^2$. This notation will be useful to separate movement along the magnetic field lines, and that perpendicular to it.

Another fundamental quantity in a magnetized plasma that comes from single particle motion is the Larmor radius or gyroradius. This is the radius that describes the orbital motion around the centre position (x_0, y_0) at time $t = t_0$ as the particle travels along the magnetic field line, i.e.,

$$r_L = \frac{v_{\perp}}{\Omega} \quad (1.33)$$

General solution of the equation of motion

We consider finally the motion of charged particles under the presence of both electric and magnetic fields, and assumed the fields do not change in time and also they are homogeneous in space. The equation of motion is then,

$$m \frac{d\mathbf{v}}{dt} = q (\mathbf{E} + \mathbf{v} \times \mathbf{B}) \quad (1.34)$$

Taking components parallel and perpendicular to \mathbf{B} as,

$$\mathbf{v} = \mathbf{v}_{\parallel} + \mathbf{v}_{\perp}$$

$$\mathbf{E} = \mathbf{E}_{\parallel} + \mathbf{E}_{\perp}$$

We obtain the following set of equations,

$$m \frac{d\mathbf{v}_{\parallel}}{dt} = q \mathbf{E}_{\parallel} \quad (1.35)$$

$$m \frac{d\mathbf{v}_{\perp}}{dt} = q (\mathbf{E}_{\perp} + \mathbf{v}_{\perp} \times \mathbf{B}) \quad (1.36)$$

Note in Eq. (1.35) the term $(\mathbf{v}_{\parallel} \times \mathbf{B})$ cancels out and $(\mathbf{v}_{\perp} \times \mathbf{B})$ has no parallel component, also it describes an accelerated motion just like in Eq. (1.22), but with acceleration given by $q\mathbf{E}_{\parallel}/m$. Eq. (1.36) is identical to

Eq. (1.23) after we applied the transform,

$$\mathbf{v}_\perp = \mathbf{v}'_\perp + \mathbf{V}_{E \times B} \quad (1.37)$$

where $\mathbf{V}_{E \times B}$ is given by $(\mathbf{E} \times \mathbf{B})/B^2$. The moving particle describes a circular motion with the characteristic cyclotron frequency, Ω , and radius, r_L . It follows then, that $\mathbf{v}'_\perp = \boldsymbol{\Omega} \times \mathbf{r}_L$ where $\boldsymbol{\Omega} = |\Omega|\hat{\omega}$, and $\hat{\omega}$ is the unit vector in the direction of gyration. The superposition of this circular motion in the plane normal to \mathbf{B} , plus a uniform motion with constant velocity $(\mathbf{E} \times \mathbf{B})/B^2$, and a uniform acceleration $q\mathbf{E}_\parallel/m$ along \mathbf{B} can be seen in Fig. 1.2. Finally, the particle velocity can be expressed in the following form,

$$\mathbf{v}(t) = \boldsymbol{\Omega} \times \mathbf{r}_L + \frac{\mathbf{E} \times \mathbf{B}}{B^2} + \frac{q\mathbf{E}_\parallel}{m}t + \mathbf{v}_\parallel(0). \quad (1.38)$$

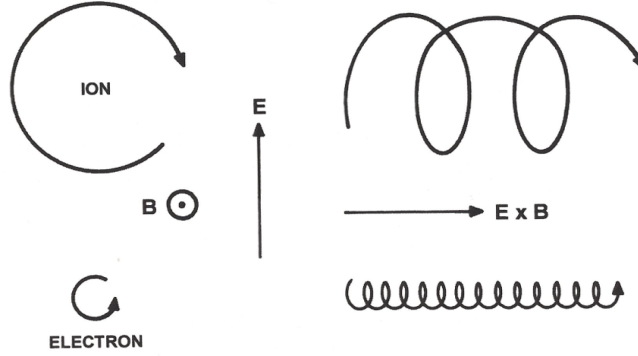


Figure 1.2: Cycloidal trajectories of ions and electrons in crossed magnetic and electric fields. The electric field \mathbf{E} acting together with the magnetic field \mathbf{B} gives rise to a drift velocity in the direction given by $\mathbf{E} \times \mathbf{B}$, reproduced from [Bittencourt, 2004].

1.4.5 Guiding centre drifts

Lets assume that the perpendicular electric field component in Eq. (1.36) is parallel to the x axis, $\mathbf{E}_\perp = E_x \hat{\mathbf{e}}_x$, the components of Eq. (1.36) becomes

$$\frac{dv_x}{dt} = \Omega v_y + \frac{q}{m} E_x \quad (1.39)$$

$$\frac{dv_y}{dt} = -\Omega v_x. \quad (1.40)$$

Taking the second derivative and combining those equations with 1.28, we obtain,

$$\frac{d^2 v_x}{dt^2} = -\Omega_s^2 v_x \quad (1.41)$$

$$\frac{d^2 v_y}{dt^2} = -\Omega_s^2 \left(v_y + \frac{E_x}{B_0} \right) \quad (1.42)$$

If we substitute $v'_y = v_y + E_x/B_0$, we recover the Eqs. (1.24) and (1.25), where the particles are gyrating about the guiding centre. Thus Eq. (1.41) describe a gyro-motion with a superimposed drift of the guiding centre in the $-y$ direction. This drift of the guiding centre is usually called $\mathbf{E} \times \mathbf{B}$ or $\mathbf{V}_{E \times B}$, and has the general form,

$$\mathbf{V}_{E \times B} = \frac{\mathbf{E} \times \mathbf{B}}{B^2}. \quad (1.43)$$

The $\mathbf{E} \times \mathbf{B}$ drift is independent of the sign of the charge and thus electrons and ions move into the same direction as showed in Fig. 1.2. A general form for any guiding centre drift can be expressed by the force \mathbf{F} as,

$$\mathbf{V}_F = \frac{1}{\Omega} \left(\frac{\mathbf{F}}{m} \times \frac{\mathbf{B}}{B} \right) \quad (1.44)$$

When the field lines are curved, a curvature drift appears. Due to their parallel velocity v_\parallel the particles experience a centrifugal force,

$$\mathbf{F}_R = m v_\parallel \frac{\mathbf{R}_c}{R_c^2} \quad (1.45)$$

where \mathbf{R}_c is the local radius of curvature or the inverse of curvature. Inserting

\mathbf{F}_R in Eq. (1.44) we obtain the curvature drift,

$$\mathbf{V}_R = \frac{mv_{\parallel}^2}{q} \frac{\mathbf{R}_c \times \mathbf{B}}{R_c^2 B^2}. \quad (1.46)$$

Hence, the curvature drift is proportional to the parallel particle energy $W_{\parallel} = mv_{\parallel}^2/2$. It creates a transverse current since ion and electron drifts have opposite signs. The curvature drift current has the form,

$$\mathbf{j}_R = n_e e (\mathbf{V}_{Ri} - \mathbf{V}_{Re}) = \frac{2n_e(W_{i\parallel} + W_{e\parallel})}{R_c^2 B^2} (\mathbf{R}_c \times \mathbf{B}) \quad (1.47)$$

All particle drifts can be described this way by using the appropriate force terms, as long as drift velocity is much smaller than its gyro-velocity. For polarization, and gradient drifts, these forces are $\mathbf{F}_P = -m d\mathbf{E}/dt$ and $\mathbf{F}_{\nabla} = \mu \nabla B$, respectively. Here $\mu = mv_{\perp}^2/2B$ is the magnetic moment. The drift polarization current and gradient current can be calculated in the same way as in Eq. (1.47). A summary of the guiding centre drifts is presented in Table 1.2.

$$\mathbf{E} \times \mathbf{B} : \mathbf{V}_{E \times B} = \frac{\mathbf{E} \times \mathbf{B}}{B^2} \quad (1.48)$$

$$\text{Polarization: } \mathbf{V}_P = \frac{1}{\Omega B} \frac{d\mathbf{E}_{\perp}}{dt} \quad \mathbf{j}_P = \frac{n_e(m_i + m_e)}{B^2} \frac{d\mathbf{E}_{\perp}}{dt} \quad (1.49)$$

$$\text{Gradient: } \mathbf{V}_{\nabla} = \frac{mv_{\perp}^2}{2qB^3} (\mathbf{B} \times \nabla B) \quad \mathbf{j}_{\nabla} = \frac{n_e(\mu_i + \mu_e)}{B^2} (\mathbf{B} \times \nabla B) \quad (1.50)$$

$$\text{Curvature: } \mathbf{V}_R = \frac{mv_{\parallel}^2}{qR_c^2 B^2} (\mathbf{R}_c \times \mathbf{B}) \quad \mathbf{j}_R = \frac{2n_e(W_{i\parallel} + W_{e\parallel})}{R_c^2 B^2} (\mathbf{R}_c \times \mathbf{B}) \quad (1.51)$$

Table 1.2: A summary of guiding centre drifts and the associated transverse currents.

1.4.6 Vlasov equation

We now turn to collective effects of the plasma. Let us consider again the particles distribution function $f(\mathbf{x}, \mathbf{v}, t)$ defined in Section 1.3. If no particle is lost or added to the plasma, the exact phase space density \mathcal{F} is conserved and then the averaged phase space density is the distribution function. Now,

we can describe the action of perturbations $\delta\mathcal{F}$ in a plasma kinetic equation as follows,

$$\frac{\partial f}{\partial t} + \mathbf{v} \cdot \nabla_x f + \frac{q}{m}(\mathbf{E} + \mathbf{v} \times \mathbf{B}) \cdot \nabla_v f = \frac{q}{m} \langle \delta\mathbf{E} + \mathbf{v} \times \delta\mathbf{B} \cdot \nabla_v \delta\mathcal{F} \rangle \quad (1.52)$$

This equation describes the evolution of coarse-grained phase space density in time and space under the action of average fields with linear perturbations. Linear perturbations of the type $f \rightarrow f + \delta\mathcal{F}$ separate the collective quantities from the perturbations, being these collisions or a self-similar correlation. For more detail in Eq. (1.52) see Baumjohann and Treumann [1997].

Consider solving Eq. (1.52) with all the correlations between particles and fields contained in the rhs is a very complicated problem. A way to simplify this term is by neglecting the correlations between the fields and account only for correlations between the particles via collisions, this approximation is known as the Boltzmann equation,

$$\frac{\partial f}{\partial t} + \mathbf{v} \cdot \nabla_x f + \frac{q}{m}(\mathbf{E} + \mathbf{v} \times \mathbf{B}) \cdot \nabla_v f = \left(\frac{\partial f}{\partial t} \right)_c \quad (1.53)$$

Since space plasmas are collisionless, except in the ionosphere, we can drop the collision term completely. This is the simplest kinetic equation of a plasma, called Vlasov equation,

$$\frac{\partial f}{\partial t} + \mathbf{v} \cdot \nabla_x f + \frac{q}{m}(\mathbf{E} + \mathbf{v} \times \mathbf{B}) \cdot \nabla_v f = 0 \quad (1.54)$$

Using the moments defined in Section 1.3, Eqs. (1.5) and (1.6) together with Eq. (1.54) we can use to determine the evolution of macroscopic quantities such as densities, velocities, and temperatures. The macroscopic single fluid description for plasmas is called magnetohydrodynamics (MHD), and it describes an electrically charged fluid under the action of external and internal electromagnetic fields. Taking the zero (Eq. (1.5)) and first order (Eq. (1.6)) moments we arrived at the continuity and momentum equation, Eqs. (1.55) and (1.56), respectively.

1.4.7 Waves in a cold plasma

There is a wide range of existing literature where all ranges of plasma waves are studied in detail, see for instance Stix [1997]; Swanson [2003]; Wesson [2004]; Freidberg [2007]. Linear theory of plasma waves is derived in various limits, for example hot and cold plasma, with magnetized and unmagnetized modes. We restrict our discussion to the most relevant compressional and torsional Alfvén waves, and the key modes relevant for this thesis. Then the ideal MHD equation for a magnetized plasma [Wesson, 2004] is as follows,

$$\frac{\partial n}{\partial t} = -\nabla \cdot (n\mathbf{v}) \quad (1.55)$$

$$nm\frac{d\mathbf{v}}{dt} = -\nabla p + \mathbf{j} \times \mathbf{B} \quad (1.56)$$

$$\frac{dp}{dt} = -\gamma p \nabla \cdot \mathbf{v} \quad (1.57)$$

$$\nabla \times \mathbf{B} = \mu_0 \mathbf{j} \quad (1.58)$$

$$\nabla \times \mathbf{E} = -\frac{\partial \mathbf{B}}{\partial t} \quad (1.59)$$

$$0 = \mathbf{E} + \mathbf{v} \times \mathbf{B} \quad (1.60)$$

where Eq. (1.60) is the non-resistive Ohm's law. Here γ is the adiabatic index, with $\gamma = c_P/c_V$, where c is the specific heat and P, V refer to constant pressure and volume, respectively. Here, n is the number density, \mathbf{v} is the velocity, p is pressure and \mathbf{j} is the density current. For an isotropic distribution function the pressure is a scalar, and we assume p to follow an adiabatic behaviour such as $d(p\rho^{-\gamma}/dt = 0)$. By linearising the set of magnetohydrodynamics ideal equations, with the sum of an equilibrium part and the perturbation we obtained a linear set of equations, such as that in [Baumjohann and Treumann, 1997, Chapter 9, Section 9.4]. Lets discuss the following modes now. When plasma oscillations are longitudinal perturbations, in the direction of the wave vector, we simply recover frequencies $\omega = \omega_{pe}$, this the plasma frequency was defined in Eq. (1.20). Here the magnetic field does not play a role. At high frequencies the ion mass is not relevant, but if we consider lower frequencies

it must be included to obtain,

$$\frac{\omega^2}{k^2} = \frac{1}{2} \left[C_s^2 + V_A^2 \pm \left((C_s^2 + V_A^2)^2 - 4C_s^2 V_A^2 \cos^2 \theta \right)^{1/2} \right] \quad (1.61)$$

where $V_A = B_0 / \sqrt{\mu_0 n m}$ is the Alfvén speed, and $C_s = \gamma(p_i + p_e) / n m_i$ is the sound speed. These speeds are also solutions of the linearized system; independent of the direction of \mathbf{k} the shear or torsional Alfvén wave satisfies $w = k_{\parallel} V_A$, see Fig. 1.3 top panel. The solutions of Eq. (1.61), where θ is the angle between \mathbf{k} and \mathbf{B} , are the magnetoacoustic waves. For $\theta = 0$, that is \mathbf{k} parallel to \mathbf{B} , the waves are,

$$\frac{\omega}{k} = V_A \quad \text{fast} \quad (1.62)$$

$$\frac{\omega}{k} = C_s \quad \text{slow} \quad (1.63)$$

For $\theta = \pi/2$, that is \mathbf{k} perpendicular to \mathbf{B} the modes are,

$$\frac{\omega^2}{k^2} = V_A^2 + C_s^2 \quad \text{fast} \quad (1.64)$$

$$\omega = 0 \quad \text{slow} \quad (1.65)$$

The fast wave is a compressional wave in which both the magnetic field and the fluid are compressed, see Fig. 1.3 bottom panel.

A generalized Ohm's law for a collisionless plasma follows from the electron fluid equation of motion, and assuming charge neutrality $n \approx n_e \approx n_i$ and with the total current defined as $\mathbf{J} = \mathbf{J}_e + \mathbf{J}_i$, we obtain:

$$\mathbf{E} = -\mathbf{J}_i \times \mathbf{B} + \frac{\mathbf{J} \times \mathbf{B}}{ne} - \frac{\nabla p}{ne} - \frac{m_e}{e} \frac{d\mathbf{u}_e}{dt} \quad (1.66)$$

The three new terms in Eq. (1.66) are: i) $\mathbf{J} \times \mathbf{B}$ or Hall term, ii) electron pressure gradient, and iii) electron inertia. Each of these terms introduces new physics into the system and has an associated characteristic length scale [Drake, 1995]. The $\mathbf{J} \times \mathbf{B}$ term describes whistler dynamics and is associated with the ion skin depth. The electron pressure term describes kinetic Alfvén dynamics and brings in the effective ion Larmor radius. The electron inertia terms introduce the electron skin depth. In the case of massless electron

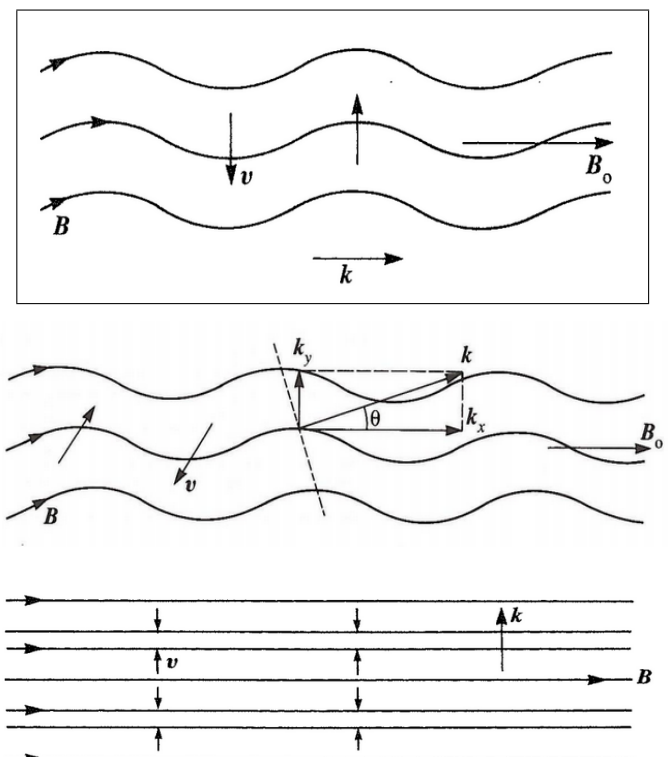


Figure 1.3: *Top panel*, torsional Alfvén wave with \mathbf{k} parallel to \mathbf{B}_0 . *Middle panel*, the magnetoacoustic wave has velocity oscillations in the plane containing \mathbf{B}_0 and \mathbf{k} . *Bottom panel*, the fast compressional magnetoacoustic with $\mathbf{k} \perp \mathbf{B}_0$. The oscillation involve compression of both the fluid and the magnetic field.

fluid approximation we drop the third term in Eq. (1.66). For example, in the Hybrid model of plasma the ions conserve its kinetic scales but the high frequency modes are not longer present due to the Darwin's approximation (see Section 2.3.2.) At least two wave modes coming from the extra terms in Ohm's law are important for the Hybrid description, see Section 2.3.2, the Whistler mode and the ion cyclotron resonant mode, see Fig. 1.4. Their frequencies, from Baumjohann and Treumann [1997], are respectively,

$$\omega = \frac{\Omega_e}{2} \left(1 + \frac{\omega_{pe}^2}{k^2 c^2} \right)^{-1} \left[\left(1 + \frac{4\omega_{pi}^2}{k^2 c^2} \right)^{1/2} + 1 \right] \quad (1.67)$$

$$\omega = \frac{\Omega_e}{2} \left(1 + \frac{\omega_{pe}^2}{k^2 c^2} \right)^{-1} \left[\left(1 + \frac{4\omega_{pi}^2}{k^2 c^2} \right)^{1/2} - 1 \right] \quad (1.68)$$

1.5 Tokamaks

A tokamak is a plasma confinement device. It confines plasma particles in close fields lines in the shape of a torus. There are two component fields to provide stability to particle motion drifts caused by curvature and magnetic field gradient, the poloidal and toroidal fields. We consider the drift now and the fields are explained in the next section. The plasma pressure is the product of the average particle motion and densities, this thermal pressure needs balance with the magnetic forces. These magnetic forces are those of magnetic pressure, $\nabla B^2/2\mu_o$, and field line curvature, $\mathbf{B} \cdot \nabla B/\mu_o$, in a tokamak. A measure of the efficiency of confinement of plasma pressure by magnetic pressure is given by the plasma beta,

$$\beta = \frac{p}{B^2/2\mu_0} \quad (1.69)$$

One of the drawbacks of the toroidal model is the magnetic field gradient in the direction of the major radius, and also the curvature in the low-field side. The particles experience a radially outward directed force F_R which is the sum of a centrifugal force and a ∇B force. As a result a drift motion occurs with drift velocity $\mathbf{V}_D = \mathbf{V}_\nabla + \mathbf{V}_R$, using Eqs. (1.50) and (1.51), called toroidal drift. This drift is transverse to both \mathbf{B} and ∇B . Because of the different charge

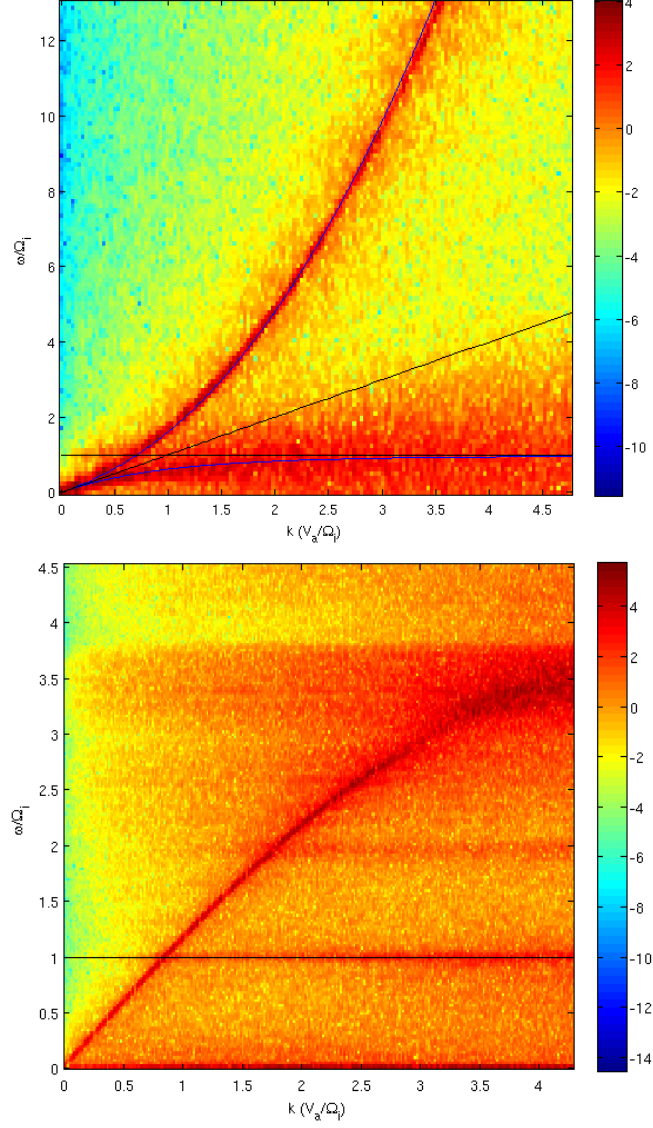


Figure 1.4: Dispersion relation for a uniform magnetized magneto-spheric plasma[Pritchett, 2000] simulated using a 3D hybrid code, algorithm description is in Section 2.3. The theoretical dispersion relations Eqs. (1.67) and (1.68) for whistler wave and ion cyclotron resonant mode are draw in blue line, alfvén speed black line, top plot. The perpendicular direction, bottom plot, shows the compressional magnetoacoustic mode from Eq. (1.64).

signs, electrons and ions experience drifts with opposite direction, giving rise to an electric field, which produces a destabilizing effect. In this way, adding the poloidal field is crucial to stop the toroidal drift. The effect is that of twisting the magnetic field lines helicoidally[Sakharov, 1958]. Here, we also define the safety factor as,

$$q = \frac{rB_\phi}{RB_p} \quad (1.70)$$

where r , R are minor and major radius respectively. B_ϕ and B_p are the toroidal and poloidal magnetic field. The safety factor q has a role in determining stability. Higher values of q lead to greater stability. If we follow a given field line many times around the torus a closed flux tube is mapped, and it is called a magnetic surface. Each magnetic surface has a different $q = \Delta\phi/2\pi$, where $\Delta\phi$ is the number of times a point in the field lines will return to the same poloidal point. For $q = 1$ the magnetic field line return to its position after 1 rotation. Then, $q = m/n$ for its combined toroidal m and poloidal n rotations. Fig. 1.5 gives an schematic view of the main areas of the poloidal cross section. The outer region is limited by the inner walls, and other plasma facing components (PFCs) such as limiters and the divertor (at the bottom). The area between the last closed flux surface (LCFS) or separatrix and the walls is the scrape-off layer (SOL). The SOL is a thin layer of plasma flowing both parallel and in the poloidal direction towards the limiter or divertor area. The area right inside the separatrix is the edge of plasma, and is a small section of the plasma between $0.9 < \hat{r} < 1$, where \hat{r} is the normalized minor radius. As the separatrix reaches the divertor, it forms the X-point, an area where the field lines reconnect. The X-point is an important section for the recycling of particles as the ions travel in and out the divertor through the LCFS many times during a discharge.

Poloidal and toroidal fields

The plasma is a highly conductive gas, and it can carry currents as a result of the relative drift between ions and electrons. In this way, the poloidal magnetic field is created by a toroidal current I_ϕ flowing through the plasma. The toroidal magnetic field is created by an array of coils in the toroidal direction, the effective result is a series of nested magnetic flux surfaces.

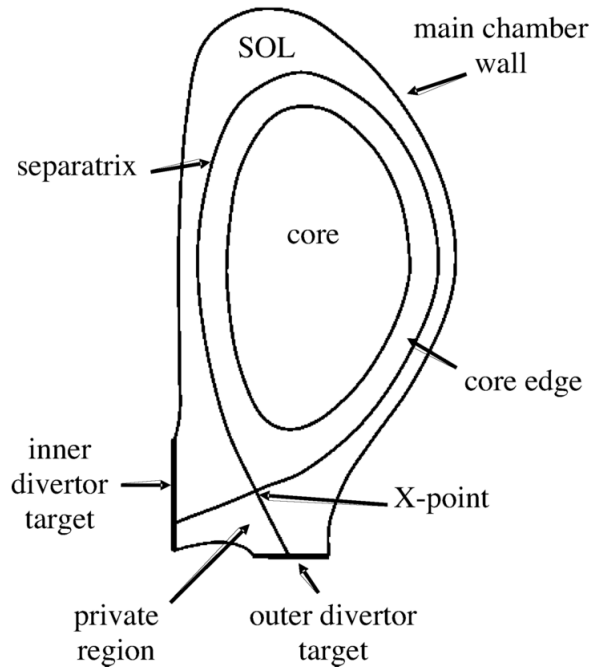


Figure 1.5: A tokamak poloidal cross-section showing the core of plasma at the centre, followed by the separatrix (the boundary between closed and open field lines), scrape-off layer (SOL) and finally the walls. In this configuration, a divertor is positioned at the bottom of the machine where the X-point lines reach the inner/outer divertor target.

The strongest magnetic field is the toroidal field. In Fig. 1.6 we can see that the lines showing the direction of toroidal field and toroidal current are extending along the entire toroidal direction. Also, the particles guiding centre (GC) follows in part the same toroidal direction, but under the action of the drift, the toroidal field is not enough to contain the particles and the poloidal field is required to twist the field lines creating the magnetic flux surfaces mentioned above. In absence of collisions or turbulence, the particle GC will remain in their motion. However, these combined fields are not enough for a sufficiently stable steady state and other means are normally necessary, such as error field corrections[Wesson, 2004]. The plasma pressure needs to be balanced by the magnetic forces making the necessary poloidal magnetic field and in turn the toroidal current I_ϕ increasing at a constant rate during the whole discharge time. As mentioned above, the poloidal field is mainly produced by currents within the plasma. In turn, these currents are created either by applying a constant change of flux through the torus (induction) or by beam injection; via heating[Wesson, 2004] or neutral beam injection[Wesson, 2004]. New advances in non-inductive scenarios have also been studied[Litaudon et al., 2002; Helander et al., 2005; Ju et al., 2000], but overall this is still a great challenge for the tokamak steady state performance.

Steady state

At steady state, a magnetically confined tokamak plasma comprises a family of nested magnetic flux surfaces in a smooth or laminar state. Yet, The tokamak is subject to a number of macroscopic instabilities[Wesson, 2004], for instance: MARFEs[Baker et al., 1982], Edge Localized Modes (ELMs)[Wagner et al., 1982], Disruptions[Gorbunov and Razumova, 1964; Sauthoff et al., 1978], Sawteeth[Von Goeler et al., 1974]. ELMs are detailed in Section 1.6. The MARFE, is a radiation instability which sometimes occurs when a dust ‘grain’ reach the X-point cooling the region by radiation. Sawteeth, are oscillations in the q -profile corresponding to the core plasma displacements with magnetic surfaces reconnecting as the core change its position. Disruptions are extreme events in which the plasma confinement is suddenly destroyed, and there are many causes known to trigger this event such as low- q profile, an unstable current profile, and impurity radiation cooling the edge plasma. Disruptions limit the

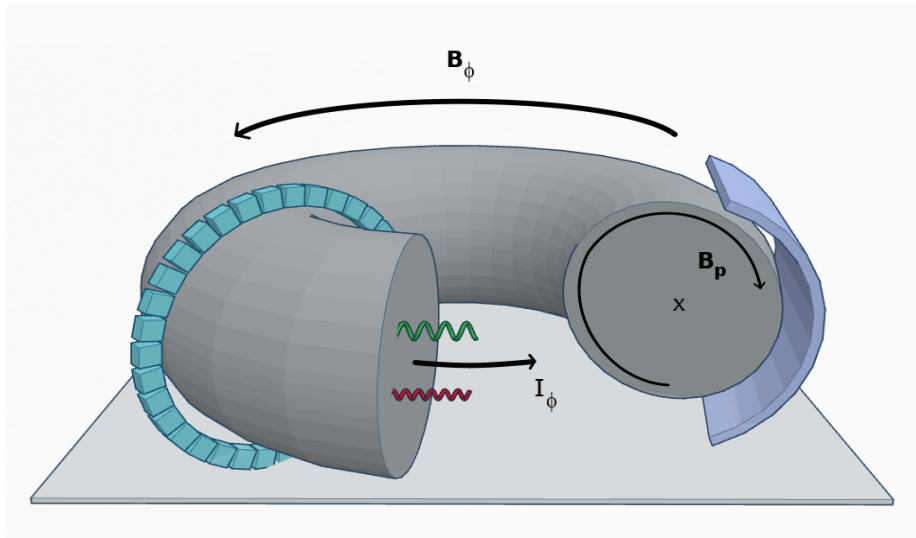


Figure 1.6: Schematic diagram of a tokamak. The plasma is contained inside a torus-shaped vacuum vessel. Poloidal B_p and toroidal B_ϕ magnetic fields keep the particles within the boundaries of the plasma in connected orbits and away from the walls. Particles gyrating (their guiding centre, as they gyrate around a field line) are also following the helical field lines formed by the combined toroidal and poloidal magnetic field lines.

operational range for currents and densities, and also leads to large mechanical stress and to intense heat loads.

The global steady state in a tokamak plasma is strongly dependent on: first, the internal balance between thermal pressure and the magnetic forces, and secondly the shape and plasma positioning controlled by external coils used during the runtime for reshape and control. The H-mode is a high confinement scenario characterized by the density pedestal formed at the edge of plasmas. In Fig. 1.7 a), the plasma pressure is profiled for a Low confinement mode (L-mode) and H-mode. In H-mode there is the formation of an internal transport barrier (ITB) that is responsible for the development of the pedestal and the enhanced confinement, characterized by a threshold plasma pressure p_{ped} . During this stage the MHD limit in the transport barrier is sometimes exceeded by edge localized modes instabilities that grow beyond the LCFS to open field lines reaching the machine vessel and divertor target in their own characteristic times, see Fig. 1.7 b).

1.6 Edge localized modes

Edge localized modes are a form of non-linear relaxation process for the edge region during the H-mode regime. They have been correlated with energy and particle loss[Zohm, 1996; Kamiya et al., 2007], and have been measured in different tokamaks, for example: ASDEX-Upgrade[Wagner et al., 1982], DIII-D[Fenstermacher et al., 2013], JET[Connor, 1998], JT-60U[Kojima et al., 2009], and MAST[Wilson et al., 2006].

The detection of ELMs has been associated to the measurement of the Balmer line, at wavelength 656.3nm, radiated from neutrals which are present in the SOL. In JET the D_α signal has been the main point of observation for the inner and outer divertor, only recently it has been replaced by Beryllium II. ELMs present a characteristic spike-chain clearly visible in different lines of sight, and in even other diagnostics. One of the imposed limitations of a steady state under ELMs is their energy deposition in material walls and divertor targets. The ELM heat flux deposition is currently a great threat to longer confinement times, imposing limits in both the surface-materials in the first wall and the lifetime of PFCs. It is also a limiting factor given the current

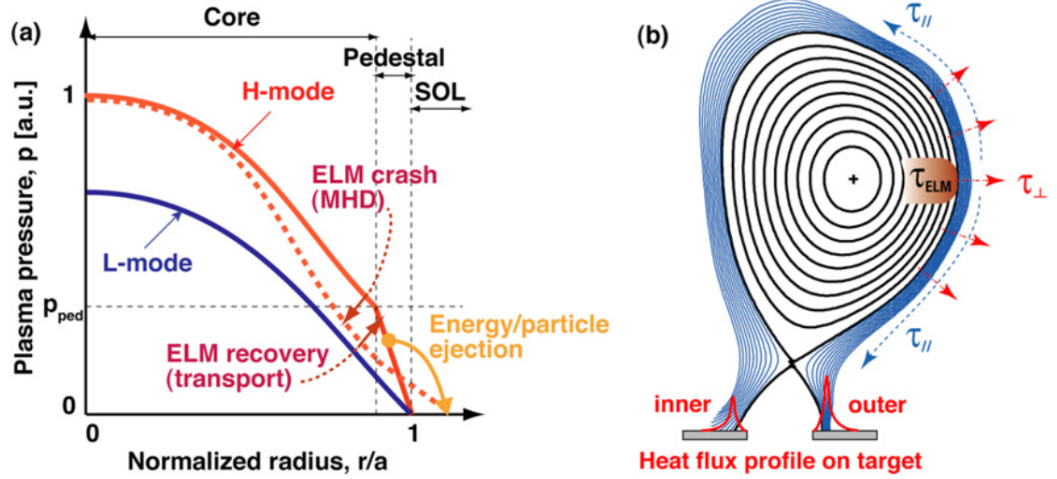


Figure 1.7: Two main areas of the mayor radius can be seen in panel (a), the section of the core where L-mode and H-mode pressure profile decreased in a similar way, and the dramatic difference in the pedestal zone where a steep pressure gradient is observed forming during the H-mode. Noticeably, the arising of one instability is depicted here, the ELM crash, to account for the sudden lost of pedestal pressure threshold and the return to a similar L-mode state, with the main difference that the pedestal is then quickly recovered. (b) We observe here the poloidal cross-section of the plasma and the magnetic surfaces with the X-point at the bottom typical of the H-mode plasma. The ELM time period is depicted at the edge showing two different times for perpendicular and parallel displacement. Reproduced from [Kamiya et al., 2007].

material heat flux limit in machines the size of ITER. This section is dedicated to provide a brief review of most important ELM features, the current state of research, and some of the techniques for ELM control and suppression.

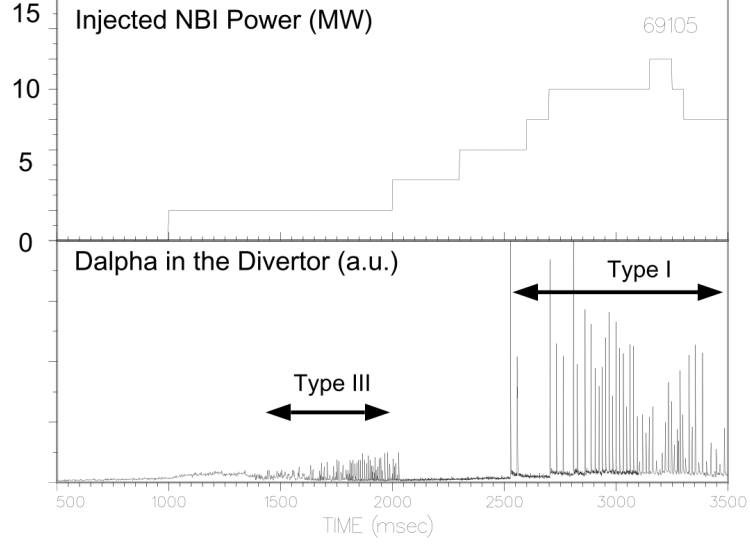


Figure 1.8: Typical sequence of ELMs during a power rise in DIII-D: at $P \sim P_{thr}$ type III ELMs are found; at higher P , type I ELMs occur.

Phenomenological categorization

There are many types of observed ELMs [Zohm, 1996], see Fig. 1.8. The main three types of ELMs are:

- Type I, are large in amplitude and narrow in time, characterized by a minor reduction of energy confinement time, and larger energy loss ΔW_{ELM} .
- Type II, is the most desirable mode of operation due to both the release of impurities and attainment of stable high edge pressure, characteristics of the H-mode.
- Type III, reaches a low edge-pressure eliminating the benefits from H-mode operation. This type-III is visible during the L-H transition ramp-up.

1.6.1 L-H transition and ELMs

Within the operation of tokamak experiments many regimes exist [Gomezano et al., 2008], but most common are the lower, and higher confinement. ELMs were first observed in the ASDEX-Upgrade by Wagner et al. [1982] during H-mode testing experiments. The amount of external heating power and the way the plasma makes contact with the material surface are factors amongst others which facilitates the L-H transition. In terms of material contact, there are two generic plasma-wall interfaces known as the ‘limiter’ and the ‘divertor’. The H-mode has been found more accessible in divertor geometries, and the transition is reproducible on almost every tokamak.

The ELM is, in an unknown way, connected with the temporarily breakdown of the H-mode internal transport barrier, although only for ELMs type-I this has been suggested [Zohm, 1996]. What the cause for these phenomena is unknown. It is observed that during the ramp-up phase, L-mode heating phase, sawteeth are observed along ELM type - III [Zohm, 1996] and they stop once the H-mode has been reached, which is probably due to the edge transport barrier formation. In a very short time range, the ELM triggered by the pressure-release-mechanism or build-up process, reaches the pressure threshold limit and then a burst occurs. The effect of releasing this pressure is shown via convective transport of particles (momentum exchange) towards the midplane and divertor. It has been suggested that this transition represents a local H-L-H transition, and the pressure build up release cycle [Kamiya et al., 2007]. For the moment, understanding the L-H transition’s physical mechanisms has been reason of an extensive research and it remains partly unexplained [Fundamenski et al., 2012; Singh et al., 2012].

1.6.2 ELM measurements

The focus has been to understand the properties of ELMs type-I in H-mode plasmas. Mitigation of ELMs type-I in a steady state of operation have been tested for instance in MAST [Kirk et al., 2013] where resonant magnetic perturbation had a 3D effect which works towards ELMs getting smaller amplitude with more frequent bursts. Hot-ion H-mode plasmas are characterized by an ELM-free period lasting a few seconds. In JET, during ELM-free H-mode, the

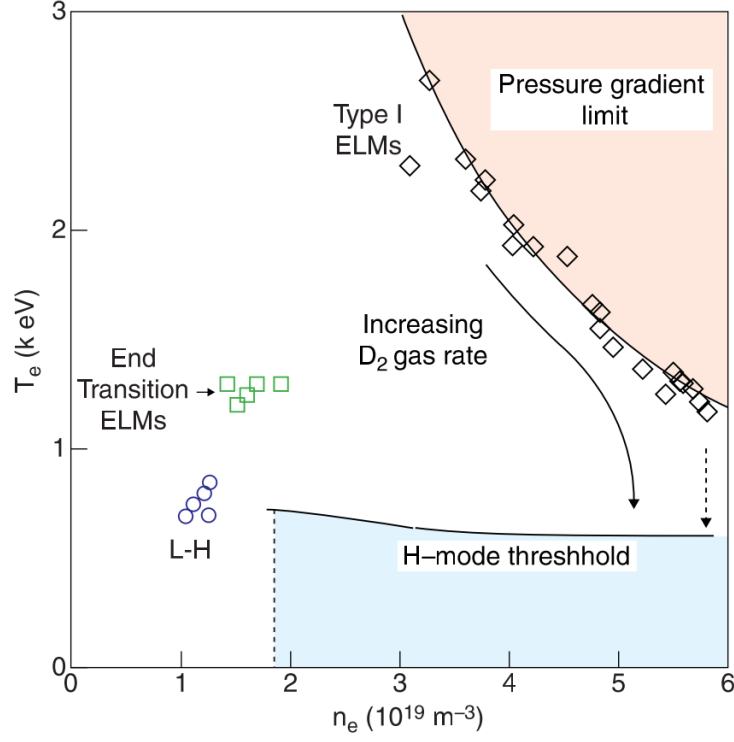


Figure 1.9: Plot of edge electron temperature versus density for a series of vertical target ELMy H-modes with varying rates of gas fuelling. The temperature and density values at the pressure gradient limit (diamonds) are representative of values at the top of the edge electron pedestal taken just prior to an ELM crash. The edge electron temperature and density at the L-H transition (circles) and at the end period of the transition ELMs (squares) are shown for comparison. At highest gas fuelling rates, the edge electron pressure begins to deviate from the curve of approximately constant pressure (the dashed arrow). In a few cases, transitions back to L-mode have been observed; here the curve for the H-mode threshold is schematic. Reproduced from [Horton et al., 1999].

plasma current was found to be a control parameter for ELM onset and the changes of the edge barrier width [Nave et al., 2000]. The ELM-free mode is generally non-stationary, therefore the cyclic ELM behaviour allows for stationary H-mode operation. In TCV, rapid vertical movement of ELMy H-mode plasmas were found to affect the waiting times in the ELMs sequences, it was attributed to the raise of an edge current [Degeling et al., 2003]. A major reason of concern is that ELMs has been measured to release up to 10% of the stored energy during the pulse [Zohm, 1996; Kamiya et al., 2007]. Peak power fluxes of unmitigated ELMs in ITER are expected to reduced the lifetime of divertor targets and PFCs to a few hundreds discharges with the current experimental scaling. Therefore, ELM frequency control is an open question whereas to mitigate the impact to ITER, according to the observed scaling of the energy released per ELM versus the ELM frequency, $\Delta W_{ELM} \approx 1/f_{ELM}$ [Zohm, 1996; McDonald et al., 2008]. Future ITER plasma scenarios will need to include the impurities accumulation towards the increased risk of disruptions given ELM suppression or mitigation scenarios. Furthermore, avoiding serious damage in the tokamak PFCs and divertor areas will be a key aspect to avoid major delays, because their replacement will be carried via remote control. Controlling the ELM frequency has become critically important for ITER as well. Gas injection has been studied in JET density peaking technique [Valovic et al., 2002], this method also works towards achieving high-density H-mode plasmas required for ITER. The density has been observed to increase during the heating phase and then remained stationary; finally, it terminates in a MHD or density limit, which is accompanied by an ELM transition from type-I to type-III followed by the return to L-mode (see this phases in Fig. 1.9). Pellet injection has also been used to achieve high confinement with high density, proving steady state with densities above the Greenwald limit [Lang et al., 2002]. ELM frequency has been measured to follow to a great extent the pellet frequency [Lang et al., 2013, 2011].

1.7 Blobs and filaments

Blobs or filaments are spatially extended structures present in tokamaks and basic plasma physics experiments. These structures are visible in 2D measure-

ments in the plane perpendicular to magnetic field \mathbf{B} as shown in Fig. 1.10. Theory and simulations predict that blobs and ELMs [Zohm, 1996] filaments are the result of the non-linear saturation of the edge turbulence, or coherent MHD instabilities, respectively [D'Ippolito et al., 2011]. The blobs/filaments provide a mechanism for the convective radial transport of particles [Krasheninnikov, 2001], heat [D'Ippolito et al., 2002; D'Ippolito and Myra, 2006], momentum [Myra et al., 2008], and parallel current [Myra, 2007] to the scrape-off layer, increasing the interaction of the plasma with material walls [Krasheninnikov et al., 2008]. Also, the blob model, with its convective and diffusive transport, incorporated to the non-Gaussian statistics observed at the edge of toroidal plasmas, starting at the separatrix to the far SOL, evidence points to these coherent structures [Xu et al., 2009; Naulin, 2007]. The existence of apparent coherent structures in the turbulent SOL was first observed using fast cameras [Goodall, 1982], around the same year when ELMs were first observed in ASDEX [Wagner et al., 1982]. The presence of blobs filaments was also observed in ASDEX using fast cameras, it was found that filamentary structure may always be present, but not always visible, and they are only illuminated by the presence of atoms or ions emitting visible radiation [Goodall, 1982]. Using different techniques, for instance, gas puff imaging (GPI), beam emission spectroscopy (BES) and Langmuir probes, these structures have been measured across many devices; NSTX [Maqueda et al., 2011] and Alcator C-Mod [Terry et al., 2003] using GPI, DIII-D [Boedo et al., 2003] using BES, and TORPEX [Furno et al., 2008] using Langmuir probes.

A general definition of the observed objects that arise in theory, simulations, and experiments satisfied the following properties:

1. It has a monopole (single-peaked) density distribution with a peak value much higher than the surrounding rms¹ fluctuations of the background plasma (typically $\geq 2 - 3$ times higher).
2. It is aligned parallel to the magnetic field \mathbf{B} ; the variations along \mathbf{B} are much weaker than those in the transverse direction, i.e. $\delta_b/L_{\parallel} \ll 1$, where δ_b and L_{\parallel} are the blob radius and parallel characteristic length, respectively.

¹Root mean square fluctuation.

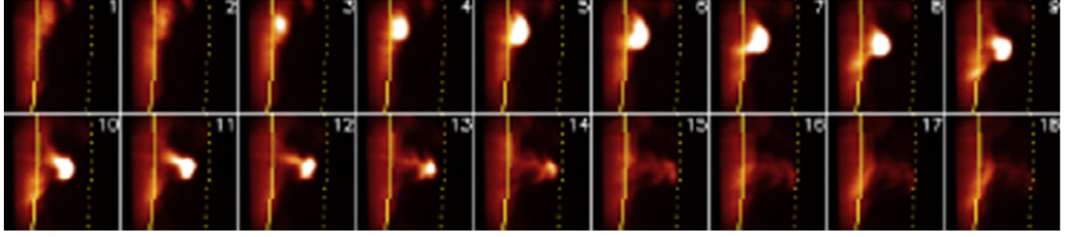


Figure 1.10: Blob creation and propagation in NSTX as seen by the GPI diagnostic. The frame rate is $7.5\mu\text{s}/\text{frame}$ and the camera extension is $25 \times 25\text{cm}$ near the outer midplane separatrix (solid line). The radial convection towards the limiter (dashed lines) has an approximate velocity of $\sim 1\text{km/s}$. Reproduced from Maqueda et al. [2011].

3. It has a dominant convective velocity $\mathbf{V}_{E \times B}$ in the direction of a charge-polarizing force, generally due to curvature and $\nabla \mathbf{B}$ in a toroidal plasma, and an associated potential and vorticity with a dipole structure in the direction transverse to its propagation, i.e, the tokamak's poloidal cross section.

1.7.1 Sheath-limited model of blobs

A 2D simplified model of a blob based on plasma polarization via an arbitrary force \mathbf{F} , see Fig. 1.11, where the force mechanisms can be those of the edge in toroidal plasmas, namely curvature or $\nabla \mathbf{B}$, has been proposed in Krasheninnikov et al. [2008]; D'Ippolito et al. [2011]; Myra and D'Ippolito [2005]. In this simple model, the balance of polarization caused by an effective gravity force $\mathbf{F} = nm_i \mathbf{g}_{sp}$ and the dissipation of that polarization through parallel current lead to the formation of a coherent structure like blobs. The \mathbf{g}_{sp} has the interpretation of a single particle gravitational acceleration, but its origin is constrained to forces which yield to $\mathbf{b} \cdot \nabla \mathbf{F} \propto \partial n / \partial y$, where y is approximately the poloidal coordinate in slab geometry. If we establish charge conservation,

$$-\nabla \cdot \mathbf{J}_\perp = \nabla_\parallel J_\parallel \quad (1.71)$$

where J_\parallel is the current parallel to the \mathbf{B} field and \mathbf{J}_\perp perpendicular to it. The reaction of charge particle drift, see Section 1.4.5, to the external force

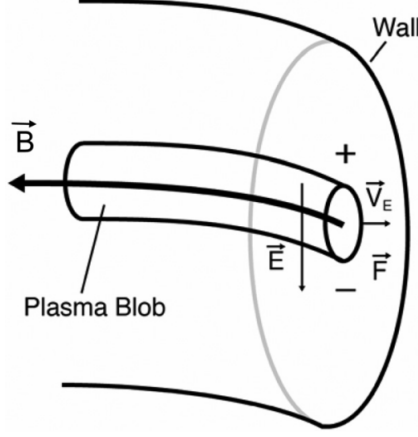


Figure 1.11: A representation of a blob (2D) or filament (3D) on the outer midplane of the tokamak's edge plasma. This structure is localized in the plane perpendicular to magnetic field, but it is extended in the parallel direction, along \mathbf{B} . The blobs are believed to originate of either turbulence or macroscopic MHD instabilities. Figure is reproduced from D'Ippolito et al. [2011].

\mathbf{F} induces a current $(c/B^2)\mathbf{F} \times \mathbf{B}$, and also polarization inside the blob by separation of charges with different sign. The charge polarization due to an effective gravity force, is followed by $\mathbf{E} \times \mathbf{B}$ convection. The perpendicular current \mathbf{J}_\perp in Eq. (1.71) can be written as the sum of the ion polarization-drift current $\mathbf{J}_{\perp,\text{pol}}$ and the particle drift induced current, Eq. (1.71) is then written as follows,

$$\nabla \cdot \left(\frac{nm_i c^2}{B^2} \nabla_\perp \phi \right) = \nabla_\parallel J_\parallel + \frac{c}{B} \mathbf{b} \cdot \nabla \times \mathbf{F} \quad (1.72)$$

where n is the plasma density, m_i ion mass, B is the magnetic field stress, $\mathbf{b} = \mathbf{B}/B$, ϕ is the electrostatic potential, c is the speed of light, $d(\cdot)/dt = \partial(\cdot)/\partial t + \mathbf{V}_{E \times B} \cdot \nabla$, and $\mathbf{V}_{E \times B} = c(\mathbf{b} \times \nabla \phi)/B$. We also have,

$$\frac{dn}{dt} \equiv \frac{\partial n}{\partial t} + \mathbf{V}_{E \times B} \cdot \nabla n \approx 0. \quad (1.73)$$

The magnitude of the \mathbf{E} field induced by the external force is obtained by balancing the current source from the $\mathbf{F} \times \mathbf{B}$ drift with the parallel and perpendic-

ular loss currents, according with the blob ‘electrical circuit’ [Krasheninnikov et al., 2008; Myra and D’Ippolito, 2005]. For blobs in a tokamak’s SOL the parallel currents in the circuit model are dependent on the plasma and sheath resistivities, and magnetic geometry, e.g. the geometry nearby the X-point at the divertor [D’Ippolito et al., 2011].

At the limit when the blob’s parallel current $J_{\parallel} = ne^2c_s\phi/T_e$ in the ‘circuit model’ is sheath limited to the 2D approximation, it allows for an analytic solution of Eqs. (1.72) and (1.73). This solution has the form of an isolated blob of plasma density convecting in the radial (x) direction with the speed v_b ,

$$n_b = n(x)(x - v_bt)e^{-(y/\delta_b)^2} \quad (1.74)$$

$$v_b = 2c_s \left(\frac{\rho_s}{\delta_b} \right)^2 \frac{L_{\parallel}}{R} \quad (1.75)$$

Here c_s and ρ_s are the sound speed and the corresponding gyroradius, R and L_{\parallel} are the radius of curvature and the sheath-to-sheath parallel connection length, finally δ_b is the blob radius in the poloidal (y) coordinate, where the (x, y, z) denote the local coordinates in the radial, poloidal, and parallel along \mathbf{B} directions, usually called slab geometry.

1.7.2 Simulation of blobs

The numerical evolution of seeded plasma blobs based on Eqs. (1.72) and (1.73) has been studied extensively in Krasheninnikov et al. [2003]; Myra et al. [2006]; Bian et al. [2003]; Aydemir [2005]; Garcia et al. [2006]; D’Ippolito and Myra [2003]; Yu and Krasheninnikov [2003]. The plasma density profile of the seeded blob are usually described as in Eq. (1.74), using a Gaussian profile, where the peak density n_{peak} is usually an integer factor of the background plasma density. The results of these simulations have shown that some blobs are unstable, but they can propagate through convection for large distances. One of the main factors for blob stability appears to be the blob radius δ_b . With a normalized blob radius $\hat{\delta} = \delta_b/\delta_*$, where δ_* is the critical blob size and v_* is

its characteristic velocity defined as,

$$\delta_* = \rho_s \left(\frac{L_{\parallel}^2}{\rho_s R} \right)^{1/5} \quad (1.76)$$

$$v_* = c_s \left(\frac{\rho_s^2 l_{\parallel}}{R^3} \right)^{1/5}, \quad (1.77)$$

the typical regimes for blob propagation are then:

- $\hat{\delta} < 1$, Kelvin-Helmholtz instability determines the stability of small scale blobs.
- $\hat{\delta} \sim 1$, blobs are stable for radial propagation.
- $\hat{\delta} > 1$, interchange instability is the controlling instability in this regime.

Although, the available experimental data for small scale blobs is limited given the constraints in identifying them, numerical simulations in Kelvin-Helmholtz dominated regime show a clear tendency to develop a mushroom shape in its evolution [Yu and Krasheninnikov, 2003; Aydemir, 2005; Bian et al., 2003], see Fig. 1.12. For large blobs, the interchange instability plays the principal role for the most part of the blob evolution [Yu and Krasheninnikov, 2003; Aydemir, 2005; Bian et al., 2003], where a non-linear phase generates Rayleigh-Taylor lobes or radial finger structures, as shown in Fig. 1.13.

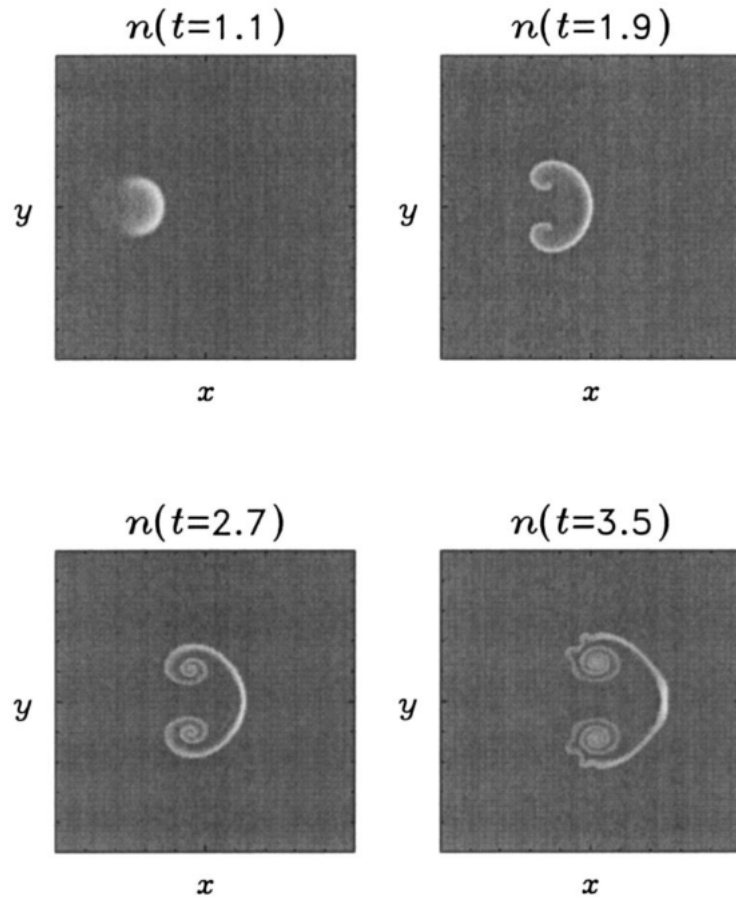


Figure 1.12: Contour plot of the evolution of a 2D density blob with small δ_b . During the radial motion of the blob the density concentrates at half of its periphery creating a front. The blob is unstable to the Kelvin-Helmholtz mode and evolves to a mushroom shape object. Reproduced from Bian et al. [2003].

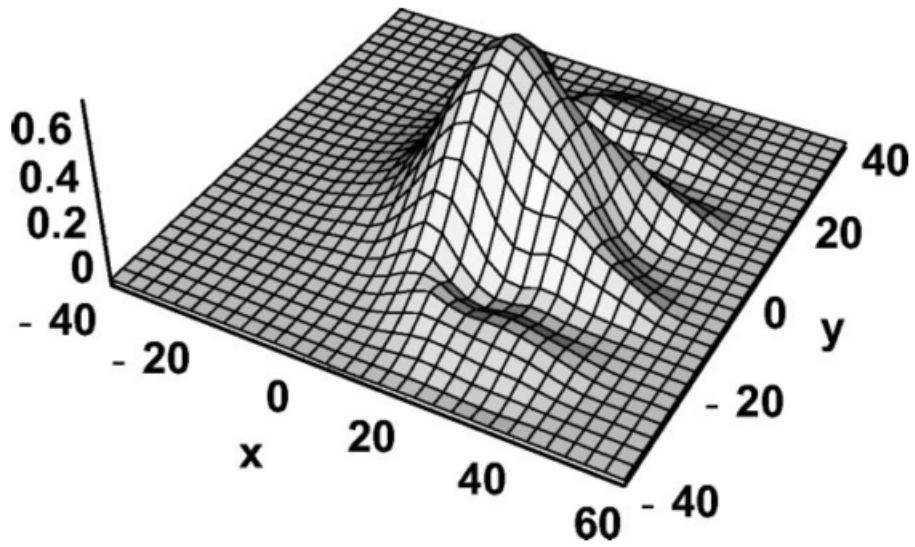


Figure 1.13: blob density profile with large δ_b in a 2D simulation. During the radial motion of the blob, it becomes unstable to the curvature-driven interchange mode. Here the non-linear phase is characterized by the presence of elongations or fingers as seen across the poloidal direction in slab geometry. Reproduced from D'Ippolito and Myra [2003].

Chapter 2

Methods

2.1 Introduction

In the areas of fusion, space and solar plasmas there is a wealth of accumulated data, particularly in fusion, JET tokamak has more than twenty years of stored data [Layne and Wheatley, 2002; Layne et al., 2012]. The data is characterized by multiple interacting nonlinear plasma processes. In order to analyse through such complex nonlinear phenomena one can test a combination of linear and nonlinear techniques. In the following section we briefly discuss some basics test before applying nonlinear analysis. Then, we explain the methods used in the Chapters 3 and 4.

2.1.1 Standard test for linear signals

Modern tools such as Matlab or python are useful to run simple tests for linear and nonlinear time series [Schreiber and Schmitz, 2000]. First, we define the autocorrelation function and stationarity. We also provide a very simple example of their use, with an additional test against the null hypothesis for randomly distributed signals with QQplots.

Autocorrelation

If we are studying a measurable quantity $x(t)$ which fluctuates in time, usually two interesting quantities to evaluate are the mean value and the variance.

They both have a global meaning as the moments of the probability distribution of the quantity $x(t)$. Yet, if we are interested in the influence of the value of x at time t on the same variable at time $t + \tau$ we can evaluate the autocorrelation function as follows,

$$A(\tau) = \lim_{T \rightarrow \infty} \int_0^T dt x(t)x(t + \tau) \quad (2.1)$$

This represents the time average of the variable product in two different times over an arbitrary large time T , which is then allowed to become infinite. We could also use the autocorrelation function to test a random variable against the null hypothesis by sampling for different T and then calculate the residual values.

Stationarity

Stationarity can be defined from considering the ensemble averaged signal, where the ensemble is the collection of all possible realizations of the variable x , therefore we may repeat the same measurements many times, and calculate the averages, this are denoted as $\langle \quad \rangle$. In many systems, the time averaged is equal to the ensemble average, such systems are known as ergodic. If we have a stationary process $x(t)$, it is reasonable to expect that the average measurements can be constructed by taking values of the variable x at successive patches. The new average value is then,

$$\bar{X}(T) = \frac{1}{2T} \int_{-T}^T dt x(t) \quad (2.2)$$

By averaging $\bar{X}(T)$ over all times we recover the mean value as in $\langle \bar{X}(T) \rangle_T = \langle x \rangle$. If $x(t)$ is an ergodic system we then have,

$$\langle x(t)x(t + \tau) \rangle = A(\tau) \quad (2.3)$$

for which all time dependent averages are equally to those ensemble averaged, i.e. the probabilistic structure of a completely stationary process is invariant under a shift in time, and therefore we can use the running average as a test.

QQplots

A quantile-quantile plot is a technique to compare two different probability distributions. The QQplot helps in determining if two data sets come from populations with a common distribution. The most common probability distribution for random variables is the normal or Gaussian probability distribution, although many others model distribution exists. The central limit theorem state that with sufficiently large number of realizations in a random variable, the arithmetic average of the variables will be approximately normally distributed, regardless of the underlying distribution. Let us consider an example, the emission (X-ray) coming from a binary pulsar star, in this case the Cepheus X-4 has shown several detections of outburst, and they have been measured since it was first catalogued in 1993 by Schulz et al. [1995]. The latest documented outburst was observed in 2002[McBride et al., 2007]. Now, we plot the probability distribution of the time series in Fig. 2.1 and the QQplot in the right, where the normal distribution test can be seen as a red straight line. The tails deviate from the Gaussian, and there is no evidence of the nonlinear bursts. We have also run a simple test for stationarity of the signal with the mean, variance, and standard deviation. These quantities are the plotted in Fig. 2.2. We can observe the previous reported bursts, in 1996 and 2002, looking at the running mean value, and from it we can also infer that there has been a burst of the X-ray binary star in November 2009, possibly not reported yet.

2.2 ELMs Methods

In the following section we describe the methods for the analysis of the ELM time series which resulted in Chapter 3.

2.2.1 ELM detection

The D_α radiation at wavelength 656nm is measured to produce the time series X_n for ELM detection. The identification of ELMs type-I, or any, allow us to determine the new time series X_t [Schreiber and Schmitz, 2000], where t is the time of each ELM at its highest peak value. Although standard normal-

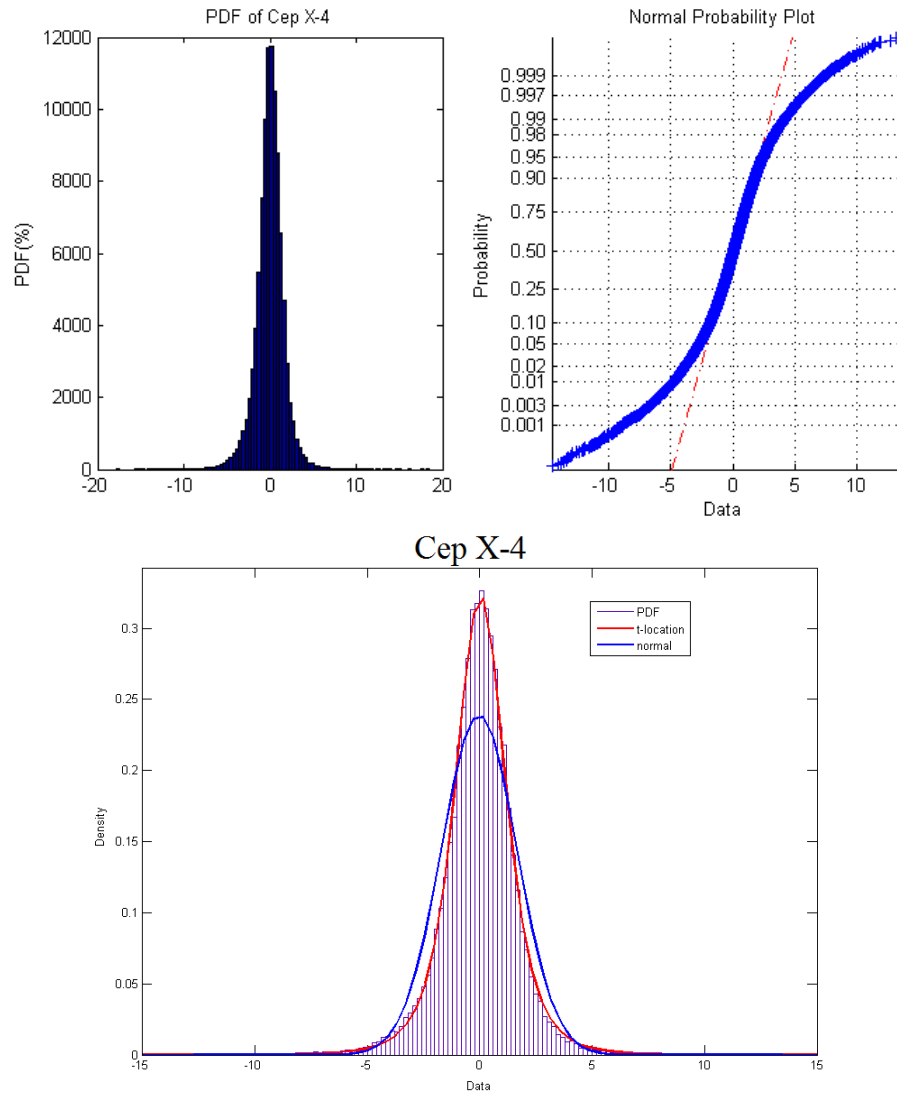


Figure 2.1: On the top left, the Probability distribution of the variable star Cep X-4 is showed, with bins of 10^3 points. On the top right, The QQplot test, see Section 2.1.1, is showing evidence that Cep X-4 does not possess a Gaussian distribution. Bottom plot, we have fit Cep X-4 distribution with two different model distributions, in blue a Gaussian distribution, and in red a t-student distribution which shows a better fit of the signal distribution.

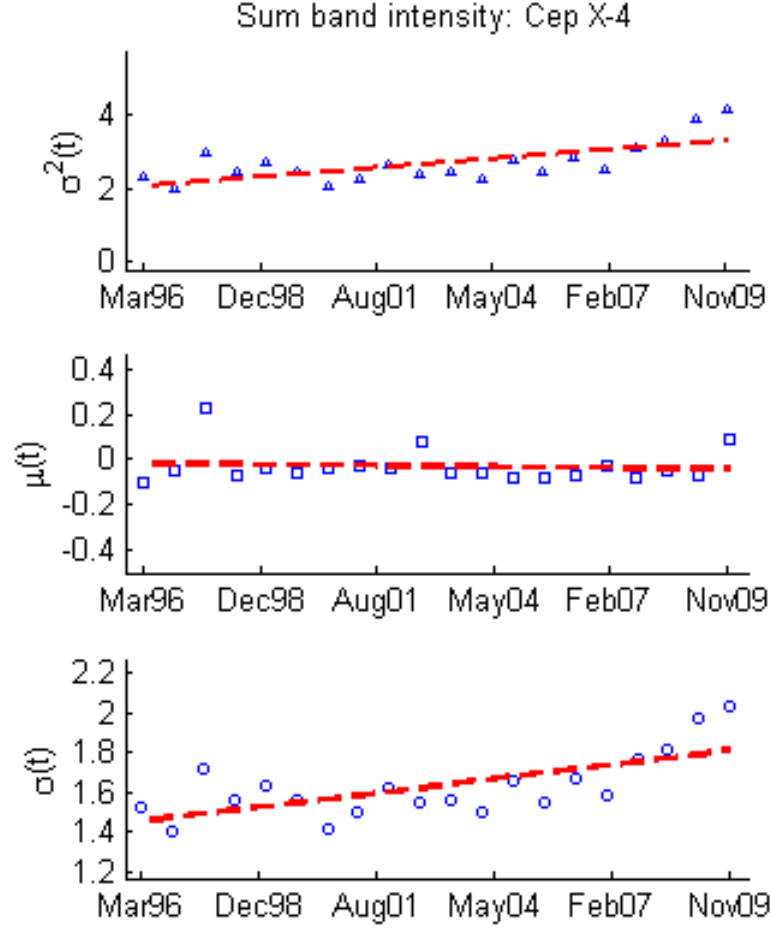


Figure 2.2: Running mean, variance, and standard deviation. The linear fit, red line, has the following slope values: from the bottom, variance $m = 0.064$, mean $m = -0.0013$, the standard deviation $m = 0.018$. We find then semi-stationary time windows where linear methods can be applied in between bursts.

ization, by subtraction of the mean and division by the standard deviation, is typical, we simply normalized by the mean value as it was observed that the signal amplitude was saturated on occasions rendering the values negligible, see Fig. 2.4 (plasmas 57867 and 57865). The intensity of the time series without ELMs or during the inter-event can be relevant for other studies such as determination of the pedestal conditions [Beurskens et al., 2009]. The JET plasma discharges ranges from 57855-57874 and 55766-55786. The ELM detection algorithm is applied to the entire length of each dataset. At first, a critical threshold is identified at $T_c = k\sigma$ where σ is the signal standard deviation and k is a constant. The nonstationary of the signal was observed leading to optimize the time window where threshold T_c remained within the range of random noise, $\sim 3\sigma$. Because the amplitude of the ELM bursts typically raised beyond 3σ two possibilities exists for detection; first, using a peak finding routine, for instance the ‘peaks’ function in Matlab, or secondly, looking for other regular features. There may be a third, which implies a fitting model distributions on each peak, but this is computationally expensive. The routines to find spikes are typical in patterns of neural activity, for instance the spike-train events in Pipa et al. [2013].

We observed something more particular, each ELM peak revealed a large gradient and a very short time windows, for instance the slope $m = 8.13 \times 10^4$ and ELM duration 5.5ms. In Fig. 2.3 we can see the linear fit, the ratio between ELM duration and the subsequent waiting time is $\Delta_{ELM} \approx 0.11$ for JET plasma 57865. This ratio is closer to 1.0 were gas has higher concentrations as in JET plasma 57869. Hence, the variations in amplitude are much faster than those in Δt , from which is relatively safe to assume that near the ELM peak $m_i \approx \Delta y_i$, where y_i is the signal amplitude. Under this assumption we select points using the following criteria,

$$\text{ELMs:} \quad m_i, m_{i+1}, m_{i+2} > 0 \quad \wedge \quad m_{i+3} \leq 0 \quad (2.4)$$

$$\text{Noise:} \quad m_i, m_{i+1}, m_{i+2} < 0 \quad \wedge \quad m_{i+3} \leq 0 \quad (2.5)$$

where $i = 1 \dots N$ and N is the total number of points in the original time series. We simply detect the change in ascending gradient to descending gradient, then we threshold for amplitude $T_c > 3\sigma$ to separate ELMs from noise. We

select more than 95% of all ELMs and the algorithm is very fast, yet we have to mask a few points, which is explained in next section, to ensure accuracy in the new time series X_{ELM} given the reduced number of ELMs per plasma, ranging approximately from [80 - 150] ELMs per plasma.

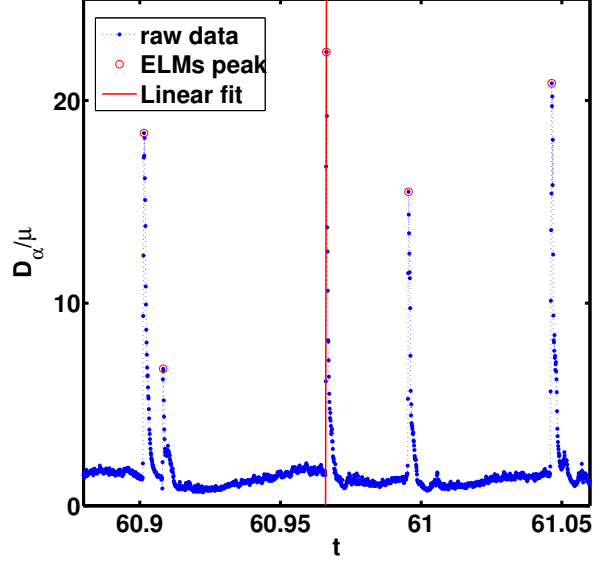


Figure 2.3: D_α line for JET plasma 57865. ELMs are steep and narrow in time. In this particular case the time width is 5.5ms. A linear fit of the point used for selection shows a slope $m = 8.13 \times 10^4$.

With higher statistics[Murari et al., 2014] we may typically observed long lived trends, but the nonlinearity and its usually fast response can be absorbed in the averages of quantities. In our collaborative work, independent algorithms have shown no substantial change for the ELM detection [Calderon et al., 2013; Chapman et al., 2014, 2015; Webster et al., 2014].

A fitted time window where stationarity is better conserved was key in refining the number of ELMs in signal like plasmas 57865, 57867, 57869 shown in Fig. 2.4. A more stable time windows can reduce dramatically the number of ELMs per plasma, at the start and the end of the time series they are neglected, specifically where the Gas puffing rate is raised to reach the H-mode, and decrease when the discharge is finished. By simply creating shorter time windows of similar gas puffing rate in every discharges we can have a

better estimation of the underlying process, other key parameters may need similar investigation.

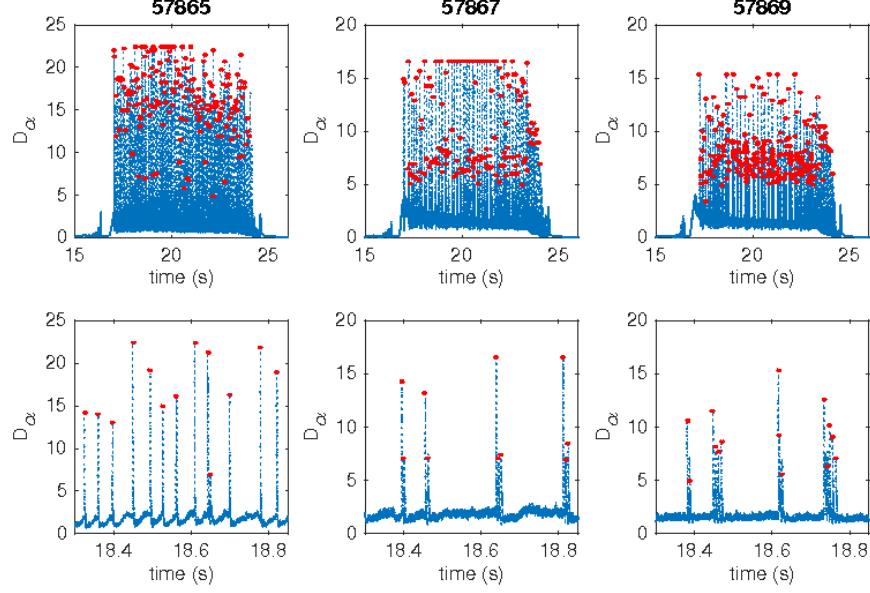


Figure 2.4: The ELM time series for shots 57865(left), 57867(centre), and 57869(right). The top panels show the full time series for $t = 15 - 25$ s. The bottom panels highlights $t = 18.3 - 18.8$ s in order to show clearly which features of the time series are being detected as type-I ELMs.

Delay plots

The new ELM time series is X_{ELM} with times t_n taken at the ELM's peak and N is the number of events. The time interval between successive events, waiting times, is obtained by taking the difference between the times t_n for each event.

$$\delta t_n = t_{n+1} - t_n \quad (2.6)$$

Delay plots are then obtained by plotting the waiting times δt_{n+i} against δt_n , with lag times $i = 1 \dots N - 2$. An indication for optimal lag times may be inferred from the auto-correlation function of the series $x(t)$ running a broad range τ . In Fig. 2.5 the same reference JET plasmas (as in Fig. 2.4) are plotted with delay coordinate δt_{n+1} vs. δt_n . We also test the new series X_{ELM} with a

histogram and fit a Gaussian probability distribution.

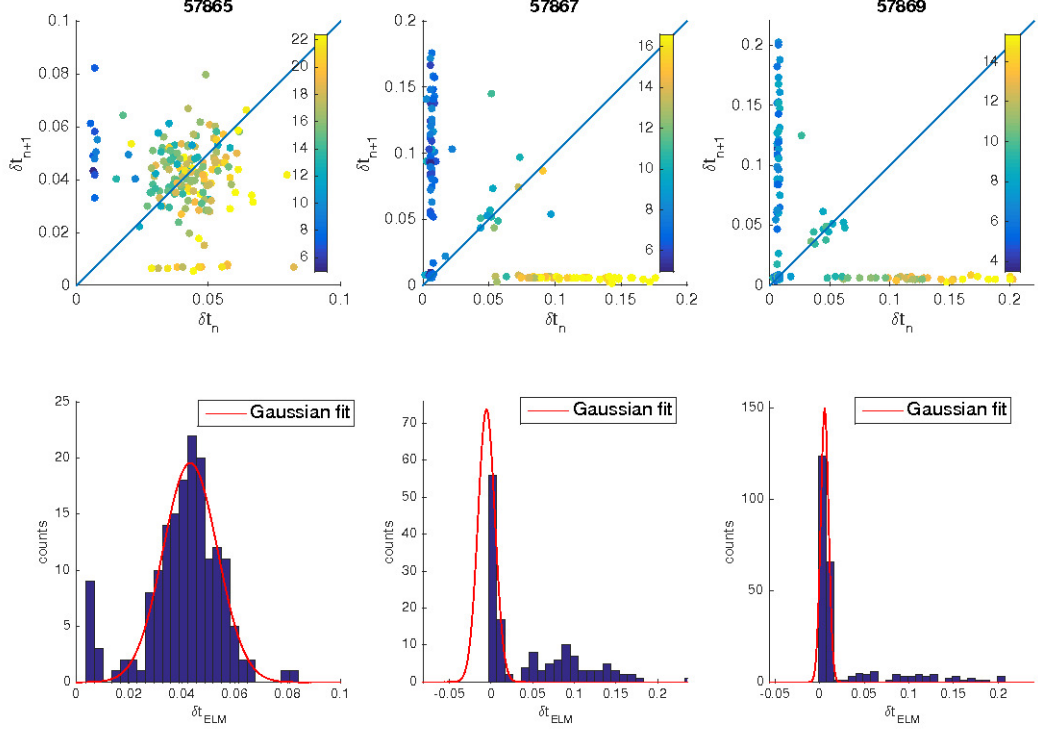


Figure 2.5: Delay plots for shots 57865(left), 57867(centre), 57869(right). The top panels show delay plots of δt_{n+1} against δt_n colour-coded by their ELM amplitude. The clustering of points near the horizontal and vertical axis means that in average the range of waiting time expected after a shorter waiting time is larger. The bottom panels are histograms of the waiting times values with a Gaussian fit.

Misidentified ELMs

In some cases an ELM can be misidentified. This can be seen in Fig. 2.6 where wrong detection can create added noise. In higher statistics above thousands ELM events [Webster and Dendy, 2013; Murari et al., 2014] wrong detection gets absorbed by the averages of the quantities. Because typically ELM detection is based on treating the ELM as nonlinear outlier beyond several standard deviations, as it can occur to have wrong populations introduced via misidentification.

Sometimes, because of the saturated amplitude a few double peaks ELMs are also detected right next to each other. The algorithm misidentification can sometimes be wrongly identified as compound-ELMs. The compound-ELMs are real ELMs occurring very sharply, one after another, or sometimes just two, as in Fig. 2.6 (*left*), whereas the second ELM near the first big ELM is a wrong detection in Fig. 2.6 (*right*).

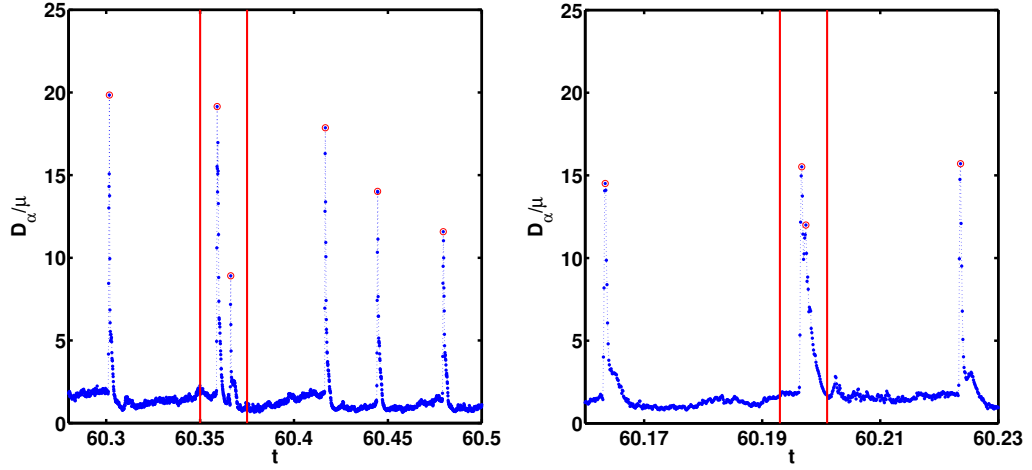


Figure 2.6: ELMing in JET-57865 and JET-57870, respectively, with red round marked ELMs. *Left*: ELMs inside vertical lines exemplify a compound-ELM. *Right*: a misidentified double-peak selection.

2.2.2 JET data system

The Joint European Torus (JET) is currently the most powerful tokamak and the focal point of the European fusion research programme. The new data storage and retrieval system for JET data took place in June 2001 [Layne and Wheatley, 2002]. The JET data warehouse consist mainly of two major frameworks: the JET Pulse File (JPF) server, and the Processed Pulse File (PPF) system. With the new infrastructure two main aspects can be highlighted: first, it allows for users to remotely access the data and secondly it centralizes the access through one standard API for data retrieval and writes. The new system is compatible with former Fortran API for user access in most mainstream open-source and proprietary software, for instance: IDL, Matlab,

MDSPlus, Python, and more. Because of the higher data creation rate, there are years of available data, it was already known to be more than 1GB per plasma discharge when the new system was implemented [Layne and Wheatley, 2002] and now this value has been increased not only with the addition of new diagnostics, but with higher resolution data. For the purposes of future work, understanding the database API and the relevant technologies is crucial, as well as the experimental databases containing extracts of experimental data from every JET plasma experiment. The Data and Coding Team at JET is currently developing a new interconnected Web and Python interfaces to access the data. The system is being developed to allow for selective criteria queries. The ‘JET dashboard’ is the name of the project, which is only a few months old and is running in beta mode for the moment, where the Web framework is partially available.

2.3 Hybrid Simulation Methods

2.3.1 Introduction

When the gap between theory and experiment exists we can benefit from numerical simulations. In plasmas where the ion scales are far more relevant than electron scales, we can use the hybrid model of plasmas [Winske, 1985] under this assumption. Kinetic/hybrid simulation involves the kinetic description of positive charges particles and the fluid description for electrons. The Maxwell’s equations are solved for time evolution, based on self-consistent sources, densities, and currents. These quantities in turn evolve from the variations in the fields and continue to change the fields around. In Fig. 2.7 we can see the basic steps for the evolution of any kinetic/hybrid computer simulation. Typically, the particle motion is advanced in a small time step, Δt , then the sources are collected to solve the fields, once the fields are obtained the particles can be move again and the cycle repeats.

2.3.2 Equations system and approximations

The hybrid model describes a plasma using a different treatment for the plasma components [Winske, 1985]. It is mainly concerned with a intermediate descrip-

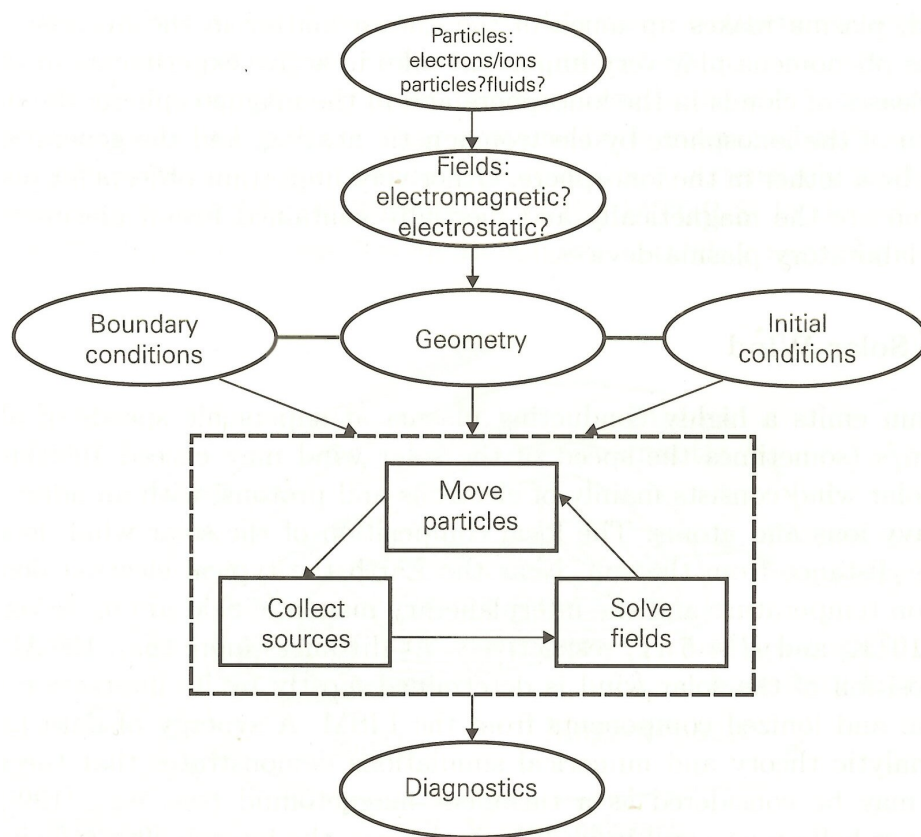


Figure 2.7: Basic steps in kinetic particle/hybrid simulations, reproduced from [Winske and Omidi, 1996].

tion between full particle and fluid-MHD models. In the model, all the ions species s are treated as particles and the particle-in-cell (PIC) scheme is used to solve the fields at grid points as the particles evolve in their motion. On the other hand, the electrons are described as a massless charge neutralising fluid. This massless approximation is characterized by dropping the electron inertia term, as described in Section 1.4.7. The main implication of this assumption is the unstable growth of the whistler mode, which requires smoothing of the fields using a low-pass frequency filter, see Section 2.3.8. The system is then described by the set of equations (2.7) as follows,

$$\frac{d\mathbf{x}_s}{dt} = \mathbf{v}_s \quad (2.7a)$$

$$m_s \frac{d\mathbf{v}_s}{dt} = q (\mathbf{E} + \mathbf{v}_s \times \mathbf{B}) \quad (2.7b)$$

$$\frac{\partial \mathbf{B}}{\partial t} = -\nabla \times \mathbf{E} \quad (2.7c)$$

$$\nabla \times \mathbf{B} = \mu_0 \mathbf{J} \quad (2.7d)$$

$$n_e m_e \frac{d\mathbf{u}_e}{dt} = -n_e e \mathbf{E} + \mathbf{J}_e \times \mathbf{B} - \nabla p_e \quad (2.7e)$$

$$p_e = n_e k_B T_e \quad (2.7f)$$

The subscript s is for multiple ion species. The ion position \mathbf{x}_s , ion velocity \mathbf{v}_s , ion mass m_s and charge q_s . The fields are, electric field \mathbf{E} , magnetic field \mathbf{B} , with magnetic permeability μ_0 and current density \mathbf{J} . The electron fluid velocity \mathbf{u}_e , number density n_e , and electronic charge e are put together into the electronic current density $\mathbf{J}_e = -en_e \mathbf{u}_e$, and the electron mass is m_e . The thermodynamic equation of state, Eq. (2.7f) is described by the electron fluid pressure where k_B is Boltzmann's constant and the electron temperature T_e . In Eq. (2.7d) we have made use of the Darwin's approximation, which neglects the displacement current. In this low frequency long wavelengths limit all the high frequencies modes for frequencies higher than electron cyclotron frequency are neglected. Eq. (2.7e) is the equation of motion for the electron fluid. The collective quantities evaluated for each species are defined as follows,

$$n_s = \int f_s(\mathbf{x}_s, \mathbf{v}_s) d\mathbf{v}_s \quad (2.8)$$

$$(n\mathbf{u})_s = \int \mathbf{v}_s f_s(\mathbf{x}_s, \mathbf{v}_s) d\mathbf{v}_s \quad (2.9)$$

$$\mathbf{u}_s = (n\mathbf{u})_s / n_s \quad (2.10)$$

$$\varrho_c = \sum_s n_s q_s \quad (2.11)$$

$$\varrho_m = \sum_s n_s m_s \quad (2.12)$$

$$\mathbf{J}_s = q_s n_s \mathbf{u}_s \quad (2.13)$$

$$\mathbf{J}_i = \sum_s \mathbf{J}_s \quad (2.14)$$

$$\mathbf{J} = \mathbf{J}_i + \mathbf{J}_e \quad (2.15)$$

We denote the particle number density n_s and the species ‘velocity density’ $(n\mathbf{u})_s$ where $f(\mathbf{x}_s, \mathbf{v}_s)$ is the probability distribution function of individual ion species s , with particles mass m_s , charge q_s . The species fluid velocity \mathbf{u}_s , charge density ϱ_c , mass density ϱ_m , the species current density \mathbf{J}_s , and ionic current density \mathbf{J}_i . The assumption that electrons are a massless charge neutralizing fluid implies that $m_e \approx 0$ and $\varrho_c = en_e$, so charge neutrality is present in the following condition, $n_e e \approx \sum_s n_s q_s$. From Eqs. (2.7d), (2.7e) and (2.15) we can recover the following expression for the electric field.

$$\mathbf{E} = -\frac{\mathbf{J}_i \times \mathbf{B}}{\varrho_c} + \frac{(\nabla \times \mathbf{B}) \times \mathbf{B}}{\mu_0 \varrho_c} - \frac{\nabla p_e}{\varrho_c} \quad (2.16)$$

We observe that $\mathbf{E} = \mathbf{E}(\varrho_c, \mathbf{J}_i, \mathbf{B}, T_e)$ does not depend explicitly of time, and so it can be obtained at each time step via its independent variables. Finally, if we substitute Eq. (2.16) into Eq. (2.7c) we obtain,

$$\frac{\partial \mathbf{B}}{\partial t} = \nabla \times \frac{\mathbf{J}_i \times \mathbf{B}}{\varrho_c} - \nabla \times \frac{(\nabla \times \mathbf{B}) \times \mathbf{B}}{\mu_0 \varrho_c} \quad (2.17)$$

The first term of Eq. (2.17) describes induction, and the second term dispersion. The electron pressure in Eq. (2.7f) does not influence the magnetic field evolution.

The following quantities are of general interest to understand and de-

scribe the plasma state. First, the magnetic pressure, as defined in section 1.5, ionic pressure per species s , and total pressure p_i ;

$$p_{mag} = B^2/2\mu_0 \quad (2.18)$$

$$p_s = \varrho_{m,s}(v_{th}^2)_s/2 \quad (2.19)$$

$$p_i = \sum_s p_s. \quad (2.20)$$

Here, v_{th} is the ion thermal speed, and we can use the previous definitions, plus Eq. (2.7f), to set the following plasma betas,

$$\beta_s = \frac{p_s}{p_{mag}} = \frac{(v_{th}^2)_s}{v_A^2} \frac{\varrho_{m,s}}{\varrho_m} \quad (2.21)$$

$$\beta_i = \sum_s \beta_s \quad (2.22)$$

$$\beta_e = \frac{p_e}{p_{mag}} = \frac{2n_e k_B T_e}{\varrho_m v_A^2} \quad (2.23)$$

where v_A is the Alfvén speed $v_A^2 = B^2/\mu_0\varrho_m$. Finally, we define the sound speed in terms of the plasma betas.

$$c_s^2 = \frac{(p_i + p_e)}{\varrho_m} = \frac{1}{2} (\beta_i + \beta_e) v_A^2 \quad (2.24)$$

The fastest mode present in the hybrid model, the 'whistler' mode, has a natural resonance occurring at the limit when this is close to the electron gyro-frequency Ω_e . Because the hybrid model allows for its unstable growth and we require a numerical control, preventing these modes to grow unstable, which is non-physical and brakes the CFL condition, see Section 2.3.8.

2.3.3 Normalization

The equation system Eq. (2.7) is normalized according to the following quantities: in a multi-species plasma, units are in terms of a reference plasma of protons with mass m_p and charge e , which has a mass density ϱ_{m0} . In this reference plasma, the proton number density is $n_0 = \varrho_{m0}/m_p$. Dimensionless simulation values are related to physical values by $s = x/u$, where s is a sim-

ulation variable, x is the corresponding physical variable, and u is a physical unit value. The list of units is,

mass density	ϱ_{m0}	
mass	$\varrho_{m0} \times (\text{unit of length})^3$	
magnetic field	B_0	Background field
unit of speed	v_A	Alfvén speed
unit of length	$v_A/\Omega_i = c/\omega_{pi}$	Ion inertial length
unit of time	Ω_i^{-1}	cyclotron time
charge density	$n_0 e$	
unit of charge	$n_0 e \times (\text{unit of length})^3$	
electric field	$v_A B_0$	
unit of energy	$\varrho_{m0} (v_A/\Omega_i)^3 v_A^2$	

Table 2.1: Normalization units of the hybrid code used in the plasma simulations in Chapter 4.

In the above definitions, c is the speed of light, the gyrofrequency $\Omega_i = eB_0/m_p$, and the ion plasma frequency $\omega_{pi}^2 = n_0 e^2 / \epsilon_0 m_i$. In terms of these units the proton charge-to-mass ratio is unity. In the simulations, the magnetic permeability, ionic and electronics betas, and sound speed are considered in the following way,

$$\mu_0 = 1, \quad \beta_s = \varrho_m^s (v_{th}^2)_s, \quad \beta_e = 2\tau_e, \quad c_s^2 = (\beta_i + \beta_e)/2 \quad (2.25)$$

where $\tau_e = k_B T_e / e$ is a measure of the electron temperature, then $p_e = \varrho_e \tau_e$ by definition.

2.3.4 Numerical scheme

Hybrid codes have been employed to simulate space plasma for more than three decades [Harned, 1982; Winske, 1985; Winske and Omid, 1996], and only recently have been applied to fusion plasmas [Gingell et al., 2012, 2013; Carbajal et al., 2014]. The three main types of solver include: a direct solver [Lipatov, 2002], the predictor-corrector method scheme [Colella, 1990; Saltzman, 1994], and algorithms based on the moment method [Winske and Quest, 1988; Matthews, 1994]. Hybrid codes similarity with PIC codes comes from the same

argument in which the phase space density is constant along the particle trajectories in absence of collisions. This principle

is known as Liouville's theorem. In this collisionless case, the spatial and velocity components map forward the distribution function conserving its phase space density. The advance of particles is done by using the current advanced method (CAM) [Matthews, 1994], which is a variation of the moment method [Winske and Quest, 1988].

The magnetic field is advanced using Faraday's law and using the electric field as a source at a defined time. The spatial derivatives are approximated by finite-differences in an interlaced grid [Yee, 1966]. In this grid some quantities are defined with half-integer at cell centres (\mathbf{E} , ϱ_c , \mathbf{J}) and others at cell nodes with full-integer (\mathbf{B}), then $n_x \Delta x$ is the full-integer domain and $(n_x + 1/2) \Delta x$ is the half-integer domain representing the interlaced grid points in one dimension, where Δx is the cell size, and n_x is the number of grid points.

The electric field can be derived from the ions velocity moments and currents, which means that \mathbf{E} can be obtained from the ions density, ions bulk velocity/current, and \mathbf{B} at a given time, without the need to integrate \mathbf{E} in time. Furthermore, existing hybrid codes differ in their approach on how to solve the fields interdependence in a numerically stable and accurate way. Our work here involves the use of *Hypsi*, a hybrid code that uses the CAM-CL algorithm [Matthews, 1994] and the MPI libraries for domain parallelization. The numerical scheme of the algorithm is focused in its majority on the following aspects: numerical integration of particle velocities and positions solving the Vlasov equation, time integration of the magnetic fields and advance of ions moments and currents with the subsequent update of the electric field for the new currents, a more comprehensive cycle is explain in Fig. 2.9 with all the simulation steps.

It is important to note that 'particles' are not ions, but macroparticles, each representing a very large number of ions. Therefore, the distribution function is effectively discretized into a finite number of ion clouds with centres \mathbf{x}_s , see Fig. 2.8, where $s = 1, 2, \dots, N$ and N is the total number of particles in the simulation. The discretization of the phase space introduces noise into the moment arrays. A consequence is that there is always a noise level in the density and currents acting as a source of small perturbations. Therefore, any-

thing with physical meaning smaller than the noise is lost, unless the number of particles is very great. The statistical noise intrinsic in PIC simulations depends on the number of macroparticles N present in the box and it is inversely proportional to the square root of the number of particles per cell, i.e. in a 100 particles per cell simulation we must increase the number to 400 to only half the noise, but then the total number of particles will be four times bigger, therefore decreasing the noise an order of magnitude clearly is impossible to provide in most HPC system nowadays.

Cloud shape and weighting function

For particles and field interpolation a cloud function of shape $S(x, x')$ and weighting function $W(x, x')$ is introduced [Hockney and Eastwood, 1988]. The finite size particle distribution might be written as in Birdsall and Langdon [1975],

$$f_c(\mathbf{x}, \mathbf{v}, t) = \int f(\mathbf{x}, \mathbf{v}, t) S(x, x') dx' \quad (2.26)$$

The cloud shape $S(x')$ of a particle with unit charge represent its charge density, and x' measures the distance from the centre of the particle. The fraction of the charged assigned from a particle with shape S at mesh point x_p is given by the overlap of the cloud shape with the cell p as follows,

$$W_p(x) = \int_{x_p-h/2}^{x_p+h/2} S(x' - x) dx' \quad (2.27)$$

Most common cloud shapes and weighting function are, the nearest grid point (NGP), cloud-in-cell (CIC), see Fig. 2.8, and triangular-shaped density (TSC) [Hockney and Eastwood, 1988]. The cloud and assignment functions must satisfy the charge conservation condition:

$$\sum_{i=1}^{N_g} W(x_i - x) = 1 \quad \text{and} \quad \int S(x' - x) dx = 1 \quad (2.28)$$

Also, weighting in three dimensions must take the form [Hockney and Eastwood, 1988]

$$W(\mathbf{x}) = W(x, y, z) = W(x)W(y)W(z) \quad (2.29)$$

to obtain continuity of value (first order), continuity of value and derivative

(second order), and higher order everywhere.

The effect of gridding the fields, which is assigning values to fields at grid points by weighted sum over particles, reduced the amount of computation and memory. Given,

$$\mathbf{E}(\mathbf{x}_s) = \sum_j W_{sj} \mathbf{E}(\mathbf{x}_j^E) \quad (2.30)$$

$$\mathbf{B}(\mathbf{x}_s) = \sum_j W_{sj} \mathbf{B}(\mathbf{x}_j^B) \quad (2.31)$$

where \mathbf{x}_j^E and \mathbf{x}_j^B are positions of grid points in E-grid (half-integer) and B-grid (full-integer) and $W_{sj} = W(\mathbf{x}_s, \mathbf{x}_j)$ is the weighting function associated to particle positions x_s .

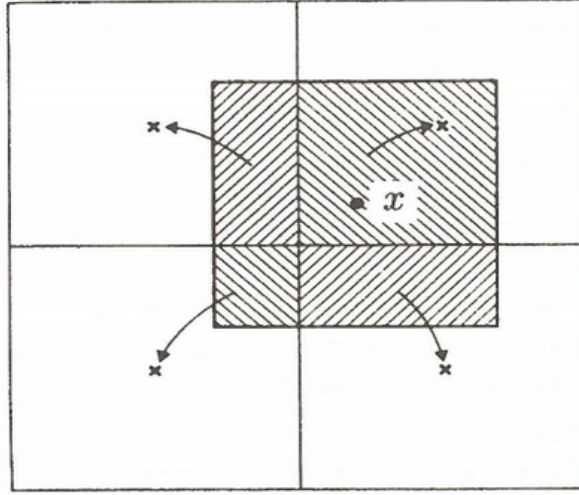


Figure 2.8: The two-dimensional CIC or area-weighting scheme. The fraction of charge assigned to the four neighbouring mesh points from a particle at position x is given by the area of overlap of its cloud shape with the cells containing those neighbouring mesh points.

2.3.5 Current Advance Method

In this method the variables \mathbf{x} and \mathbf{v} are advanced alternately. A time step Δt is introduced and the variables are evaluated at different time levels denoted

by superscripts, for example: $\mathbf{x}^{n+1} = \mathbf{x}((n+1)\Delta t)$. The differential Eqs. (2.7a) and (2.7b) are rewritten as difference equations,

$$\mathbf{x}^{1/2} = \mathbf{x}^{-1/2} + \Delta t \mathbf{v}^0 \quad (2.32)$$

$$\mathbf{v}^1 = \mathbf{v}^0 + \Delta t \frac{q_s}{m_s} \left(\mathbf{E}^{1/2}(\mathbf{x}^{1/2}) + \mathbf{v}^{1/2} \times \mathbf{B}^{1/2}(\mathbf{x}^{1/2}) \right) \quad (2.33)$$

We first observe the need to do an extra particle ‘push’ given the problem of having to solve Eq. (2.33) without having $\mathbf{v}^{1/2}$ neither $\mathbf{E}^{1/2}$. Using the similar time centred integration in 2.33 to the second order in Δt by making a first-order half-step from \mathbf{v}^0 to $\mathbf{v}^{1/2}$

$$\mathbf{v}^{1/2} = \mathbf{v}^0 + \frac{\Delta t}{2} \frac{q_s}{m_s} (\mathbf{E}_*^{1/2} + \mathbf{v}^0 \times \mathbf{B}^{1/2}) \quad (2.34)$$

For the ‘pre-push’ of particles a mixed time level electric field is required $\mathbf{E}_*^{1/2} = \mathbf{E}(\varrho_c^{1/2}, \mathbf{J}_i^0, \mathbf{B}^{1/2}, T_e)$. This is fixed by the advance of the ionic current density \mathbf{J}_i^0 a half-time step to $\mathbf{J}_i^{1/2}$ with an appropriate equation of motion. Now, only one pass through the particle velocity is necessary to solve Eq. (2.33), since $\mathbf{E}^{1/2}$ is computed as a function of $\mathbf{J}_i^{1/2}$. This is called the moment method [Winske and Quest, 1988], and almost half the computing time because of the minor number of grid points compared to push all the particles twice. Since the ionic current density is the quantity advanced this method is called current advance method [Matthews, 1994].

Current and charge densities are defined analytically by taking the moments of the distribution function $f(\mathbf{x}, \mathbf{v})$. They are determined at the grid points $\mathbf{x}_s^{1/2}$ by their weighted sum over the particles \mathbf{x}_j . A weighting function $W_{sj}^{1/2} = W(\mathbf{x}_s^{1/2}, \mathbf{x}_j)$, where $W_{sj} = W_{js}$ and each particle has unit weight, see Eq. (2.28). Ionic charge and current density are collected at grid points as,

$$\varrho_c(x_j) = \sum_s W_{sj}^{1/2} q_s \quad (2.35)$$

$$J_i(x_j) = \sum_s W_{sj}^{1/2} q_s v_s \quad (2.36)$$

with particles and velocities defined at different times, then \mathbf{J}_i has velocities at the beginning of the time step \mathbf{v}_s^0 , and positions at its midpoint $\mathbf{x}_s^{1/2}$. The ‘free-streaming’ [Friedman et al., 1991] ionic current is defined for Eq. (2.36)

as follows,

$$\mathbf{J}_i^*(\mathbf{x}_s^{1/2}, \mathbf{v}_s^0) = \sum_s W(\mathbf{x}_s^{1/2}) q_s \mathbf{v}_s^0 \quad (2.37)$$

where \mathbf{x}_s and \mathbf{v}_s refer to all the particles and all the i to all the grid points.

Advancing the Ionic Current Density

An equation of motion is now derived for advancing \mathbf{J}_i to the midpoint of the time step. Multiply the ‘pre-push’ equation of motion Eq. (2.34) by the charge q_s , and sum the contributions of the terms at the grid point, using weights $W_{sj}^{1/2}$ evaluated at particle positions $\mathbf{x}_s^{1/2}$:

$$\sum_s W_{sj}^{1/2} q_s \mathbf{v}_s^{1/2} = \sum_s W_{sj}^{1/2} q_s \mathbf{v}_s^0 + \frac{\Delta t}{2} \sum_s W_{sj}^{1/2} \frac{q_s^2}{m_s} (\mathbf{E}_*^{1/2} + \mathbf{v}^0 \times \mathbf{B}^{1/2}) \quad (2.38)$$

$$\mathbf{J}_i^{1/2} = \mathbf{J}_i^* + \frac{\Delta t}{2} (\Lambda \mathbf{E}^{1/2} + \Gamma \times \mathbf{B}^{1/2}) \quad (2.39)$$

$$\Lambda = \sum_s W_{sj}^{1/2} \frac{q_s^2}{m_s} \quad (2.40)$$

$$\Gamma = \sum_s W_{sj}^{1/2} \frac{q_s^2}{m_s} \mathbf{v}_s^0 \quad (2.41)$$

where summation is done over ion species s .

2.3.6 Cyclic Leapfrog

The electric field is evaluated as a function of the time-centred charge and current densities, $\mathbf{E}_*^{1/2} = \mathbf{E}(\rho_c^{1/2}, \mathbf{J}_i^{1/2}, \mathbf{B}^{1/2}, T_e)$, where the field $\mathbf{B}(t_0)$ is advanced from t_0 to $t_0 + \Delta t$ in a cycle of n substeps of size $\delta t = \Delta t/n$, so that,

$$\begin{aligned} \mathbf{B}_p &= \mathbf{B}(t_0 + p\delta t), \\ \mathbf{B}_1 &= \mathbf{B}_0 - \delta t \nabla \times \mathbf{E}_0, \\ \mathbf{B}_2 &= \mathbf{B}_0 - 2\delta t \nabla \times \mathbf{E}_1, \\ &\vdots \\ \mathbf{B}_{p+1} &= \mathbf{B}_{p-1} - 2\delta t \nabla \times \mathbf{E}_p \end{aligned}$$

where $p = 1, 2, \dots, n - 1$. Also,

$$\begin{aligned}\mathbf{B}_n &= \mathbf{B}_{n-2} - 2\delta t \nabla \times \mathbf{E}_{n-1} \\ \mathbf{B}_n^* &= \mathbf{B}_{n-1} - \delta t \nabla \times \mathbf{E}_n\end{aligned}$$

and finally

$$\mathbf{B}(t_0 + \Delta t) = \frac{1}{2}(\mathbf{B}_n + \mathbf{B}_n^*) \quad (2.42)$$

Here, two copies of the magnetic field are used, one for the odd solution and one for the even solution, which leapfrog over each other. After n steps, defined during the initialization, the solutions are averaged.

Time-advanced Algorithm

In general, the sequence to move each step from t_0 to t_1 is made as shown in Fig. 2.9. The loop sequence is the following:

1. Advance \mathbf{B}^0 to $\mathbf{B}^{1/2}$, and $\mathbf{J}_i^*(\mathbf{x}^{1/2}, \mathbf{v}^0)$ to $\mathbf{J}_i^{1/2}$ and evaluate $\mathbf{E}^{1/2} = \mathbf{E}(\varrho_c^{1/2}, \mathbf{J}_i^{1/2}, \mathbf{B}^{1/2}, T_e)$, using Eqs. (2.39) to (2.41).
2. Advance \mathbf{v}^0 to \mathbf{v}^1 , and $\mathbf{x}^{1/2}$ to $\mathbf{x}^{3/2}$, using Eqs. (2.33) to (2.34).
3. Collect the moments in the same loop through the particle:

$$\begin{aligned}\varrho_c^{3/2} &= \varrho(\mathbf{x}^{3/2}) \\ \mathbf{J}_i^{*-} &= \mathbf{J}_i^*(\mathbf{x}^{1/2}, \mathbf{v}^1) \\ \mathbf{J}_i^{*+} &= \mathbf{J}_i^*(\mathbf{x}^{3/2}, \mathbf{v}^1) \\ \Lambda &= \Lambda(\mathbf{x}^{3/2}, \mathbf{v}^1) \\ \Gamma &= \Gamma(\mathbf{x}^{3/2}, \mathbf{v}^1).\end{aligned}$$

4. Obtain averages ϱ_c^1 and \mathbf{J}_i^1 and advanced $\mathbf{B}^{1/2}$ to \mathbf{B}^1 . \mathbf{B} is integrated in time by cyclic leapfrog, Eq. (2.42).

At the beginning and at the end of the simulations the positions and velocities are moved to the time level required by the CAM-CL algorithm [Matthews, 1994].

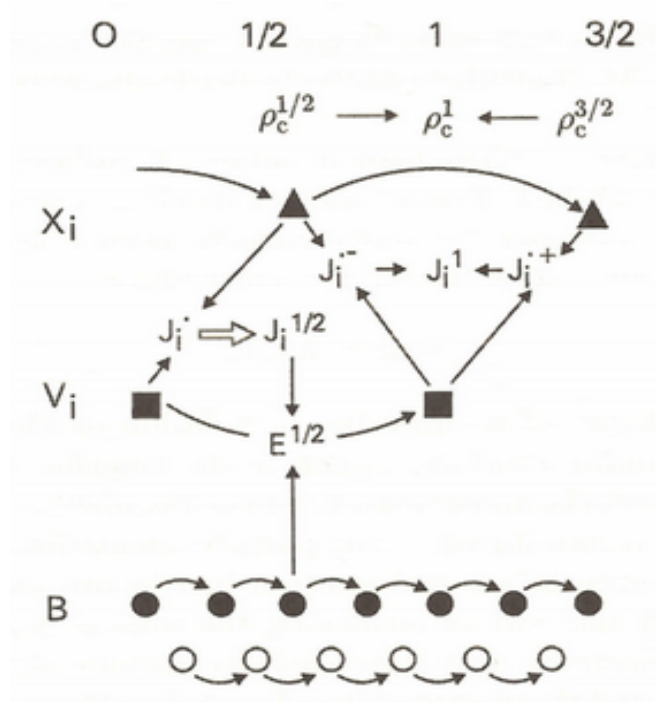


Figure 2.9: Schematic of the time advance scheme in CAM-CL. At the beginning of the step, \mathbf{x} has been advanced to time level $1/2$ with \mathbf{v}_0 . Moments already collected are $\rho_c^{1/2}$ and the ‘free-streaming’ ionic current density $\mathbf{J}_i^*(\mathbf{x}^{1/2}, \mathbf{v}_0)$, as well as ρ_c^0 and \mathbf{J}_i^0 . Two solutions of \mathbf{B} are advanced by substeps (cyclic leapfrog) to time level $1/2$, with $\mathbf{E}(\rho_c^0, \mathbf{J}_i^0, \mathbf{B}, T_e)$. The current advance method advances \mathbf{J}^* to $\mathbf{J}_i^{1/2}$, with the fields $\mathbf{B}^{1/2}$ and $\mathbf{E}(\rho_c^{1/2}, \mathbf{J}_i^0, \mathbf{B}^{1/2}, T_e)$. The time centred (for \mathbf{v}) electric field is now evaluated at time level $1/2$, $\mathbf{E}^{1/2}(\rho_c^{1/2}, \mathbf{J}_i^{1/2}, \mathbf{B}^{1/2}, T_e)$. The particles are pushed, $\mathbf{v}_0 \rightarrow \mathbf{v}_1$, $\mathbf{x}^{1/2} \rightarrow \mathbf{x}^{3/2}$, and the moments are collected, $\rho(\mathbf{x}^{3/2})$, from which ρ_c^1 is obtained as an average of $\rho_c^{1/2}$ and $\rho_c^{3/2}$; the backward and forward ‘free-streaming’ currents $\mathbf{J}_i^{*-}(\mathbf{x}^{1/2}, \mathbf{v}^1)$ and $\mathbf{J}_i^{*+}(\mathbf{x}^{3/2}, \mathbf{v}^1)$, which are averaged to obtain \mathbf{J}_i^1 . Finally, $\mathbf{B}^{1/2} \rightarrow \mathbf{B}^1$ and the cycle repeats, reproduced from Matthews [1994].

2.3.7 Particle loading

The loading of nonuniform distributions in space can be expressed as in Lipatov [2002]. Let us suppose that we need to place particles so as to form a density $d(x)$, from $x = a$ to $x = b$. The cumulative distribution function has the form

$$D(x) = \frac{\int_a^x d(x')dx'}{\int_a^b d(x')dx'}, \quad (2.43)$$

where $D(a) = 0$ and $D(b) = 1$. Equating $D(x_s)$ to a uniform distribution numbers ϵ_s , $0 < \epsilon_s < 1$, will produce x_s corresponding to the distribution $d(x)$. In cases where an analytic solution is not possible it is necessary to use a numerical method to solve $x_s = x_s(\epsilon_s)$ [Birdsall and Langdon, 1975]. The inversion problem to find a uniform plasma spatial distribution is simply provided through an analytic solution of Eq. (2.43).

Loading a Maxwellian velocity distribution

Let us use the system of coordinates which is located in the frame of the bulk velocity, $v = \mathbf{v}_{bulk}$. a normalized thermal (Maxwellian) distribution is shown in Fig. 2.10. Most of the particles are within the region inside $v = 3v_T$ (99%) so very often we do not need to place particles beyond 3 or $4v_T$. Keeping the particles with sufficiently high v may result in a strong decrease in the integration time step Δt due to Courant-Fridrich-Levy (CFL) condition, explained in next section. Let us suppose that the density is spatially uniform with the isotropic Gaussian distribution $f_0(\mathbf{v})$. Then the cumulative distribution function for the speed $v = |\mathbf{v}|$,

$$\epsilon_s = F(\mathbf{v}) = \frac{\int_0^v \exp\left(-\frac{v'^2}{2v_T^2}\right) d\mathbf{v}'}{\int_0^\infty \exp\left(-\frac{v'^2}{2v_T^2}\right) d\mathbf{v}'} \quad (2.44)$$

is set equal to a set of uniformly distributed numbers ϵ_s , varying from 0 to 1, in order to obtain the values of v . In the one-dimensional case, the integration over $f(v)$ cannot be explicitly done, but it is done numerically, as in [Birdsall and Langdon, 1975, INIT routine in ES1 code], to produce a quiet-Maxwellian distribution, with thermal velocity, v_T . In the case of two or three-dimensional

isotropic thermal distribution, the integration of Eq. (2.44) can be done explicitly. The speed is $v = \sqrt{v_x^2 + v_y^2}$, angle $\theta = \arctan v_y/v_x$, $d\mathbf{v} = 2\pi v dv$. The inversion for speed v obtained in terms of ϵ gives,

$$v_s = v_T \sqrt{-2 \ln \epsilon_s}. \quad (2.45)$$

Another set of uniform numbers ϵ_m is chosen for the angles θ , over the range 0 to 2π , $\theta_m = 2\pi\epsilon_m$. The third coordinate can be added by repeating one of the previous axis, although this is a debatable practise.

After all the particles are loaded, we can start moving, or setting the particles for time $\Delta t = 0$ and collect the moments and solve the fields at $t = 0$.

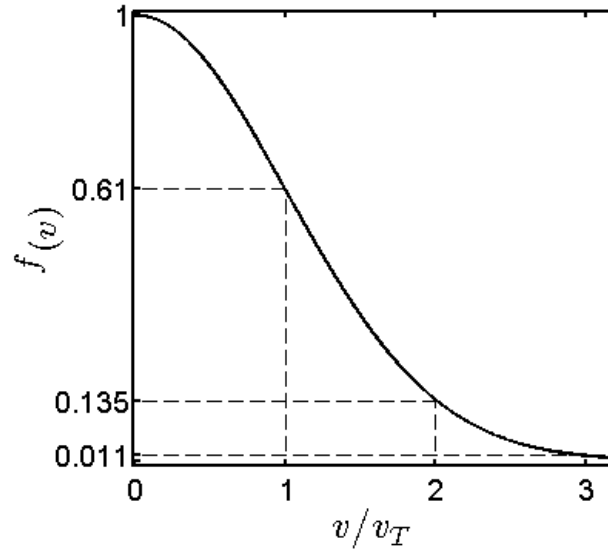


Figure 2.10: Normalized thermal velocity distribution.

2.3.8 Stability and CFL condition

The electric and magnetic fields are staggered in half-integer, full-integer, time step grid to conserve the Maxwell's laws[Birdsall and Langdon, 1975; Yee, 1966]. A stability condition can be derived in any PIC code from plane waves solution into the Maxwell's equations onto the grid[Courant et al., 1928].

Hence, for the scheme to be stable the following condition is necessary,

$$(c\Delta t)^2 < \left(\frac{1}{\Delta x^2} + \frac{1}{\Delta y^2} + \frac{1}{\Delta z^2} \right)^{-1} \quad (2.46)$$

$$\frac{v\Delta t}{\Delta x} < \frac{1}{\sqrt{3}} \quad (2.47)$$

This condition prevents information travelling faster than the limiting speed, crossing more than one cell in a single time step. The Eq. (2.46) is the Courant-Friedrichs-Levy (CFL) condition [Courant et al., 1928] which defines the maximum time step size to resolve the fastest characteristic velocity. For equal cell size $\Delta_x = \Delta_y = \Delta_z$ we obtain Eq. (2.47), where v is the characteristic fastest velocity in the system. In the hybrid model the speed of the whistler wave mode is the fastest to resolve.

From the generalized Ohm's law in Section 1.4.7 we retained the Hall term, responsible for the whistler mode, and the electron pressure term. In this regime we must resolve the ion motion with grid spacing usually smaller than the ion Larmor radius. In addition, the massless electron assumption left the whistler mode unbounded of the previous electron cyclotron cut-off. Altogether, impose a severe constrain on the choosing of the time step Δt [Pritchett, 2000]. For large wavenumber the whistler frequency scales as $\omega/\Omega_i = (k\delta_i)^2$, where δ_i is the ion skin depth. For the largest wavenumber $k_{max} = \pi/\Delta x$ the new CFL condition gives,

$$\Omega_i \Delta t < (\Delta x/\delta_i)^2 / \sqrt{n} \pi \quad (2.48)$$

where n is the number of spatial dimensions for the grid. To prevent this unstable growth a smoothing technique that works as a low-pass frequency filter in the frequency domain is applied. A low-pass filter passes signals with a frequency lower than a cut-off frequency, smoothing the higher frequencies above the cut-off. The amount of attenuation depends on the filter. The smoothing is done in the time domain by taking advantage of the convolution property which state that applying the filter in the frequency domain is equivalent to take the convolution with the inverse transform of the convolution filter. For a Gaussian filter where $g(x) = 1/\sigma$ for $|x| \leq \sigma/2$, and zero anywhere else. Then

we have,

$$g * f(x) = \int_{-\infty}^{\infty} g(a)f(x-a)da = \frac{1}{\sigma} \int_{-\sigma/2}^{\sigma/2} f(x-a)da \quad (2.49)$$

The effect of this integral is to take the average of all values of $f(x)$ in a neighbourhood of size σ around x . For a discrete weighted ε average in one-dimension of F in a neighbourhood Δx , the convolved quantity is,

$$(1 - \varepsilon)F\delta(x_s) + \frac{\varepsilon}{2} (F\delta(x_s + \Delta x) + F\delta(x_s - \Delta x)) \quad (2.50)$$

where $\delta(x)$ is the Dirac function, and F is the smoothed quantity. Note this is easily extendible to three dimensions, which is faster than the Gaussian convolution per grid point.

Round-off error

Computers arithmetic precision can lead to erroneous results, and often this is extended for large scientific computations. The binary numbering system (base-2 intrinsic in most computer) can be represented in the base-10 system and also using scientific notation. The number 126 in binary 01111110₂ representation and also,

$$\begin{aligned} 126 &= 1 \times 10^2 + 2 \times 10^1 + 6 \times 10^0 && \text{base-10} \\ &+ .126 \times 10^3 && \text{scientific notation} \end{aligned}$$

Using scientific notation the components are stored following the IEEE (Institute of Electrical and Electronic Engineers) convention for binary arithmetic. Single precision and double precision are the basics *floating point* or real numbers inside the machine. However, finite computing power implies that precision is finite to a certain value ϵ associated to different machines or technologies, and it is also different for single and double precision. The machine ϵ strongest implication is the *effective zero*, which means that the computer can not distinguish from $1.0 + \epsilon! = 1.0$ anymore and the calculation becomes seamless. The ϵ value for single and double precision in the HPC cluster used in Chapter 4 are $\sim 6 \times 10^{-8}$ and $\sim 10^{-16}$, respectively.

Chapter 3

Characterization of ELMs in JET plasmas

The results in this chapter are published in Calderon et al. [2013].

3.1 Parameter space and dimensionality

ELMs time series have been the subject of intensive study in different tokamak experiments in order to quantify and extract signatures of the underlying physical process or processes. Given the highly non-linear nature of these events [Greenhough et al., 2003; Ikonen and Dumbrajs, 2005; Zvejnieks et al., 2004] traditional linear analysis has been less successful in describing ELMs properties and only a few statistical quantities have been more robust in defining the ELMs global behaviour [Calderon et al., 2013; Chapman et al., 2014; Murari et al., 2014; Webster et al., 2014]. As our understanding of the phenomena improved correlation has been established between ELM frequency with change of several experimental parameters; collisionality [Zohm, 1996; Kamiya et al., 2007], pedestal pressure and temperature [Pitzschke et al., 2012; Saibene et al., 1999] and many other plasma parameters [Degeling et al., 2001; Hill, 1997; Connor, 1998]. A broader parameter space with increased dimensionality is then required to fully understand this phenomena. There has been focus on non-linear properties, relatively to one, two or more dimensions including collisionality, q-profile, Neutral Beam Injection (NBI) among others, to search for deterministic or chaotic behaviour [Degeling et al., 2001; Bak

et al., 1999; Martin et al., 2002; Ikonen and Dumbrajs, 2005]. In JT-60U early studies suggested the presence of Unstable Periodic Orbits(UPOs) based on their recurrence properties and the fixed point transform [Bak et al., 1999]. An unstable periodic solution in a chaotic dynamical system is characterized by a linear first-order perturbation as the system approach the UPO, and the subsequent exponentially growing perturbation as the system moves away from the unstable solution. In TCV a similar study was carried out to identify UPOs [Degeling et al., 2001; Martin et al., 2002]. It argued that the time delay between ELMs may be the result of noise only or must be a deterministic process as shown by the relative appearance of UPOs in the time series. The fluctuations in the time delay of continuous ELMs were found to be related to the variations of the external parameters such as plasma current I_p , elongation κ , and density n_e . While it has not been established whether the nature of the ELM waiting times is purely random mean-distributed[Adamov, 2008], neither this can be rejected as hypothesis, given the common episodes of single periodic with random spread, yet, these findings opened the door for the application of many different non-linear methods traditionally applied in others areas, for example see the review by Dendy et al. [2007]. In DIII-D observations of ELMs dynamic have focused on understanding the physics that independently controls the edge pedestal density and temperature gradients [Fenstermacher et al., 2005]. Simulation of ELMs using a MHD model [Huijsmans et al., 2015] have been partially successful in describing ELM dynamics, but they are not fully able to account for variations imposed by impurities, high densities with low pedestal collisionality for plasmas as in the ITER scenario, although nonlinear MHD simulations efforts exists [Fenstermacher et al., 2013]. In JET the Probability Distributions Functions (PDFs) of ELM bursts were analysed on a series of discharges to quantify the measured PDFs against a series of model distribution (Gaussian, inverse exponential, and Poisson) by Greenhough et al. [2003]. Also recently, Murari et al. [2014] provided an extensive statistical analysis of JET discharges with the old carbon wall containing thousands of ELM events, in mostly similar plasmas. Murari et al. [2014] tested several model distributions on a large set of JET discharges for ELM type-I and presented a tool (universal multi-event locator, UMEL) to facilitate the identification of ELM events. Defining a model distribution can help us to

understand the global ELM time response distribution directly correlating its changes with key experimental parameters. In addition, ELMs type-III were studied using model distribution in L-mode/H-mode plasmas characterizing them mainly with Weibull distributions according to the changes in the inter-ELM time difference [Webster, 2012]. A quantitative classification of ELMs statistical properties has been provided in several tokamaks, yet the use of non-linear techniques to study the strong correlation of the ELM phenomena with its parameter space has only recently been gaining attention [Calderon et al., 2013; Chapman et al., 2014, 2015; Webster et al., 2014; Murari et al., 2014]. Here we discuss the characterization of ELMs inter-event time difference according to the changes of and its dependence upon a key control parameter, the gas injection rate in otherwise similar plasmas. During the course of this thesis, the application of such studies has been recently investigated in real-time ELM frequency feedback control loop in JET by Lennholm et al. [2015].

3.2 Characterization of ELMs in low dimensional space

Ruelle and Takens [1971] discussed a classical scenario for the transition from ordered to disordered flow in fluids with increasing driving control parameter like those in Newhouse et al. [1978]; Trefethen et al. [1993]. This has been observed in Rayleigh-Bénard convection in fluids by Bodenschatz et al. [2000]; Ahlers [1974]; Gollub and Swinney [1975]; Gollub and Benson [1980]; Libchaber et al. [1983], and in drift wave turbulence by Klinger et al. [1997] and flute instabilities in plasmas [Brochard et al., 2006]. Oscillatory behaviour arises either if there is a constant of the motion, or if there is a limit cycle onto which the system dynamics is attracted in the presence of damping or dissipation. In the present case, where the system is the plasma undergoing the ELMing process, the nature and number of the relevant phase space co-ordinates is not known from first principles. Progress towards their identification can nevertheless be made by applying techniques of dynamical systems analysis to visualize changes in the topology of the phase space. A convenient method is that of ‘delay plots’, see Section 2.2.1, that is, to plot the successive time

intervals between crossings of a surface of section in the phase space[Matsoukis et al., 2000; Devine and Chapman, 1996; Schreiber and Schmitz, 2000]. Fig. 3.1 shows how we define a threshold here.

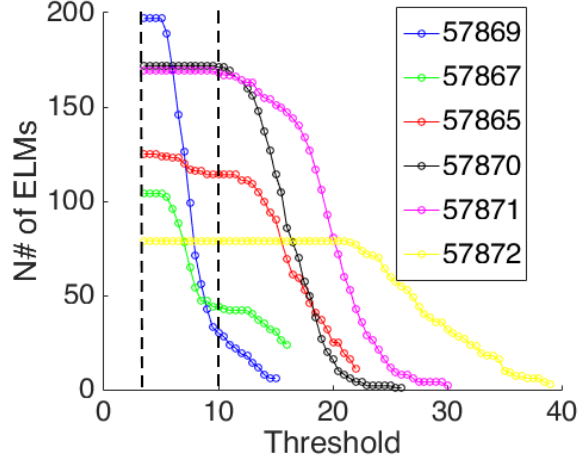


Figure 3.1: For six JET plasmas the counts of ELMs events as a function of the amplitude threshold (cut every 0.5 of normalized amplitudes). We observe the vertical dashed line at 3.5 separating noise level. The second vertical line, with amplitude value 10.0, is chosen to illustrate best the changes in delay plots (middle panel) of Figs. 3.3 and 3.4 according to the variations of the gas puffing rate in Fig. 3.5.

In this chapter we report the application of delay plots to the measured time intervals or inter-event times between successive ELMs. We consider ELM sequences from six similar plasmas in the JET tokamak, including JET plasma 57865 where the H-mode closely approaches an ITER operating regime with respect to some, but not all, key dimensionless parameters [Pamela et al., 2005]. We obtain evidence that Type I ELMing in these plasmas exhibits transitions between processes with distinct physical analogues, dependent on the value of the gas puffing rate as control parameter. In all six plasmas the toroidal magnetic field density is 2.7T, the plasma current is 2.5MA, neutral beam and ion cyclotron resonance heating power are 13.5MW and 2.0MW respectively, and the H_{98} confinement factor is in the range 0.87 to 1.0. In all six plasmas, gas puffing terminates at 23.3s and neutral beam heating is ramped down from 23.5 to 24.5s. The differences in Type I ELM character are largely determined by the different levels of externally applied gas puffing.

The intensity of the D_α signal, which sometimes saturates, is not necessarily a reliable proxy for the magnitude of the underlying ELM plasma phenomenon, whereas occurrence times are well defined. ELM occurrence and ELM inter-event times are the primary physical indicators addressed in the present study. The moment of occurrence of each ELM is inferred from the D_α datasets using an algorithm similar to that described in Greenhough et al. [2003]; Webster et al. [2014], which exploits the steep leading edge of each ELM. This procedure generates a sequence of event times t_n for each n th ELM, and hence inter-event times $\delta t_n = t_n - t_{n-1}$. These sequences are used to construct delay plots, which are known to capture aspects of the topology of the unknown underlying phase space evolution of the system [Schreiber and Schmitz, 2000; Matsoukis et al., 2000; Devine and Chapman, 1996].

3.2.1 Results and discussion

Figures 3.3 and 3.4 show measured Type I ELM signals for a sequence of six JET H-mode plasmas $578nm$, where nm is 72, 71, 70, 65, 67, and 69 in order of increasing magnitude and duration of the gas puffing rate, shown in Fig. 3.5, which is the key external control parameter. The upper trace in each panel of Figs. 3.3 and 3.4 plots the time-evolving intensity of Lyman alpha recombination radiation from deuterium, D_α , measured by a camera directed at the inner divertor, normalised by the mean measured intensity. The line of sight can be seen in Fig. 3.2. The two groupings of three plasmas are at lower (Fig. 3.3) and higher (Fig. 3.4) gas puffing rates. At lower gas puffing rates (Fig. 3.3) the ELM signal intensity is roughly the same across each time series, whereas at higher gas puffing rates (Fig. 3.4) this shows a rich structure. We will investigate this structure by sorting the ELM events that are used to construct the time series of inter-ELM time intervals (delay times), in terms of whether they exceed a threshold in signal intensity, see Fig. 3.1 threshold line is plotted against number of ELMs used for choosing best threshold cut; the thresholds used (3.5 and 10 ELM amplitude) are indicated by horizontal lines on the ELM time series (top panel in Figs. 3.3 and 3.4). Each n th Type I ELM that has signal intensity exceeding a given threshold then forms a set of events at time t_n with the delay between events $\delta t_n = t_n - t_{n-1}$. The middle

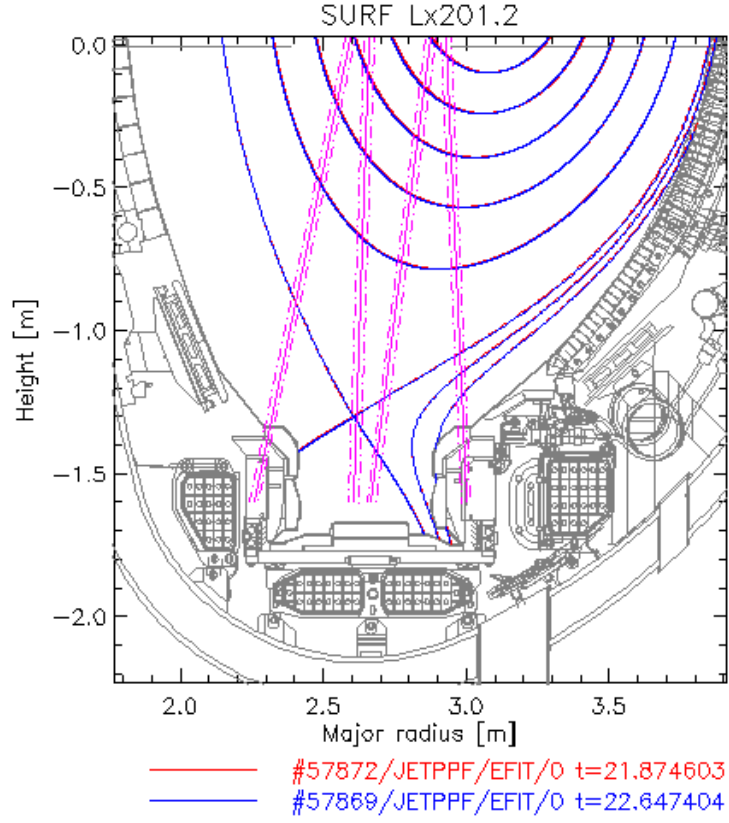


Figure 3.2: Diagram of the JET vessel in poloidal cross section showing divertor (bottom) and walls (grey structure). The line of sight of D_α radiation emission at 656[nm] in vertical lines is pointing to the inner and outer divertor spanning across multiple channels, as shown by the broadening of line limits. At the top, magnetic flux surfaces from EFIT equilibrium reconstruction of JET plasmas 57872 and 57869 at $t \approx 22$ s.

panels of Figs. 3.3 and 3.4 show the delay plots for a given threshold, that is, δt_{n+1} versus δt_n .

The D_α signal intensity for the ELM at t_n is indicated by colour coding. While these delay plots reflect the topology of the system phase space they are not a phase space reconstruction. For a trajectory that is approximately singly periodic the delay plot will exhibit a single concentration of points on the $\delta t_{n+1} = \delta t_n$ line, centred on the mean period $\tau = \delta t_{n+1} = \delta t_n$, as shown in Section 2.2.1. The spread of points about the mean period reflects a combination, in unknown proportions, of intrinsic and extrinsic sources of irregularity in a quasi-regular process, and determines the practical resolution limit of this method. A period-two oscillation will generate two concentrations of points, symmetrically placed either side of the $\delta t_{n+1} = \delta t_n$ line. Dynamical switching between one period τ_1 and another at τ_2 will generate four concentrations of points: at the two distinct periods τ_1 and τ_2 on the $\delta t_{n+1} = \delta t_n$ line, and at two locations symmetrically placed either side of the line, at $(\delta t_{n+1}, \delta t_n)$ coordinates (τ_1, τ_2) and (τ_2, τ_1) .

The number of ELMs evaluated in these six JET plasmas ranges between 79 and 197. The mean inter-ELM time interval is in the range 25 to 60ms. The delay plots in Fig. 3.3 are insensitive to the threshold, in marked contrast to Fig. 3.4, suggesting that these reflect distinct processes. In Fig. 3.3, plasmas with successively greater gas puffing rates are shown from left to right. We can see that increased gas puffing causes the ELMing process to bifurcate from singly periodic (57872), via transitional behaviour (57871), to a situation where two periods are present (57870) together, with the plasma switching between them. This behaviour is approximately analogous to that of small amplitude oscillations of two weakly coupled pendulums with different natural frequencies. It is also apparent that a longer delay time δt_n before an ELM correlates statistically with a larger D_α signal intensity. The bottom pair of plots in each panel of Figs. 3.3 and 3.4 displays the probability density functions (PDFs) for the distributions of measured δt_n for the ELM time series using the same amplitude thresholds as for the delay plots; in Fig. 3.3, unlike Fig. 3.4, these two panels are identical.

We now turn to Fig. 3.4 which corresponds to higher overall levels of gas puffing rate. It displays a transition in the ELMing process as the gas

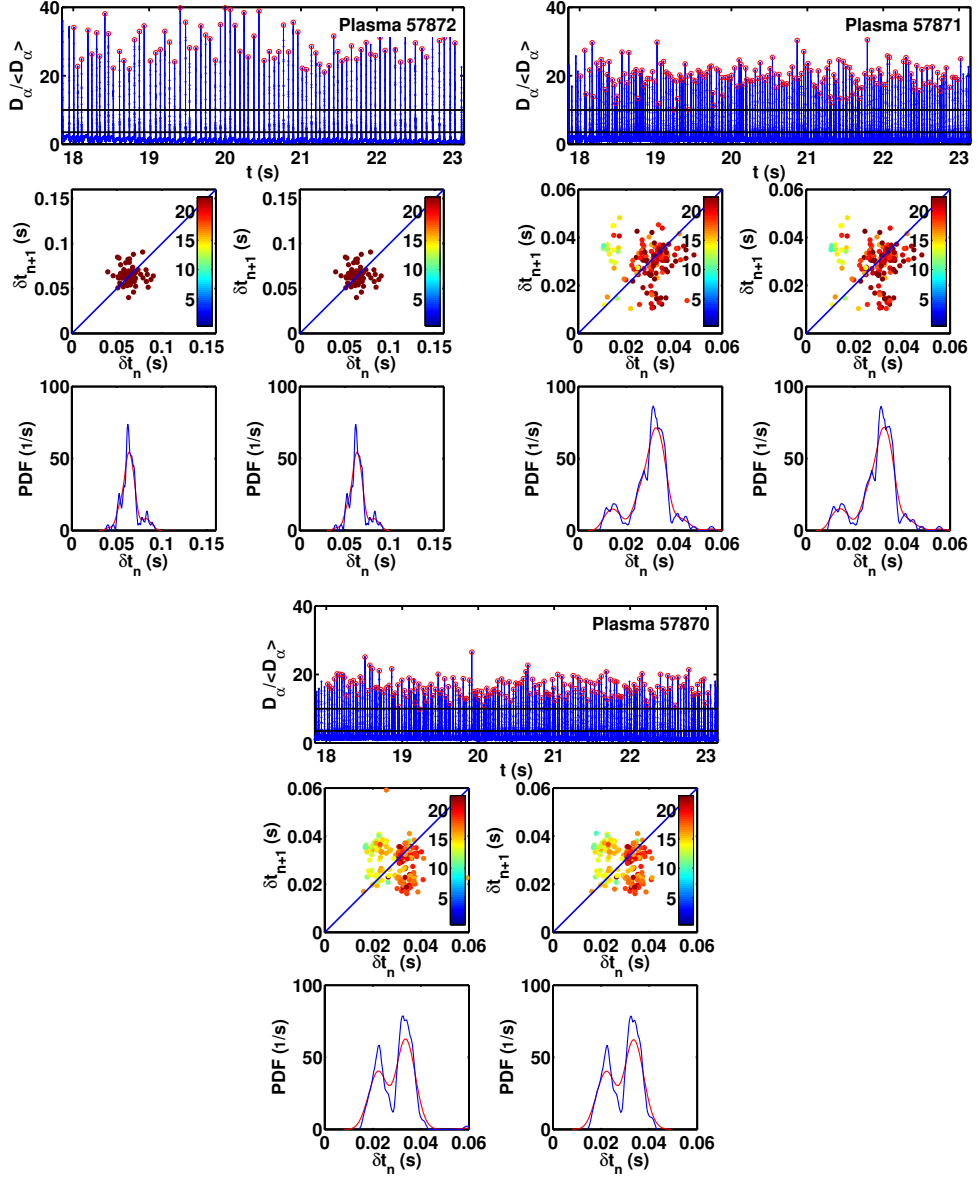


Figure 3.3: ELM characteristics of three similar JET plasmas 57872, 57871, 57870 at lower gas puffing rates, showing for each plasma: (top of each panel) the time trace of D_α signal intensity, displaying also the two amplitude thresholds used for the centre and bottom plots; (centre of each panel) delay plots for ELMs, with amplitude colour coded above the higher (lower) threshold on the left (right); (bottom of each panel) corresponding probability density functions for the distributions of measured δt_n for the ELM time series, using the same amplitude thresholds as for the delay plots; the red and blue curves represent different binning of the same data. The three plasmas are ordered, from the left, in terms of increasing magnitude of gas puffing, see Fig. 3.

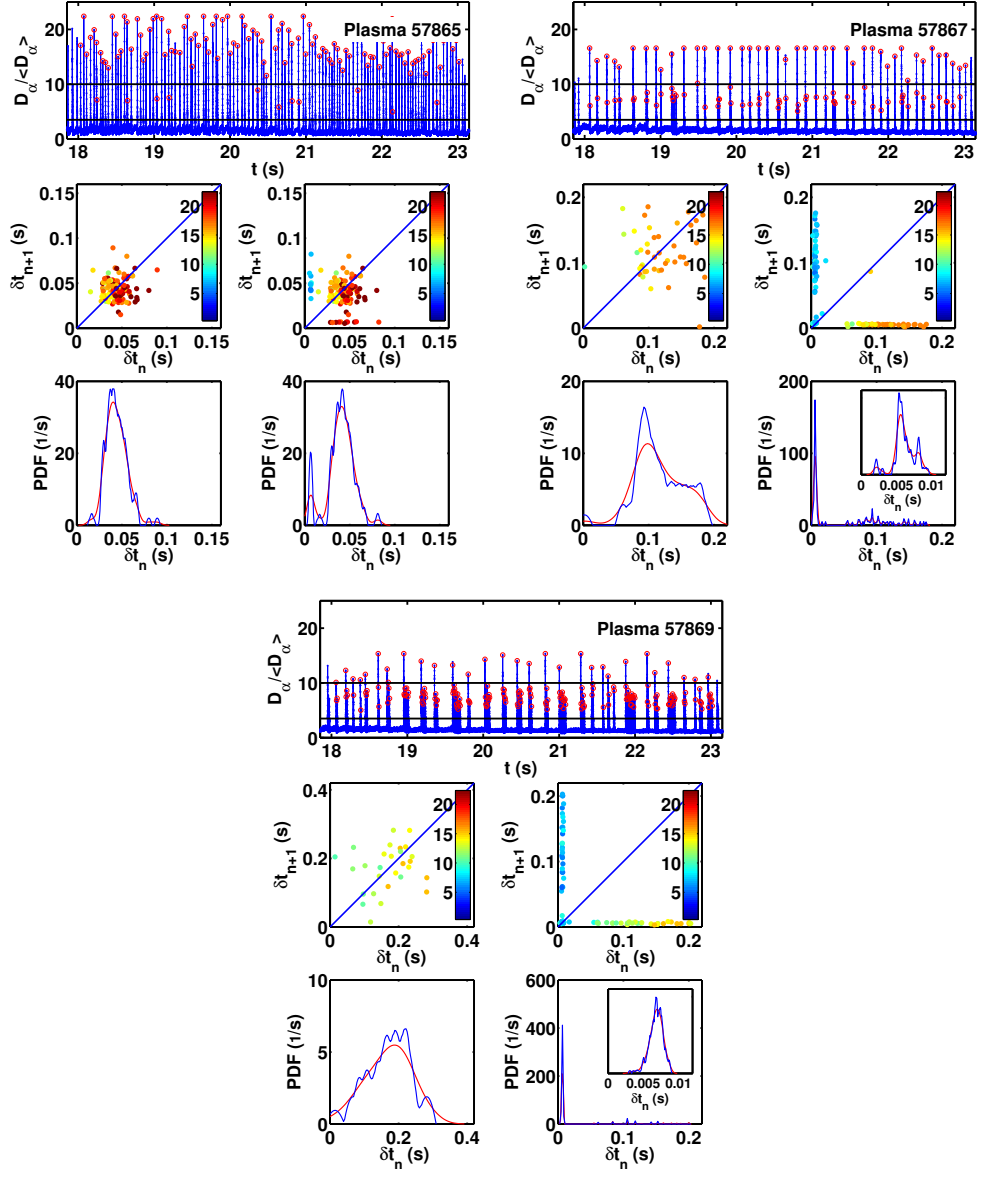


Figure 3.4: As Fig. 3.3, for three similar JET plasmas 57865, 57867, 57869 at higher gas puffing rates. The three plasmas are ordered, from the left, in terms of increasing magnitude of gas puffing, see Fig. 3.5. The bottom panels from JET plasmas 57867 and 57869 also include an inset panel displaying the sharp peak in the PDF. The population in this sharp peak increases with the gas puffing rate, and has the average period $\tau = 6.7 \pm 6.6 \times 10^{-2}$ (ms).

puffing rate is increased, which is different to that seen in Fig. 3.3. Each ELM with large D_α signal intensity is statistically likely to be rapidly followed by a population of postcursor ELMs with smaller D_α signal intensity. The likelihood of a postcursor ELM, and their number, increases with gas puffing rate. As a consequence, the delay plots constructed for different thresholds now, unlike Fig. 3.3, show different structure. At relatively low gas puffing rate (left hand plots) most delays fall within a single group on the $\delta t_{n+1} = \delta t_n$ line. However when the threshold is reduced, smaller postcursor events begin to feature in the time series of delays and result in populations (lines parallel to the axes) far from the $\delta t_{n+1} = \delta t_n$ line, and a new, narrowly constrained group on the $\delta t_{n+1} = \delta t_n$ line at small $(\delta t_{n+1}, \delta t_n)$. As the gas puffing rate is increased, these small postcursor events come to dominate numerically. It is noteworthy that whereas ELMs with large signal amplitude exhibit a broad inter-ELM time interval distribution, the distribution of the postcursors is very sharply defined and is invariant between the three JET plasmas, see Fig. 3.4 bottom panels. Its inverse defines a potentially important characteristic frequency of the ELMING process.

This process, as seen in the delay plots, is analogous to random large amplitude transient impulses driving a system that has a narrowband resonant frequency response. Furthermore, through a recent collaboration [Chapman et al., 2015] new information has expanded our understanding of the narrow band waiting times postcursors, which suggests the hypothesis of an external natural frequency aligning with possible sequence of *prompt* ELM [Chapman et al., 2014], identified as compound ELMs in Fig. 3.4. The complex nature of the postcursors have provided the argument to evaluate whether the build-up signature [Chapman et al., 2015] to an ELM that has been either globally displaced or suffered a bulk motion can be used to explain the compound ELM behaviour. In Chapman et al. [2014, 2015] the full flux loop voltage signals, VLD2 and VLD3, located in the vicinity of inner and outer divertor, have been both exploited to detect temporal phase synchronization during the intrinsic ELM build-up [Chapman et al., 2015], which suggests a coherent large-scale plasma perturbation. As further work, provided high resolution on relevant signatures exists, testing the hypothesis that compound ELMs, as in Fig. 3.4 plasma 57869, are a pattern of successive *prompt* ELMs and if they arise from

global plasma motion via self-kick [Chapman et al., 2015] or coupling with the vertical stabilization control coils in JET[Sartori et al., 2008; De la Luna et al., 2009].

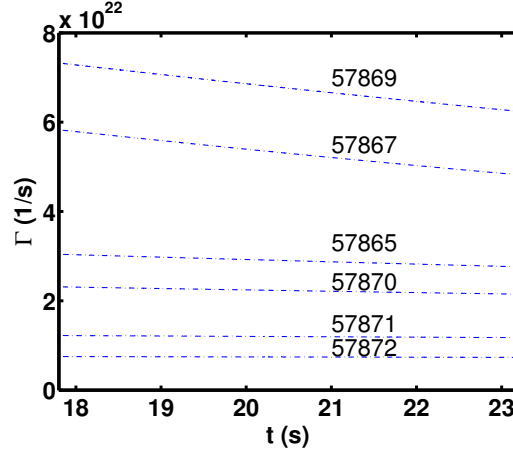


Figure 3.5: Time trace of gas puffing rate, Γ , in particles per second, which is the primary external control parameter for the six otherwise similar JET plasmas: ordered, from the bottom, in terms of increasing magnitude.

Figure 3.5 displays the gas puffing rates for all six JET plasmas. The clear changes in ELMing displayed in Fig. 3.3, and for JET plasmas 57867 to 57869, arise under comparatively small changes in gas puffing, while there is a relative large step (a factor of approximately two) between 57865 and 57867. Other ELM interval dynamics are in principle possible for other gas fuelling rates, especially for fuelling rates between those of 57865 and 57867, for these otherwise identical plasma operating regimes.

3.2.2 Conclusions

Some previous experiments have observed that Type I ELM frequency (mean inter-ELM interval) increases with gas puffing rate [McDonald et al., 2008]. Moreover, early theoretical studies [Lönneroth et al., 2003] suggested that it might be possible to explain the experimentally observed transition from Type I to Type III ELMy H-mode triggered by strong gas puffing, as well as the subsequent increase in ELM frequency and deterioration of plasma confinement,

as a transition from second to first stability (either ideal or resistive modes). However, there is still no widely accepted model for the overall ELMing process or processes.

Chapter 4

Modelling and evolution of Blob dynamics

4.1 Introduction

The edge of tokamak plasmas is a region dominated by transport of heat, momentum and energy. It is also subject of multiple-scale phenomena and instabilities[Wesson, 2004], see Section 1.5 Different propagating structures have been observed; blobs/filaments[Krashennnikov et al., 2008], ELMs [Wagner et al., 1982; Zohm, 1996] and their dynamics is far more complex as they tend to rotate[Rozhansky and Kirk, 2008; Kamiya et al., 2007] as well as undergoing radial transport, and down towards the divertor area. The transport mechanisms are believed to arise from saturation of nonlinear turbulent processes or from coherent MHD instabilities thresholds[D’Ippolito et al., 2011]. The layer where the exchange of energy, momentum and heat occurs extends from the separatrix to the far SOL. The mechanisms enhancing transport remain yet unclear, some theories exist that compare the measured quantities with the expected transport coefficients[Rozhansky and Kirk, 2008; Myra et al., 2012; Naulin, 2007]. It has been observed that blobs with sufficient radial velocity can reach far SOL areas, and even hit the walls which can be sometimes compared with ELM behaviour. Yet, they have distinctive formation mechanisms. While ELMs are formed by the nonlinear saturation of electromagnetic ballooning and/or peeling-ballooning modes near the pedestal[Kamiya et al.,

2007, see Fig. 8], blobs are formed by the nonlinear saturation of electrostatic edge turbulence near the separatrix [D’Ippolito et al., 2011; Krasheninnikov et al., 2008]. In the following sections we show novel results of 3D hybrid simulations using fusion plasmas parameters, with a seeded blob placed to evolve in a background plasma while convecting in a direction transverse to the magnetic field.

4.2 Hybrid model

In the hybrid simulations presented here, the particles follow a six-dimensional phase space evolution and the gridded fields, electric field \mathbf{E} and magnetic field \mathbf{B} are evolved in a staggered grid with three-dimensional Cartesian coordinates. The details of the plasma model and the equation system are explained in Sections 2.3.2 and 2.3.4. Periodic boundary conditions are applied to \mathbf{E} in boundary cells, and they are implied to \mathbf{B} , since it is obtained from the integration of \mathbf{E} , at each time step. Moments at opposite boundary points are added together, and particles crossing a boundary layer re-enter on the opposite side of the simulation domain.

4.2.1 Initial conditions: plasma parameters

The electromagnetic fields $\mathbf{E} = \mathbf{E}(\mathbf{x}, \mathbf{y}, \mathbf{z})$ and $\mathbf{B} = \mathbf{B}(\mathbf{x}, \mathbf{y}, \mathbf{z})$ are vector fields in the space extending in three dimensions to the limits of the simulation domain, see Table 4.1. All weighted macroparticles within a cell in the three-dimensional space (3D) are contributing to the density at the cell nodes evaluated in the B-grid. The Background plasma parameters are chosen to be characteristic of edge conditions in a medium size tokamak, e.g., NSTX or MAST. The background magnetic field $B_{z,0} = 0.69\text{T}$, temperature $T_e = 4 \times 10^6\text{K}$, approximately 344eV, and number density 8.1×10^{20} are the most important plasma parameter, small variations in these parameters are relevant in terms of the numerical evolution of the blob.

To describe the motion of the blobs or filaments we use the following coordinate system; x is defined as the parallel direction, given the hybrid’s code internal coordinate system. With the purpose of resembling the blob

Simulation domain	$300\Delta x, 150\Delta y, 100\Delta z$
Spatial resolution $\Delta x, \Delta y, \Delta z$	$0.1\rho_i$
Background magnetic field, \mathbf{B}_0	0.69T
Internal magnetic field, \mathbf{B}_{blob}	0.54T
Temperature, T_e	344 eV
Background ion gyroradius, ρ_i	~ 0.004 m
Background ion gyroperiod, t_{Ω_i}	9.5×10^{-8} s
Background number density, n_0	$8.1 \times 10^{20} \text{m}^{-3}$
Blob peak number density, n_{blob}	$2\text{-}3 \times n_0$
Alfvén speed, V_A	$0.53 \times 10^6 \text{ms}^{-1}$
Plasma beta, β_{blob}	0.0008
Plasma beta, $\beta_{background}$	0.002
Total computational particles	5.04×10^8

Table 4.1: Simulation parameters of a seeded blob in a background plasma with density n_0 .

convention direction (from left to right), we have chosen the y -direction as the radial direction, and the z -direction represents here the poloidal direction. Our frame of reference differs from that of previous 2D hybrid simulations [Gingell et al., 2012] in what they defined as a moving frame of reference, with the background plasma with velocity equal to the blob drift velocity \mathbf{V}_D . Hence, a standing observer in this new frame of reference see the blob moving with $-\mathbf{V}_D$. We do not apply this transformation in our simulations, but instead we have initialized the particles belonging to the filament with a drift velocity $\mathbf{V}_D = 0.3$ in units of Alfvén speed in the y -direction, according to normalization in Section 2.3.3.

4.2.2 Blob Initialization

We focus briefly in loading the particles in the computational domain. There is two apparent species, the particles in the background plasma with a specific density and distribution of velocities, and the particles inside the blob which are nonuniformly distributed in space, and their thermal velocity distribution has been shifted in the transversal coordinate by V_D , the nature of this drift velocity is explained in Section 1.7. Both groups of particles have equal charge and mass, as they are both protons, but we can treat them as two different

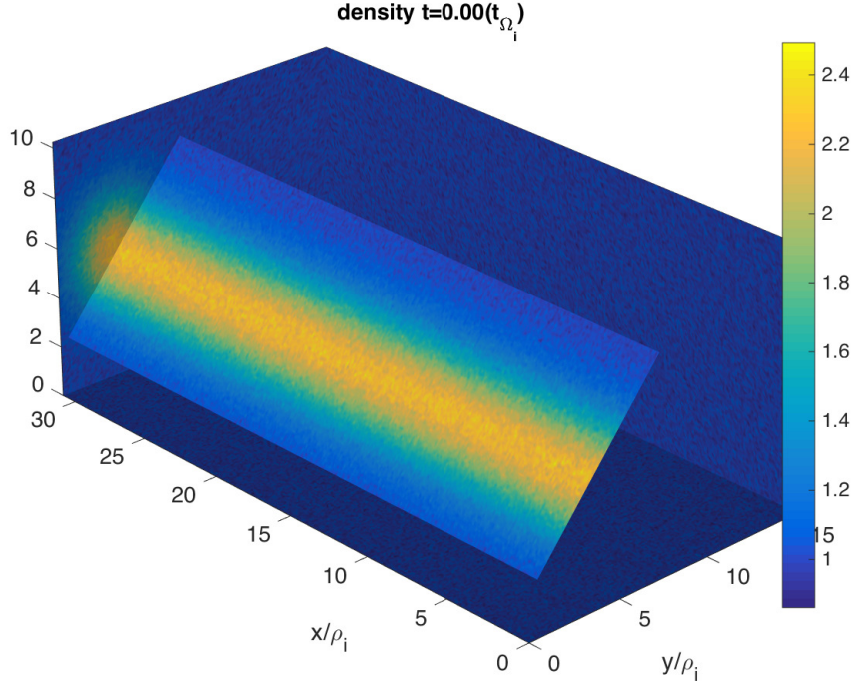


Figure 4.1: Oblique cut of a 3D plasma blob seeded in a background plasma with number density n_0 . Colorbar indicates number density in units of the background plasma n_0 . The blob is uniformly randomly distributed along its largest dimension and the cross-section density profile follows a Gaussian profile with blob radius set as the distribution's FWHM. The cross-section density profile was initialized with the same conditions as Eqs. (2.44) and (2.45), but in the spatial dimension to create the inhomogeneity.

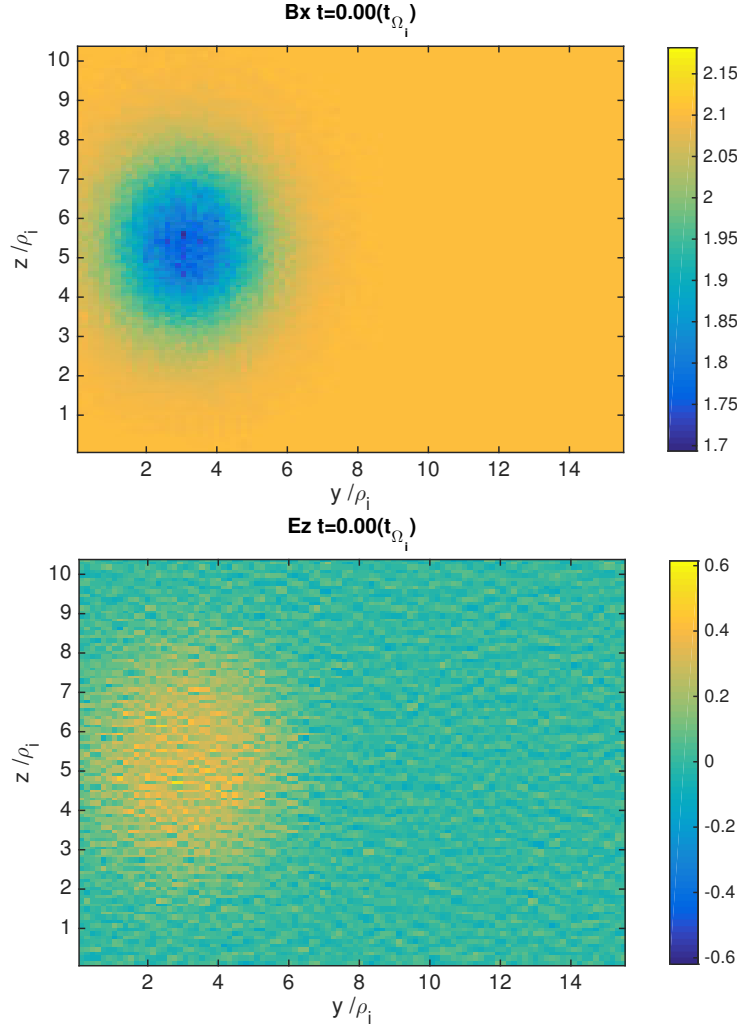


Figure 4.2: *Top*: transversal cut of the parallel magnetic field (x -direction) at $t = 0$. *Bottom*: transversal cut of the electric field in the poloidal direction (z -coordinate) at $t = 0$. This Electric field is in response to the imposed drift velocity \mathbf{V}_D , although is the charge polarization the responsible for the creation of this electric field, and in turn this field $\mathbf{E} \times \mathbf{B}$ the cause of the blob's drift.

species and calculate their grid-defined quantities as previously explained in Section 2.3.5; density, and current densities per species.

First, both groups are initialized in space, the background plasma has a uniform distribution in space with density n_0 everywhere, we simply apply Eq. (2.43). The second group, the particles inside the blob, are initialized in space nonuniformly with the following distribution[D’Ippolito et al., 2002],

$$n(y, z)_{blob} = n_{peak} e^{-((y-y_0)^2 + (z-z_0)^2)/2\delta_b^2} \quad (4.1)$$

where (y_0, z_0) is the pair coordinate where the blob’s centre is initialized inside the domain, and δ_b is the blob radius, in which case we are using the Gaussian distribution full-width at half maximum (FWHM) to quantify the blob radius consistently. Hence, the total density in space is $n_{blob} + n_0$. Fig. 4.1 shows the three dimensional blob density and background density through cuts in the domain edges, and a oblique cut at 45 degrees passing through the blob’s centre shows the density distribution along the magnetic field lines. Secondly, in both groups of particles, the velocity distributions are thermalized following initialization methods applied consistently in existing hybrid simulations [Gingell et al., 2012, 2013; Carbajal et al., 2014] through the inversion of their cumulative probability distribution[Birdsall and Langdon, 1975], see Section 2.3.7. The background plasma has a mean thermal speed $v_{th} = 0.067V_A$, and the blob’s mean thermal speed is $v_{th}^{blob} = 0.042V_A$ with the addition of shifting its velocity in the radial direction according to $v_y^{blob} \Leftarrow v_y^{blob} + V_D$.

The magnetic field is initialized uniformly, and then balanced using an MHD scale condition to balance the forces inside the blob. In a steady plasma with a scalar pressure the force balance for each species is

$$n_s q_s (\mathbf{E} + \mathbf{v}_s \times \mathbf{B}) = \nabla p_s \quad (4.2)$$

Adding over all species,

$$\mathbf{E} \sum_s n_s q_s + \sum_s n_s q_s \mathbf{v}_s \times \mathbf{B} = \nabla p \quad (4.3)$$

Since the plasma is quasi-neutral, the first term is negligible, and Eq. (4.3)

becomes,

$$\mathbf{J} \times \mathbf{B} = \nabla p \quad (4.4)$$

Using Ampere's Law, and the vector relation $(\nabla \times \mathbf{B}) \times \mathbf{B} = \mathbf{B} \nabla \mathbf{B} - \nabla B^2/2$ we obtain,

$$\nabla p = -\nabla \frac{B^2}{2\mu_0} + \frac{1}{\mu_0} \mathbf{B} \cdot \nabla \mathbf{B} \quad (4.5)$$

The last term is due to field line curvature, which we neglect at $t = 0$. Hence, we obtain a condition to balance the magnetic field pressure with the plasma pressure as follows,

$$p + \frac{B^2}{2\mu_0} = \text{constant} \quad (4.6)$$

The electric field is initialized using Eq. (2.16). Fig. 4.2 shows a transversal cut of the magnetic and electric field at $t = 0$ with the balance condition Eq. (4.6) for B_x and the induced E_z by seeding a drift velocity in the blob particles.

4.3 Results

We report kinetic simulations of filamentary structures where the central density peak is above the background density between $2 - 3 n_0$. The simulations were performed using the hybrid model of plasma explained in Section 2.3 with initial parameters matching those of tokamak middle size like MAST or NSTX, see Table 4.1. The simulations total time ranges between $10.35 - 17.5 t_{\Omega_i}$ gyroperiods.

Since, macroscopic fluid scales have been studied in detail with seeded blobs in Krasheninnikov et al. [2008]; D'Ippolito and Myra [2006]; Myra et al. [2006]; Bian et al. [2003] by using a model for blob spatial density distribution as in Eq. (1.74) with the addition of the background density n_0 . While they solved and evolved a coupled equation system composed by Eqs. (1.72) and (1.73), we focus on the evolution of a seeded ion-gyro scale blob, where single particles interaction with the background plasma shows a much richer blob evolution not observable at macroscopic scales as those in existing previous simulations.

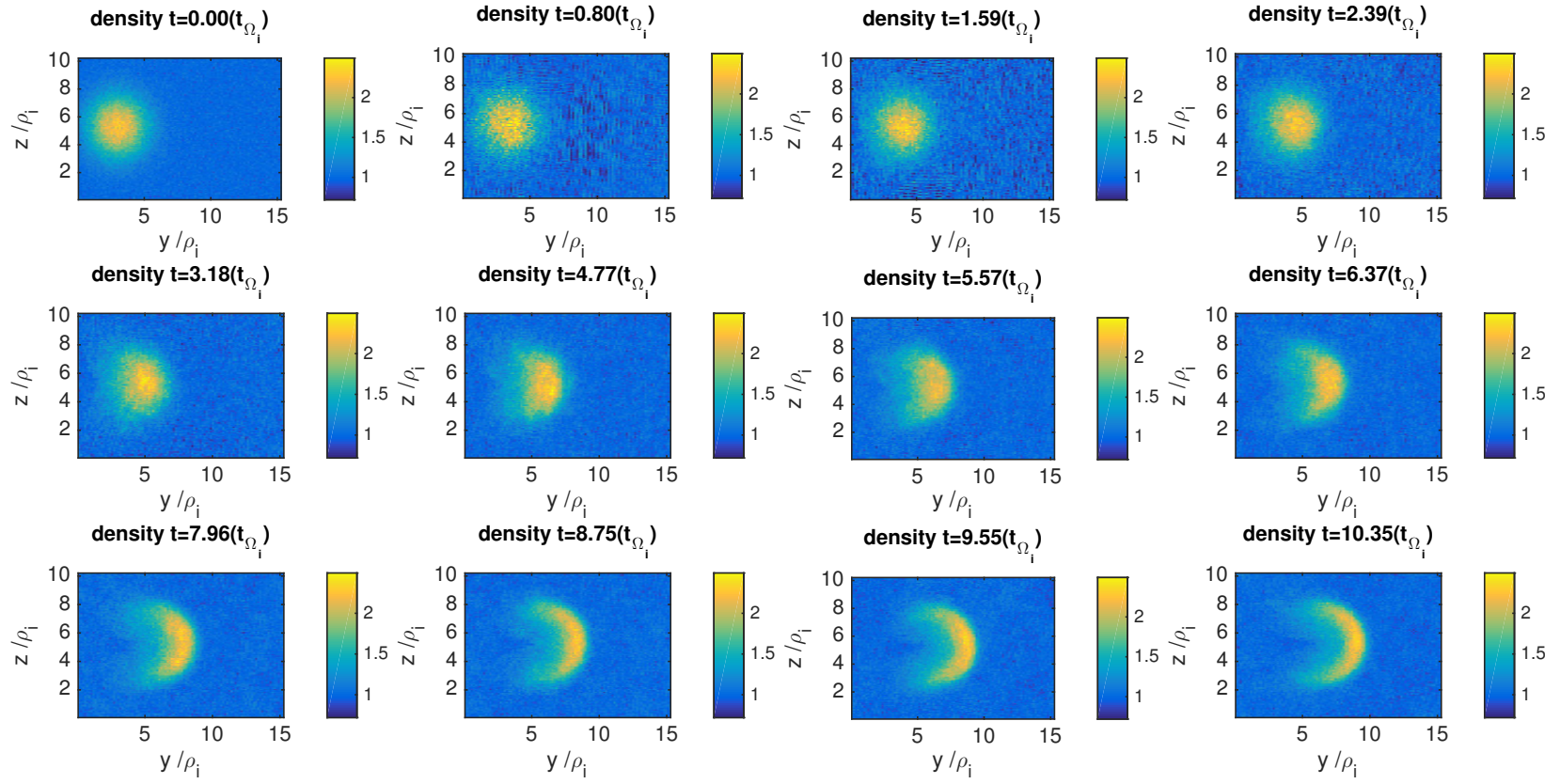


Figure 4.3: The evolution of the blob number density in a transverse cut at half the blob's parallel length. The blob radius is approximately $3.5\rho_i$.

4.3.1 Simulations of filaments in 3D

The full evolution of a three dimensional blob is shown in Fig. 4.3 through transversal cuts in the number density at half the blob parallel length. The initial response is relative to the force balance, right after $t = 0$, where any small variation in the initialization is compensated. The blob evolves from there under two competing processes. The travelling blob's flow with a density higher than the background and the drift convective velocity may drive Kelvin-Helmholtz instabilities. This may be observed as surfaces modes which grow amplitude variations restricted to the boundary and consequent nonlinear amplitude growth is expected at the flanks of the front. This effect was observed in 2D blob with a radius $\sim 10\rho_i$ in previous hybrid simulations [Gingell et al., 2012]. A related process is the nonlinear steepening of the blob density profile at the leading edge, which in cases where the structures remain coherent they resemble a shock-wave solution of the Burgers' equation [Treumann and Baumjohann, 1997].

We observe that as a result of convective velocity of the blob, the particles in the background of the blob are quickly released from the blob given their effective Larmor radius. Particles in the boundary may rapidly exchange momentum with the background plasma. In the front it is expected under fluid approximation that particles will be deflected to the sides creating bipolar structure under the assumption of an incompressible flow $\nabla \cdot \mathbf{v} = 0$. Yet, this is not an ideal case, and the effective Larmor radius plays a role in the particles transitioning in/out the blob boundary. Although the streamlines do partially present the bipolar twin cell vortex when we look at the plasma density currents in the perpendicular plane.

Because of the initial vorticity the plasma convects faster in the centre than in the extremes forming what appears as extended flanks which are very slowly separating from the plasma blob while continue to convect as they are displaced, resulting in a pile up effect on the upstream edge front, this front particularly conserve the density peak value for the most part of the evolution as opposed to 2D evolution in Gingell et al. [2012]. The main interaction between the two flows is observed at the front of the upstream edge where the two flows meet. There is first an observable steepening of the edge gradient facing the radial direction, which continue to enhance the sharp transition

layer for particles coming in/out the blob. This effect resembles that of a shock wave, described by Burgers' equation. The shock wave is typically found in space plasmas with a thin transitive area, propagating with supersonic speed in which there is a sharp increase of density, pressure, and speed. The one-dimensional approximation of the Burgers' equation,

$$\frac{\partial v}{\partial t} + v \frac{\partial v}{\partial x} = \alpha \frac{\partial^2 v}{\partial x^2} \quad (4.7)$$

where $\alpha > 0$ acting as a diffusion coefficient, and the convective derivative accounting for the nonlinearity on the lhs. The diffusive second order derivative (rhs) is compensating for the nonlinearity until the terms are comparable and the mode transition into a stationary solution. The evidence for dissipation balancing the wave front can be seen in the formation of normal electric field near the front on the blob which is not reproduced behind the blob, see Fig. 4.4 *top*.

We also observe in Fig. 4.4 *bottom* how the magnetic field strength in the parallel direction has been carried by the blob particles into the same shape determined by the particles distribution as the blob is drifting radially in the y -direction. If the particles can carry the magnetic field lines we think it is possible to bend the field lines for sections moving with the plasma blob at different speed in the parallel direction, which is the case for ELM filaments in which the footpoints do not follow the sheath-to-sheath model and therefore bending of the field lines requires an electromagnetic model for ELM filaments [Krasheninnikov et al., 2008].

In Fig. 4.6 we show the evolution of a three dimensional structure corresponding to the interpolated values of the number density at a given threshold, i.e., an iso-surface obtained from interpolation of density grid points in the vicinity of the chosen number density threshold $n_{Thre} = 1.2n_0$.

We have already discussed how the central section in the blob is moving faster than the flanks. This is mainly driven by current density inside the blob structure, also because there is nothing stopping the elongated shaping of the blob, as the transfer of momentum with background particles is broadening the front surface. The initial blob's width $\sim 3.5\rho_i$ has now been broadened to approximately $\sim 8\rho_i$. The convecting particles in the flanks of the blob,

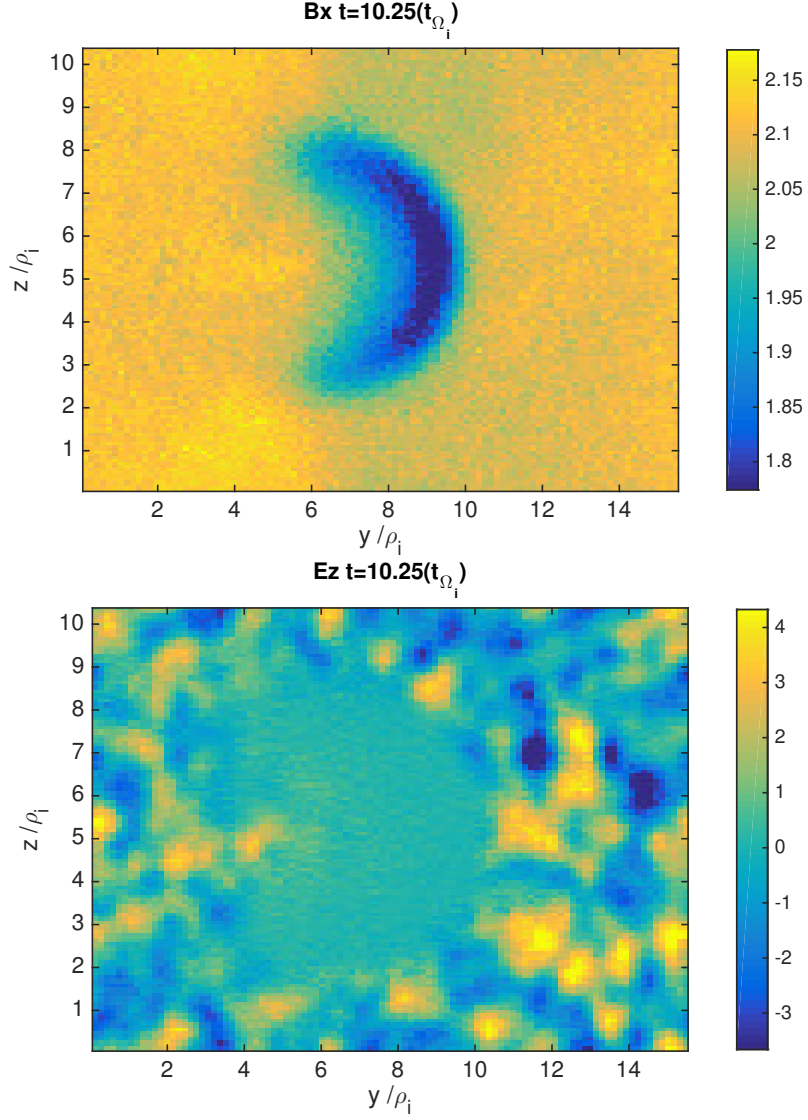


Figure 4.4: *Top*: transversal cut of the 3D blob's magnetic field showing the resultant magnetic rearrangement after the particles carried the magnetic field lines into the blob's shape. *Bottom*: same transversal cut showing the electric field in the z -direction where the distinct internal blob profile contrast with the edge front in which the creation on local electric field is in response to the dissipation processes which are in turn balancing the blob's convection. The same is not observed in the space behind the blob.

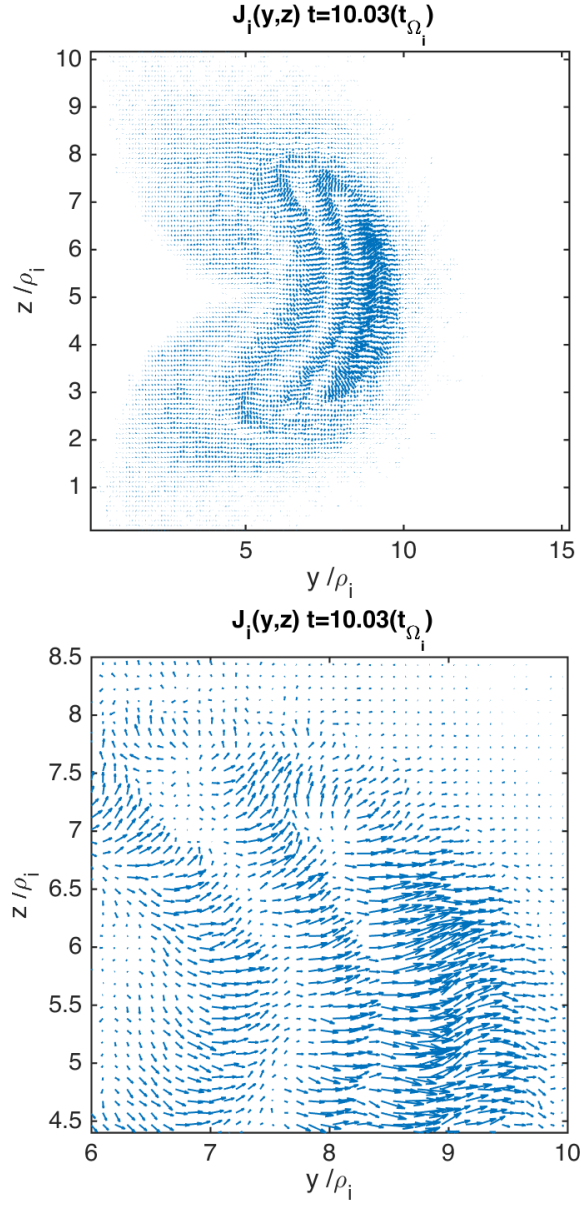


Figure 4.5: Current density in the transversal cut of a 3D blob. Background plasma current density is not plotted here.

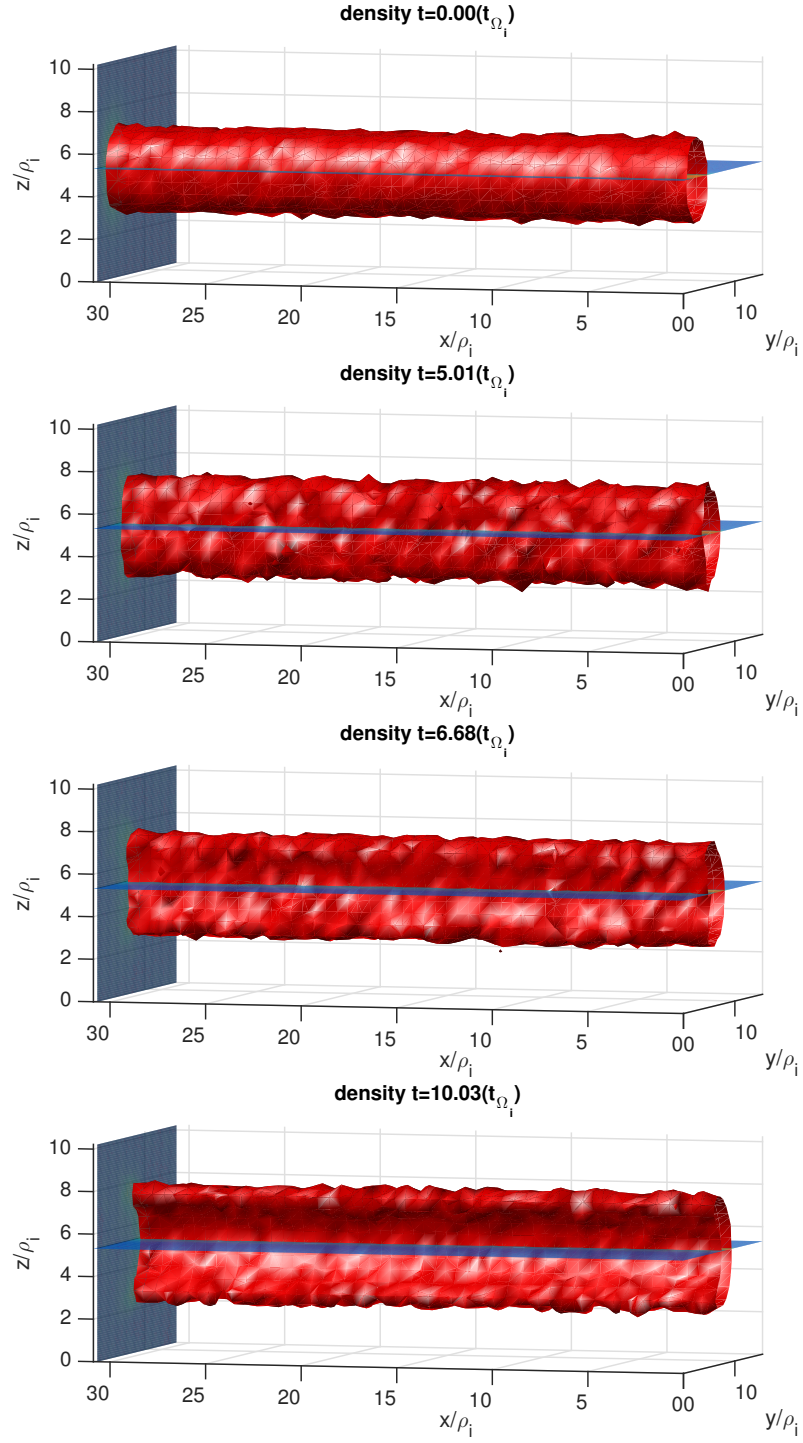


Figure 4.6: Time evolution of an iso-surface interpolated from selected grid number density values in the vicinity of the threshold density $n_{Thre} = 1.2n_0$.

those that are been delayed some distance behind, are still propagating with the coherent structure as observed in the centre and flanks density currents of Fig. 4.5. Only the particles initially in the blob (the background is not plotted here) are still moving radially outwards (y -axis), while others where completely removed and are now spreading freely behind the blob. Similarly, there are now particles from the background drifting with the blob in a structure similar to the one observed in Fig. 4.5, although they tend to complete the pattern observed, which is something yet to explain. Principally, the momentum exchange can be understood by the finite Larmor radius interaction between the two flows. The two flows have distinct velocities distributions, the blob velocity distribution is shifted in the y -direction by the drift velocity, which is imposed by an initial electric field (due to charge polarization) moving with the blob's flow. The ions moving across the front edge surface and the flanks experience the acceleration, caused by the electric field, which is in the opposite direction to the initial background flow so as to conserve momentum after the interaction. We can take the first moment of the Vlasov equation Eq. (1.54) for each ion population species s by multiplying it by \mathbf{v} and integrating over the velocity space. We arrive at the bulk momentum equation for ion species (s),

$$n_s m_s \frac{d\mathbf{v}_s}{dt} = q_s n_s (\mathbf{E} + \mathbf{v}_s \times \mathbf{B}) - \nabla p_s. \quad (4.8)$$

Taking the following Amperè's law, in the low-frequency limit, yields,

$$\nabla \times \mathbf{B} = \mu_0 \mathbf{J} = \mu_0 e \left(\sum_s n_s \mathbf{v}_s - n \mathbf{v}_e \right). \quad (4.9)$$

Then with the generalized Ohm's law and the Amperè's law Eq. (4.9) we can obtain, for each ion species s , the multi-fluid description as follows,

$$n_s m_s \frac{D\mathbf{v}_s}{Dt} = e n_s \left(\mathbf{v}_s - \frac{1}{n} \sum n_s \mathbf{v}_s \right) \times \mathbf{B} + \frac{n_s}{n} (\mathbf{J} \times \mathbf{B} - \nabla p_e) - \nabla p_s. \quad (4.10)$$

Where $D(\cdot)/Dt$ is the convective derivative and p_s is each ion species pressure. The first term on the rhs corresponds to the local momentum transfer between species, which is significant given the different species velocities in here. This

term describes the momentum transfer along the $\mathbf{v} \times \mathbf{B}$ direction. Finally, this term vanishes when we sum over all the species showing momentum conservation. The second term and third term were already described, as the Hall term which is responsible for the Whistler propagation and the pressure terms which account for the Alfvén compressional waves, explained in Section 1.4.7.

4.3.2 Simulation of blob dynamics in 2D

Existing 2D hybrid simulations [Gingell et al., 2012] shown the evolution of blobs with different radius sizes ranging between $1 - 10\rho_i$ in an effort to establish the evolution as one varies the initial blob size. The importance of the blob radius was already established in Section 1.7.2 where the blob coherence through convection is directly correlated with the blob size [Krasheninnikov et al., 2008; D’Ippolito and Myra, 2003; Myra et al., 2006]. Another focus in Gingell et al. [2012] was to establish the resolution limits for resolving the blob evolution with a minimum number of particles per cell without compromising most of the observed evolution character. We compare the total number of particles 2×10^7 to the 1.24×10^8 required to achieve our simulation with a radius $\sim 15\rho_i$. For this we have used the minimum suggested of 100 particles per cell. The main assumptions we adopted to simulate the 2D blobs is that of negligible curvature and ∇B , this last one particularly given the challenge in creating acceptable boundary conditions in the kinetic model. We have initialize the 2D blob with same plasma parameters as in Table 4.1. In Fig. 4.7, we present the initial parallel magnetic field, and the transverse electric field, and the initial number density in normalized units.

During the different blob stability regimes, explained in Section 1.7.2, it was stated that the curvature and ∇B played principally three roles in the blob evolution: a) ‘primary’ instability develops into turbulence (which may lead to blob creation in areas near the separatrix [Aydemir, 2005]), b) the curvature drives the blob motion down the magnetic field gradient, and c) the curvature continues to drive ‘secondary’ instabilities on the propagation structure, when different conditions for stability applies accordingly to $\hat{\delta}$, as seen in Figs. 1.12 and 1.13. The blob in our simulation consist of larger blob compared to blob sizes explored in the previous 2D results in [Gingell et al., 2012].

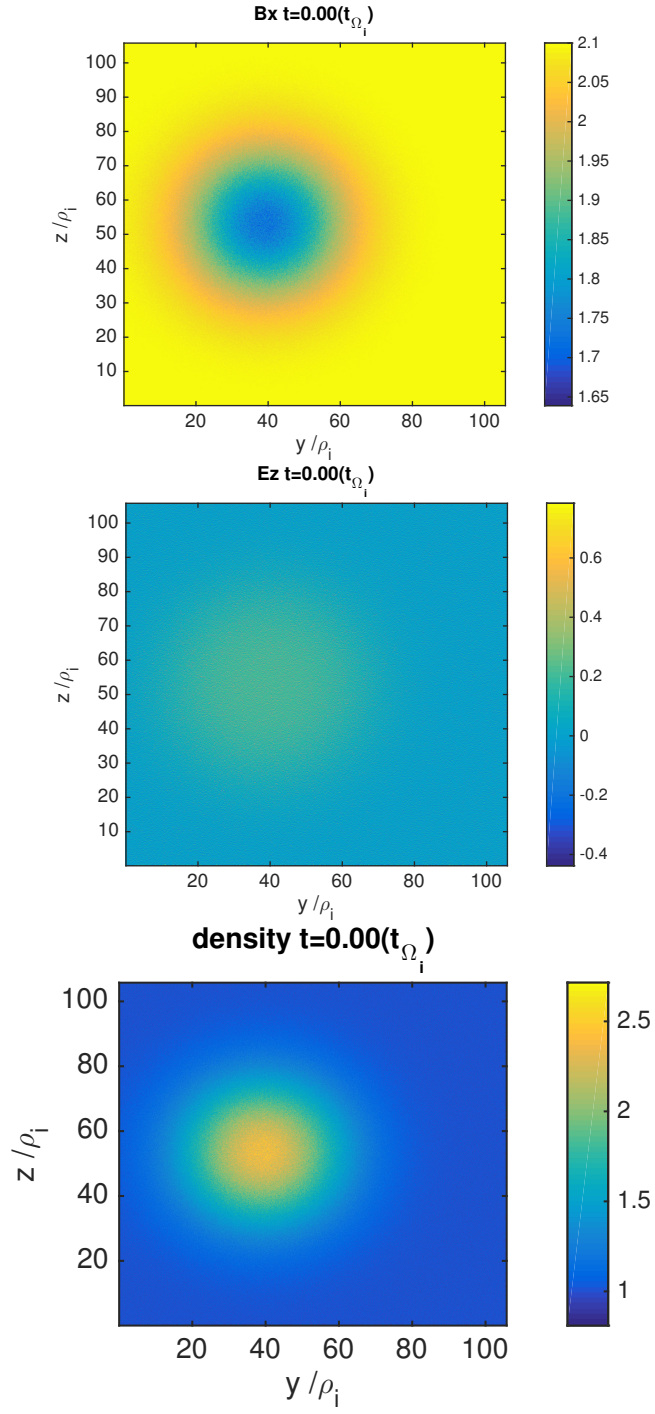


Figure 4.7: Initial conditions for a 2D blob of radius approximately $15\rho_i$.

In Fig. 4.8 we observe the evolution of the blob density currents for the large size $\sim 15\rho_i$ 2D blob, where the *top* panels show with arrows where the density current direction are in the plane at each grid point. Lets focus first on the small change suffered by the observable bulk velocities, as shown by the interpolation values in the *bottom* panels. Density currents inside the blob have only little variations, and the finite effect of the ion Larmor radius is responsible for this small variations in the internal current (centre of the blob) while the blob is seen to evolve across approximately 5 gyro-periods, yet this effect does little to perturb the convection velocity as most of the particles remain within the limit of the blob boundaries providing stability. We have already mentioned the effect of the particle diffusion caused by the effective Larmor radius affecting the particles at the bordering surface crossing the magnetic surface in and out. It is apparent that for this larger blob with size $\sim 2.4cm$ the evolution is more consistent with measured blobs of similar sizes. In NSTX the complete evolution of a $\sim 4cm$ blob measured using Gas puffing Injection technique with snapshots every $7.0\mu s$ shows the blob as a coherent structure, which is closer with the evolution we observe here in our 2D blob simulation at approximately $1.6\mu s$. In Fig. 4.9 the blob number density is show after 17.5 gyro-periods, where little change is observable.

Because we are not currently introducing any model for our blob evolution but simple evolving the coherent structure with particles, there is no consistent way for us to compare our blob size with the normalized blob size presented in the sheath-to-sheath model in Section 1.7.1. We can only make an estimation that the resulting evolution is an early stage of evolution presented in the sheath model, if we compare evolution time of a 2D blob fluid simulation carried by Yu and Krasheninnikov [2003], see Fig. 4.9. Finally, we find that for this particular blob size simulated here, the blob is less prompt to fall into any of the reviewed instability regimes including interchange instability and Kelvin-Helmholtz (KH) instability. For a blob of a smaller size ($\sim 10\rho_i$) in [Gingell et al., 2012, Fig. 11] we observed the asymmetric growth of a KH instability at an evolution time of 11 gyro-periods, which provides a point of reference. Yet, this evolution is not reproduced in the 2D blob here, and also for smaller size, which is the case of our 3D blob we do not observe the arising of the KH instability.

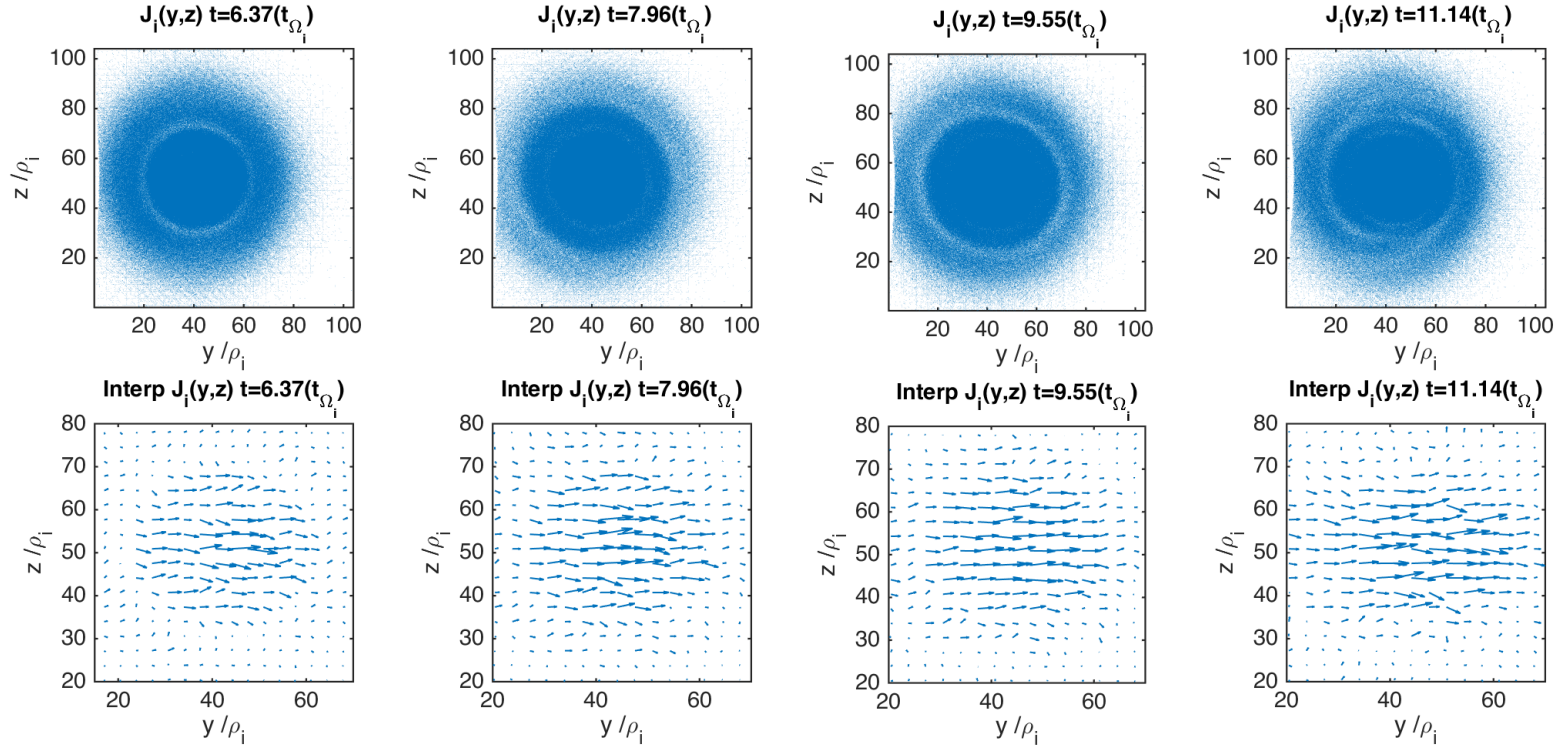


Figure 4.8: The intermediate time evolution of the transversal density current inside the large size 2D blob with radius $\delta_b = 15\rho_i$. The *bottom* panels are interpolations of the *top* panels arrows showing the direction of density currents per grid cell. These currents correspond only to moments for the blob particles.

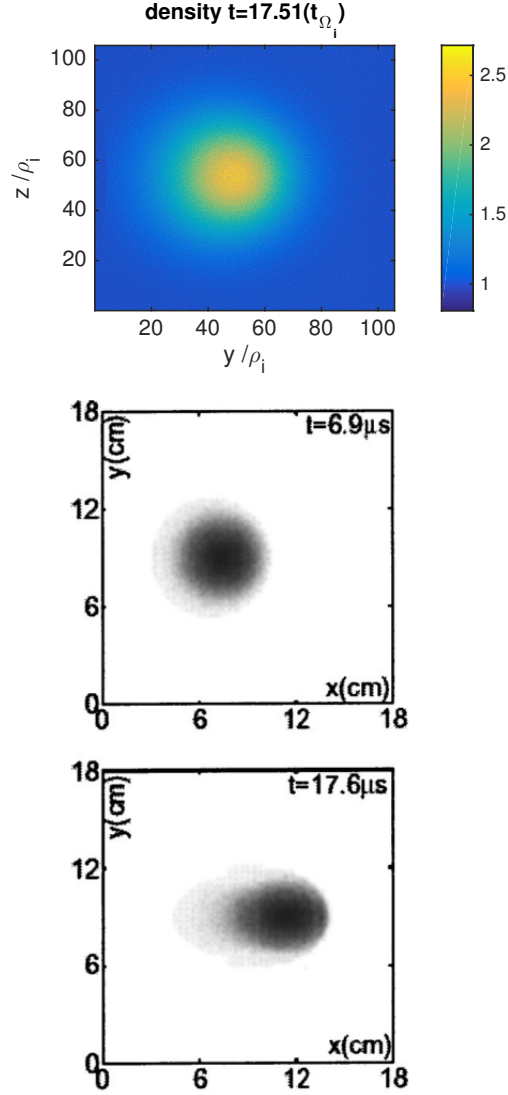


Figure 4.9: We compare the evolution of a large size 2D blob with an approximate width of 11.4cm at time $t = 17.5t_{\Omega_i} \approx 1.6\mu s$ with the evolution of a blob with radius $\hat{\delta}$ in a 2D fluid simulation. Reproduced from Yu and Krasheninnikov [2003].

4.4 Conclusions

We have investigated the evolution of seeded plasma blobs in a background plasma with peak densities ranging between $2 - 3n_0$. The evolution of plasmas

with hybrid simulation which involves a kinetic description of ions and fluid treatment for massless charge neutralizing electrons is extended to a few ion gyro-periods in plasma parameters matching those of an edge tokamak plasma. We have performed novel 3D kinetic simulations of ion gyro-scale filaments extending to a few centimetres on the parallel direction and of approximate cross section of 1.3cm in the perpendicular plane. We find that previous turbulent character for 2D blob size $\sim 4\rho_i$ developing into Kelvin-Helmholtz instability[Gingell et al., 2012] does not reproduce in the 3D case, but instead the mode survive stable for longer times entering a state which resemble that of a propagating shock wave[Aydemir, 2005]. We have provided the evolution of 3D number density through a series of iso-surfaces which corresponded to the grid-chosen values matching the vicinity of a threshold value $n_{Thre} = 1.2n_0$. In addition, simulations in three dimensions suffer a limiting character principally constrained by the computational resources, and the small time step in the case of hybrid codes in fusion plasmas, typically between $10^{-3} - 10^{-5}t_{\Omega_i}$.

We have also expanded previous 2D results which evolved maximum blob size up to $\sim 10\rho_i$ [Gingell et al., 2012]. Our modelled 2D blob has a radius $15\rho_i$ accordingly to our measured FWHM based in Eq. (4.1). We observe that the coherent character of the blob evolution resembles that of a similar size experimentally measured blobs[Maqueda et al., 2011], and that during the evolution time $17.5t_{\Omega_i}$ none of the existing instabilities has taken control of the blob dynamics. Furthermore, we have observed that the balance with local effects as we see in the front edge dissipation may play a role in allowing for travelling solitary front. Finally, we conclude that the nonlinear evolution of blob dynamics is highly dependent on the blob size, as determined by the normalized blob radius $\hat{\delta}$ as defined in Section 1.7.1, although we cannot currently offer an estimation of this value in our simulations.

Chapter 5

Conclusions

Increasing understanding of the underlying mechanisms responsible for instabilities observed in general plasmas and fusion experiments is crucial for the evolution of current experiments and for the general theory. Though many of these instabilities are observable they have extremely complex behaviour and exists typically in multiple lengths and times scales. Also, in fusion experiments there is a wide range of variations among tokamak toroidal geometries and divertor system, which is found to also play a role to some unknown degree in evolution of edge instabilities. We have performed two different but complementary studies: the characterization of edge localized modes taking advantage on its characteristic emission and their relative dependence on the variations of key control drivers, such as that of gas puffing rate. In addition, we studied the numerical evolution of typical filamentary structures found in edge of tokamak plasmas, and other linear devices. Their evolution is characterized by enhancement of transport of particle and energy to areas limiting with the walls and exhaust system. Both instabilities are characterized by their nonlinear evolution, and they are currently under intensive research, principally due to the fusion schedule and the construction of ITER.

5.1 Conclusions of ELMs analysis

We have established already the strong dependence of these instabilities with many control parameters. In our work here we have found they are strongly influenced by the changes on a single control parameter, in conditions where

the system remained mostly constant through the variations in the gas puffing rate. Also, some previous experiments have observed that Type I ELM frequency (mean inter-ELM interval) increases with gas puffing rate [McDonald et al., 2008]. Moreover, early theoretical studies [Lönnroth et al., 2003] suggested that it might be possible to explain the experimentally observed transition from Type I to Type III ELMy H-mode triggered by strong gas puffing, as well as the subsequent increase in ELM frequency and deterioration of plasma confinement, as a transition from second to first stability (either ideal or resistive modes). However, there is still no widely accepted model for the overall ELMing process or processes. Furthermore, through recent collaboration [Chapman et al., 2015] new information has expanded our understanding of the narrow band waiting times precursors, which suggests the hypothesis of an external natural frequency aligning with possible sequence of *prompt* ELM [Chapman et al., 2014], identified as compound ELMs. The complex nature of the precursors have provided the argument to evaluate whether the build-up signature [Chapman et al., 2015] to an ELM that has been either globally displaced or suffered a bulk motion can be used to explain the compound ELM behaviour. In Chapman et al. [2014, 2015] the full flux loop voltage signals, VLD2 and VLD3, located in the vicinity of inner and outer divertor, have been both exploited to detect temporal phase synchronization during the intrinsic ELM build-up [Chapman et al., 2015], which suggests a coherent large-scale plasma perturbation.

5.2 Conclusions of blob simulations

Modelling of blob dynamics present challenges relative to the nonuniform spatial distribution of particles, which creates diamagnetic drifts in a plasma with background magnetic field. Also, the current blob models do describe the physics of blobs completely and there is need for more detailed models. Early evidence from numerical simulations suggests that blobs and ELM filaments are created by the non-linear saturation of turbulence or an MHD instabilities in the edge plasma. In tokamaks the theory predicts that the dominant instability in the SOL is usually a curvature-driven sheath-interchange [Garbet et al., 1991] or resistive X-point [Myra et al., 2000*b,a*; Xu et al., 2000] mode loc-

alized on the low field side. They are both not easily comparable with kinetic simulations, as those showed here, yet we have found evidence for the consistent evolution of coherent structures with radial velocities comparable with those measured in experiments. Particularly, to the 2D and 3D simulations we find that previous turbulent character for 2D blob size $\sim 4\rho_i$ developing into Kelvin-Helmholtz instability[Gingell et al., 2012] does not reproduce in the 3D case, but instead the mode survive stable for longer times entering a state which resemble that of a propagating shock wave[Aydemir, 2005]. We have provided the evolution of 3D number density through a series of iso-surfaces which corresponded to the grid-chosen values matching the vicinity of a threshold value $n_{Thre} = 1.2n_0$. In addition, simulations in three dimensions suffer a limiting character principally constrained by the computational resources, and the small time step in the case of hybrid codes in fusion plasmas, typically between $10^{-3} - 10^{-5}t_{\Omega_i}$.

We have also expanded previous 2D results which evolved maximum blob size up to $\sim 10\rho_i$ [Gingell et al., 2012]. Our modelled 2D blob has a radius $15\rho_i$ accordingly to our measured FWHM based in Eq. (4.1). We observe that the coherent character of the blob evolution resembles that of a similar size experimentally measured blobs[Maqueda et al., 2011], and that during the evolution time $17.5t_{\Omega_i}$ none of the existing instabilities has taken control of the blob dynamics. Furthermore, we have observed that the balance with local effects as we see in the front edge dissipation may play a role in allowing for travelling solitary front. Finally, we conclude that the nonlinear evolution of blob dynamics is highly dependent on the blob size, as determined by the normalized blob radius $\hat{\delta}$ as defined in Section 1.7.1, although we cannot currently offer an estimation of this value in our simulations.

Appendix A

The next step for fusion: ITER

Fusion experiments started around the second half of the twentieth century, and thanks to the active development we have now a much better understanding of the required experimental conditions and scaling laws that regulate to some degree how fusion can be sustained in new plasmas scenarios and varied experimental conditions[Gormezano et al., 2008].

In 2006, the ITER agreement was signed by the ITER parties (European Atomic Energy Community, China, India, Japan, Republic of Korea, Russia, and United States of America) for the collaborative effort to achieve fusion by the year 2050. Fusion development adopted a more structured plan as well, the fusion road map [Romanelli, 2012]. Here, the most critical steps and milestones were stated; first, to achieve fusion within the ‘Horizon 2020’ period mainly by focusing all efforts in the ITER experiment. Nonetheless, the best fusion scenario remains limited by our own understanding of the many fusion mechanisms and phenomena, and also by the control and fine tuning of experiments. Real plasmas at high temperatures and densities are susceptible to slight changes, perturbations can give grow to instabilities and subsequent brake in confinement. Understanding the fusion mechanisms has been positively influenced by the intertwined development of theory, experiment, and numerical simulations. However, other critical considerations, such as safety, energy gain, and costs have set the precedent for past and future constraints in fusion development. More about the history of the ITER project in ITER¹ digital space. With ITER we observe that fusion activity and development are

¹www.iter.org

no longer a local activity but rather that of a global and extended scientific community.

Many past fusion devices are no longer in use, but they served their purpose by helping to modernize the designs and better understanding the physical principles. Some of the most streamline machines that still remain and evolved are for instance: linear devices, tokamaks and stellarators (see the book by Freidberg [2007] on magnetic confinement). A variation from the traditional magnetically confined plasma is the inertial confinement technology for fusion energy, although is beyond the scope here, it is a very interesting approach using high end lasers towards the same end. In general, all the above machines are based on magnetic confinement, they use superconductors carrying high currents to generate intense magnetic fields. These magnetic fields or coils are used to exert strong confining forces over a group of ionized gas particles contained inside a vacuum vessel. A model of the ITER tokamak can be seen in Fig. A.1. The fields are the basis of the confinement, but this does not guaranteed fusion reactions, we also need the right temperature and densities or we can say the right pressure. Although, these machines are all designed to achieve magnetically confined thermonuclear reactions they provide only some degree of their combined contributions, and yet it is very difficult to extrapolate the physics from one machine to another, even among the several different tokamak experiments. It should be notice that the tokamak is the chosen candidate for the construction of ITER.

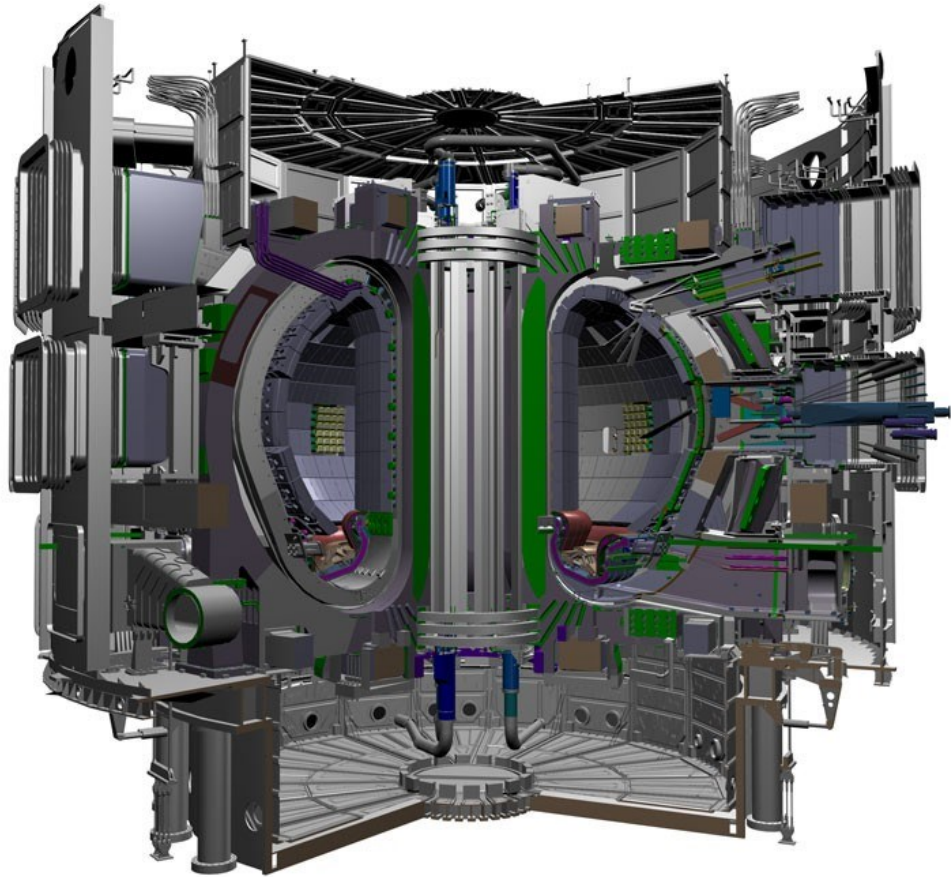


Figure A.1: Schematic of the ITER project based on the tokamak concept of magnetic confinement, in which the plasma is contained in a torus-shaped vacuum vessel. The fuel is a mixture of deuterium and tritium, and is heated to temperatures over 150 million degree centigrade. Strong magnetic fields are used to keep the plasma away from the walls; these are produced by superconducting coils and by an electrical current driven through the plasma. Reproduced from www.iter.org/mach.

List of Figures

1.1	Velocity averaged cross section ($\langle\sigma v\rangle = R_{ij}/n_i n_j$) for the D-T, D-D, and D-He ³ fusion reactions as a function of temperature, reproduced from Wesson [2004].	5
1.2	Cycloidal trajectories of ions and electrons in crossed magnetic and electric fields. The electric field \mathbf{E} acting together with the magnetic field \mathbf{B} gives rise to a drift velocity in the direction given by $\mathbf{E} \times \mathbf{B}$, reproduced from [Bittencourt, 2004].	11
1.3	<i>Top panel</i> , torsional Alfvén wave with \mathbf{k} parallel to \mathbf{B}_0 . <i>Middle panel</i> , the magnetoacoustic wave has velocity oscillations in the plane containing \mathbf{B}_0 and \mathbf{k} . <i>Bottom panel</i> , the fast compressional magnetoacoustic with $\mathbf{k} \perp \mathbf{B}_0$. The oscillation involve compression of both the fluid and the magnetic field.	17
1.4	Dispersion relation for a uniform magnetized magneto-spheric plasma[Pritchett, 2000] simulated using a 3D hybrid code, algorithm description is in Section 2.3. The theoretical dispersion relations Eqs. (1.67) and (1.68) for whistler wave and ion cyclotron resonant mode are draw in blue line, alfvén speed black line, top plot. The perpendicular direction, bottom plot, shows the compressional magnetoacoustic mode from Eq. (1.64).	19
1.5	A tokamak poloidal cross-section showing the core of plasma at the centre, followed by the separatrix (the boundary between closed and open field lines), scrape-off layer (SOL) and finally the walls. In this configuration, a divertor is positioned at the bottom of the machine where the X-point lines reach the inner/outer divertor target.	21

1.6	Schematic diagram of a tokamak. The plasma is contained inside a torus-shaped vacuum vessel. Poloidal B_p and toroidal B_ϕ magnetic fields keep the particles within the boundaries of the plasma in connected orbits and away from the walls. Particles gyrating (their guiding centre, as they gyrate around a field line) are also following the helical field lines formed by the combined toroidal and poloidal magnetic field lines.	23
1.7	Two main areas of the mayor radius can be seen in panel (a), the section of the core where L-mode and H-mode pressure profile decreased in a similar way, and the dramatic difference in the pedestal zone where a steep pressure gradient is observed forming during the H-mode. Noticeably, the arising of one instability is depicted here, the ELM crash, to account for the sudden lost of pedestal pressure threshold and the return to a similar L-mode state, with the main difference that the pedestal is then quickly recovered. (b) We observe here the poloidal cross-section of the plasma and the magnetic surfaces with the X-point at the bottom typical of the H-mode plasma. The ELM time period is depicted at the edge showing two different times for perpendicular and parallel displacement. Reproduced from [Kamiya et al., 2007].	25
1.8	Typical sequence of ELMs during a power rise in DIII-D: at $P \sim P_{thr}$ type III ELMs are found; at higher P , type I ELMs occur.	26

1.9	Plot of edge electron temperature versus density for a series of vertical target ELMy H-modes with varying rates of gas fuelling. The temperature and density values at the pressure gradient limit (diamonds) are representative of values at the top of the edge electron pedestal taken just prior to an ELM crash. The edge electron temperature and density at the L-H transition (circles) and at the end period of the transition ELMs (squares) are shown for comparison. At highest gas fuelling rates, the edge electron pressure begins to deviate from the curve of approximately constant pressure (the dashed arrow). In a few cases, transitions back to L-mode have been observed; here the curve for the H-mode threshold is schematic. Reproduced from [Horton et al., 1999].	28
1.10	Blob creation and propagation in NSTX as seen by the GPI diagnostic. The frame rate is $7.5\mu\text{s}/\text{frame}$ and the camera extension is $25 \times 25\text{cm}$ near the outer midplane separatrix (solid line). The radial convection towards the limiter (dashed lines) has an approximate velocity of $\sim 1\text{km/s}$. Reproduced from Maqueda et al. [2011].	31
1.11	A representation of a blob (2D) or filament (3D) on the outer midplane of the tokamak's edge plasma. This structure is localized in the plane perpendicular to magnetic field, but it is extended in the parallel direction, along \mathbf{B} . The blobs are believed to originate of either turbulence or macroscopic MHD instabilities. Figure is reproduced from D'Ippolito et al. [2011].	32
1.12	Contour plot of the evolution of a 2D density blob with small δ_b . During the radial motion of the blob the density concentrates at half of its periphery creating a front. The blob is unstable to the Kelvin-Helmholtz mode and evolves to a mushroom shape object. Reproduced from Bian et al. [2003].	35

1.13	blob density profile with large δ_b in a 2D simulation. During the radial motion of the blob, it becomes unstable to the curvature-driven interchange mode. Here the non-linear phase is characterize by the presence of elongations or fingers as seen across the poloidal direction in slab geometry. Reproduced from D'Ippolito and Myra [2003].	36
2.1	On the top left, the Probability distribution of the variable star Cep X-4 is showed, with bins of 10^3 points. On the top right, The QQplot test, see Section 2.1.1, is showing evidence that Cep X-4 does not possess a Gaussian distribution. Bottom plot, we have fit Cep X-4 distribution with two different model distributions, in blue a Gaussian distribution, and in red a t-student distribution which shows a better fit of the signal distribution.	40
2.2	Running mean, variance, and standard deviation. The linear fit, red line, has the following slope values: from the bottom, variance $m = 0.064$, mean $m = -0.0013$, the standard deviation $m = 0.018$. We find then semi-stationary time windows where linear methods can be applied in between bursts.	41
2.3	D_α line for JET plasma 57865. ELMs are steep and narrow in time. In this particular case the time width is 5.5ms. A linear fit of the point used for selection shows a slope $m = 8.13 \times 10^4$.	43
2.4	The ELM time series for shots 57865(left), 57867(centre), and 57869(right). The top panels show the full time series for $t = 15 - 25$ s. The bottom panels highlights $t = 18.3 - 18.8$ s in order to show clearly which features of the time series are being detected as type-I ELMs.	44
2.5	Delay plots for shots 57865(left), 57867(centre), 57869(right). The top panels show delay plots of δt_{n+1} against δt_n colour-coded by their ELM amplitude. The clustering of points near the horizontal and vertical axis means that in average the range of waiting time expected after a shorter waiting time is larger. The bottom panels are histograms of the waiting times values with a Gaussian fit.	45

2.6	ELMing in JET-57865 and JET-57870, respectively, with red round marked ELMs. <i>Left:</i> ELMs inside vertical lines exemplify a compound-ELM. <i>Right:</i> a misidentified double-peak selection.	46
2.7	Basic steps in kinetic particle/hybrid simulations, reproduced from [Winske and Omidi, 1996].	48
2.8	The two-dimensional CIC or area-weighting scheme. The fraction of charge assigned to the four neighbouring mesh points from a particle at position x is given by the area of overlap of its cloud shape with the cells containing those neighbouring mesh points.	55
2.9	Schematic of the time advance scheme in CAM-CL. At the beginning of the step, \mathbf{x} has been advanced to time level 1/2 with \mathbf{v}_0 . Moments already collected are $\varrho_c^{1/2}$ and the ‘free-streaming’ ionic current density $\mathbf{J}_i^*(\mathbf{x}^{1/2}, \mathbf{v}_0)$, as well as ϱ_c^0 and \mathbf{J}_i^0 . Two solutions of \mathbf{B} are advanced by substeps (cyclic leapfrog) to time level 1/2, with $\mathbf{E}(\varrho_c^0, \mathbf{J}_i^0, \mathbf{B}, T_e)$. The current advance method advances \mathbf{J}^* to $\mathbf{J}_i^{1/2}$, with the fields $\mathbf{B}^{1/2}$ and $\mathbf{E}(\varrho_c^{1/2}, \mathbf{J}_i^0, \mathbf{B}^{1/2}, T_e)$. The time centred (for \mathbf{v}) electric field is now evaluated at time level 1/2, $\mathbf{E}^{1/2}(\varrho_c^{1/2}, \mathbf{J}_i^{1/2}, \mathbf{B}^{1/2}, T_e)$. The particles are pushed, $\mathbf{v}_0 \rightarrow \mathbf{v}_1$, $\mathbf{x}^{1/2} \rightarrow \mathbf{x}^{3/2}$, and the moments are collected, $\varrho(\mathbf{x}^{3/2})$, from which ϱ_c^1 is obtained as an average of $\varrho_c^{1/2}$ and $\varrho_c^{3/2}$; the backward and forward ‘free-streaming’ currents $\mathbf{J}_i^{*-}(\mathbf{x}^{1/2}, \mathbf{v}^1)$ and $\mathbf{J}_i^{*+}(\mathbf{x}^{3/2}, \mathbf{v}^1)$, which are averaged to obtain \mathbf{J}_i^1 . Finally, $\mathbf{B}^{1/2} \rightarrow \mathbf{B}^1$ and the cycle repeats, reproduced from Matthews [1994].	59
2.10	Normalized thermal velocity distribution.	61

3.1	For six JET plasmas the counts of ELMs events as a function of the amplitude threshold (cut every 0.5 of normalized amplitudes). We observe the vertical dashed line at 3.5 separating noise level. The second vertical line, with amplitude value 10.0, is chosen to illustrate best the changes in delay plots (middle panel) of Figs. 3.3 and 3.4 according to the variations of the gas puffing rate in Fig. 3.5.	67
3.2	Diagram of the JET vessel in poloidal cross section showing divertor (bottom) and walls (grey structure). The line of sight of D_α radiation emission at 656[nm] in vertical lines is pointing to the inner and outer divertor spanning across multiple channels, as shown by the broadening of line limits. At the top, magnetic flux surfaces from EFIT equilibrium reconstruction of JET plasmas 57872 and 57869 at $t \approx 22$ s.	69
3.3	ELM characteristics of three similar JET plasmas 57872, 57871, 57870 at lower gas puffing rates, showing for each plasma: (top of each panel) the time trace of D_α signal intensity, displaying also the two amplitude thresholds used for the centre and bottom plots; (centre of each panel) delay plots for ELMs, with amplitude colour coded above the higher (lower) threshold on the left (right); (bottom of each panel) corresponding probability density functions for the distributions of measured δt_n for the ELM time series, using the same amplitude thresholds as for the delay plots; the red and blue curves represent different binning of the same data. The three plasmas are ordered, from the left, in terms of increasing magnitude of gas puffing, see Fig. 3.	71

3.4	As Fig. 3.3, for three similar JET plasmas 57865, 57867, 57869 at higher gas puffing rates. The three plasmas are ordered, from the left, in terms of increasing magnitude of gas puffing, see Fig. 3.5. The bottom panels from JET plasmas 57867 and 57869 also include an inset panel displaying the sharp peak in the PDF. The population in this sharp peak increases with the gas puffing rate, and has the average period $\tau = 6.7 \pm 6.6 \times 10^{-2}$ (ms).	72
3.5	Time trace of gas puffing rate, Γ , in particles per second, which is the primary external control parameter for the six otherwise similar JET plasmas: ordered, from the bottom, in terms of increasing magnitude.	74
4.1	Oblique cut of a 3D plasma blob seeded in a background plasma with number density n_0 . Colorbar indicates number density in units of the background plasma n_0 . The blob is uniformly randomly distributed along its largest dimension and the cross-section density profile follows a Gaussian profile with blob radius set as the distribution's FWHM. The cross-section density profile was initialized with the same conditions as Eqs. (2.44) and (2.45), but in the spatial dimension to create the inhomogeneity.	79
4.2	<i>Top</i> : transversal cut of the parallel magnetic field (x -direction) at $t = 0$. <i>Bottom</i> : transversal cut of the electric field in the poloidal direction (z -coordinate) at $t = 0$. This Electric field is in response to the imposed drift velocity \mathbf{V}_D , although is the charge polarization the responsible for the creation of this electric field, and in turn this field $\mathbf{E} \times \mathbf{B}$ the cause of the blob's drift.	80
4.3	The evolution of the blob number density in a transverse cut at half the blob's parallel length. The blob radius is approximately $3.5\rho_i$.	83

4.4	<i>Top</i> : transversal cut of the 3D blob's magnetic field showing the resultant magnetic rearrangement after the particles carried the magnetic field lines into the blob's shape. <i>Bottom</i> : same transversal cut showing the electric field in the z -direction where the distinct internal blob profile contrast with the edge front in which the creation on local electric field is in response to the dissipation processes which are in turn balancing the blob's convection. The same is not observed in the space behind the blob.	86
4.5	Current density in the transversal cut of a 3D blob. Background plasma current density is not plotted here.	87
4.6	Time evolution of an iso-surface interpolated from selected grid number density values in the vicinity of the threshold density $n_{Thre} = 1.2n_0$	88
4.7	Initial conditions for a 2D blob of radius approximately $15\rho_i$	91
4.8	The intermediate time evolution of the transversal density current inside the large size 2D blob with radius $\delta_b = 15\rho_i$. The <i>bottom</i> panels are interpolations of the <i>top</i> panels arrows showing the direction of density currents per grid cell. These currents correspond only to moments for the blob particles.	93
4.9	We compare the evolution of a large size 2D blob with an approximate width of 11.4cm at time $t = 17.5t_{\Omega_i} \approx 1.6\mu s$ with the evolution of a blob with radius $\hat{\delta}$ in a 2D fluid simulation. Reproduced from Yu and Krasheninnikov [2003].	94
A.1	Schematic of the ITER project based on the tokamak concept of magnetic confinement, in which the plasma is contained in a torus-shaped vacuum vessel. The fuel is a mixture of deuterium and tritium, and is heated to temperatures over 150 million degree centigrade. Strong magnetic fields are used to keep the plasma away from the walls; these are produced by superconducting coils and by an electrical current driven through the plasma. Reproduced from www.iter.org/mach	101

Bibliography

- Adamov, G. M. [2008], ELM synchronized Thomson scattering measurements on ASDEX Upgrade, *in* ‘35th EPS Conference on Plasma Phys. Hersonissos’, Vol. 32, pp. P-4.002.
- Ahlers, G. [1974], ‘Low-Temperature Studies of the Rayleigh-Bénard Instability and Turbulence’, *Physical Review Letters* **33**(20), 1185–1188.
- Aydemir, A. Y. [2005], ‘Convective transport in the scrape-off layer of tokamaks’, *Physics of Plasmas* **12**(6), 062503.
- Bak, P. E., Yoshino, R., Asakura, N. et al. [1999], ‘Identification of Unstable Periodic Orbit in Inter-Edge-Localized-Mode Intervals in JT-60U’, *Physical Review Letters* **83**(7), 1339–1342.
- Baker, D., Snider, R. and Nagami, M. [1982], ‘Observation of cold, high-density plasma near the Doublet III limiter’, *Nuclear Fusion* **22**(6), 807–811.
- Baumjohann, W. and Treumann, R. A. [1997], *Basic Space Plasma Physics*, World Scientific.
- Beurskens, M. N. A., Osborne, T. H., Horton, L. D. et al. [2009], ‘Pedestal width and ELM size identity studies in JET and DIII-D; implications for ITER’, *Plasma Physics and Controlled Fusion* **51**(12), 124051.
- Bian, N., Benkadda, S., Paulsen, J.-V. et al. [2003], ‘Blobs and front propagation in the scrape-off layer of magnetic confinement devices’, *Physics of Plasmas* **10**(3), 671.
- Birdsall, C. K. and Langdon, A. B. [1975], *Plasma physics via computer simulation*, Institute of Physics.

- Bittencourt, J. A. [2004], *Fundamentals of Plasma Physics*, Springer New York.
- Bodenschatz, E., Pesch, W. and Ahlers, G. [2000], ‘Recent Developments in Rayleigh-Bénard Convection’, *Annual Review of Fluid Mechanics* **32**(1), 709–778.
- Boedo, J. A., Rudakov, D. L., Moyer, R. A. et al. [2003], ‘Transport by intermittency in the boundary of the DIII-D tokamak’, *Physics of Plasmas* **10**(5), 1670.
- Brochard, F., Gravier, E. and Bonhomme, G. [2006], ‘Transitions to spatiotemporal chaos and turbulence of flute instabilities in a low- β magnetized plasma’, *Physical Review E* **73**(3), 036403.
- Calderon, F. A., Dendy, R. O., Chapman, S. C. et al. [2013], ‘Identifying low-dimensional dynamics in type-I edge-localised-mode processes in JET plasmas’, *Physics of Plasmas* **20**(4), 042306.
- Carbajal, L., Dendy, R. O., Chapman, S. C. et al. [2014], ‘Linear and nonlinear physics of the magnetoacoustic cyclotron instability of fusion-born ions in relation to ion cyclotron emission’, *Physics of Plasmas* **21**(1), 012106.
- CCFE [2014], ‘It is T time for JET’, *Newsletter* (Retrieved 2015-09-03. http://www.ccf.ac.uk/news_detail.aspx?id=277).
- Chapman, S. C., Dendy, R. O., Todd, T. N. et al. [2014], ‘Relationship of edge localized mode burst times with divertor flux loop signal phase in JET’, *Physics of Plasmas* **21**(6), 062302.
- Chapman, S. C., Dendy, R. O., Todd, T. N. et al. [2015], ‘The global build-up to intrinsic edge localized mode bursts seen in divertor full flux loops in JET’, *Physics of Plasmas* **22**(7), 072506.
- Colella, P. [1990], ‘Multidimensional upwind methods for hyperbolic conservation laws’, *Journal of Computational Physics* **87**(1), 171–200.
- Connor, J. W. [1998], ‘A review of models for ELMs’, *Plasma Physics and Controlled Fusion* **40**(2), 191–213.

- Courant, R., Friedrichs, K. and Lewy, H. [1928], ‘Über die partiellen Differenzengleichungen der mathematischen Physik’, *Mathematische Annalen* **100**(1), 32–74.
- De la Luna, E., Sartori, F., Lomas, P. et al. [2009], Magnetic ELM Triggering Using the Vertical Stabilization Controller in JET, *in* ‘36th EPS Conference on Plasma Physics’.
- Degeling, A. W., Martin, Y. R., Bak, P. E. et al. [2001], ‘Dynamics of edge localized modes in the TCV tokamak’, *Plasma Physics and Controlled Fusion* **43**(12), 1671–1698.
- Degeling, a. W., Martin, Y. R., Lister, J. B. et al. [2003], ‘Magnetic triggering of ELMs in TCV’, *Plasma Physics and Controlled Fusion* **45**(9), 1637–1655.
- Dendy, R. O., Chapman, S. C. and Paczuski, M. [2007], ‘Fusion, space and solar plasmas as complex systems’, *Plasma Physics and Controlled Fusion* **49**(5A), A95–A108.
- Devine, P. E. and Chapman, S. C. [1996], ‘Self-consistent simulation studies of non-linear electron-whistler wave-particle interactions’, *Physica D: Non-linear Phenomena* **95**(1), 35–49.
- D’Ippolito, D. A. and Myra, J. R. [2003], ‘Blob stability and transport in the scrape-off-layer’, *Physics of Plasmas* **10**(10), 4029.
- D’Ippolito, D. A. and Myra, J. R. [2006], ‘Thermal transport catastrophe and the tokamak edge density limit’, *Physics of Plasmas* **13**(6), 062503.
- D’Ippolito, D. A., Myra, J. R. and Krasheninnikov, S. I. [2002], ‘Cross-field blob transport in tokamak scrape-off-layer plasmas’, *Physics of Plasmas* **9**(1), 222.
- D’Ippolito, D. A., Myra, J. R. and Zweben, S. J. [2011], ‘Convective transport by intermittent blob-filaments: Comparison of theory and experiment’, *Physics of Plasmas* **18**(6), 060501.
- Drake, J. F. [1995], *Physics of the Magnetopause*, Vol. 90 of *Geophysical Monograph Series*, American Geophysical Union.

- Fenstermacher, M. E., Xu, X. Q., Joseph, I. et al. [2013], ‘Fast pedestal, SOL and divertor measurements from DIII-D to validate BOUT++ nonlinear ELM simulations’, *Journal of Nuclear Materials* **438**, 346–350.
- Fenstermacher, M., Osborne, T., Leonard, A. et al. [2005], ‘Structure, stability and ELM dynamics of the H-mode pedestal in DIII-D’, *Nuclear Fusion* **45**(12), 1493–1502.
- Freidberg, J. P. [2007], *Plasma Physics and Fusion Energy*, Cambridge University Press.
- Friedman, A., Parker, S., Ray, S. et al. [1991], ‘Multi-scale particle-in-cell plasma simulation’, *Journal of Computational Physics* **96**(1), 54–70.
- Fundamenski, W., Militello, F., Moulton, D. et al. [2012], ‘A new model of the L-H transition in tokamaks’, *Nuclear Fusion* **52**(6), 062003.
- Furno, I., Labit, B., Podestà, M. et al. [2008], ‘Experimental Observation of the Blob-Generation Mechanism from Interchange Waves in a Plasma’, *Physical Review Letters* **100**(5), 055004.
- Garbet, X., Laurent, L., Roubin, J.-P. et al. [1991], ‘A model for the turbulence in the scrape-off layer of tokamaks’, *Nuclear Fusion* **31**(5), 967–972.
- Garcia, O. E., Horacek, J., Pitts, R. A. et al. [2006], ‘Interchange turbulence in the TCV scrape-off layer’, *Plasma Physics and Controlled Fusion* **48**(1), L1–L10.
- Gingell, P. W., Chapman, S. C. and Dendy, R. O. [2013], ‘Plasma heating by ion gyro-scale blobs in the kinetic and fluid regimes’, *Plasma Physics and Controlled Fusion* **55**(5), 055010.
- Gingell, P. W., Chapman, S. C., Dendy, R. O. et al. [2012], ‘Transport and evolution of ion gyro-scale plasma blobs in perpendicular magnetic fields’, *Plasma Physics and Controlled Fusion* **54**(6), 065005.
- Gollub, J. P. and Benson, S. V. [1980], ‘Many routes to turbulent convection’, *Journal of Fluid Mechanics* **100**(03), 449.

- Gollub, J. P. and Swinney, H. L. [1975], ‘Onset of Turbulence in a Rotating Fluid’, *Physical Review Letters* **35**(14), 927–930.
- Goodall, D. [1982], ‘High speed cine film studies of plasma behaviour and plasma surface interactions in tokamaks’, *Journal of Nuclear Materials* **111-112**, 11–22.
- Gorbunov, E. P. and Razumova, K. A. [1964], ‘Effect of a strong magnetic field on the magnetohydrodynamic stability of a plasma and the confinement of charged particles in the Tokamak machine’, *Journal of Nuclear Energy. Part C, Plasma Physics, Accelerators, Thermonuclear Research* **6**(5), 515–525.
- Gormezano, C., Challis, C. D., Joffrin, E. et al. [2008], ‘Chapter 4 Advanced Tokamak Scenario Development At Jet’, *Fusion Science and Technology* **53**(May).
- Greenhough, J., Chapman, S. C., Dendy, R. O. et al. [2003], ‘Probability distribution functions for ELM bursts in a series of JET tokamak discharges’, *Plasma Physics and Controlled Fusion* **45**(5), 747–758.
- Harned, D. S. [1982], ‘Quasineutral hybrid simulation of macroscopic plasma phenomena’, *Journal of Computational Physics* **47**(3), 452–462.
- Helander, P., Akers, R. J., Valovič, M. et al. [2005], ‘The effect of non-inductive current drive on tokamak transport’, *Plasma Physics and Controlled Fusion* **47**(12B), B151–B163.
- Hill, D. [1997], ‘A review of ELMs in divertor tokamaks’, *Journal of Nuclear Materials* **241-243**, 182–198.
- Hockney, R. W. and Eastwood, J. W. [1988], *Computer Simulation Using Particles*, Vol. 25.
- Horton, L., Vlasses, G., Andrew, P. et al. [1999], ‘Studies in JET divertors of varied geometry. I: Non-seeded plasma operation’, *Nuclear Fusion* **39**(1), 1–17.
- Huijsmans, G. T. A., Chang, C. S., Ferraro, N. et al. [2015], ‘Modelling of edge localised modes and edge localised mode control’, *Physics of Plasmas* **22**(2), 021805.

- IEA [2011], ‘World Energy Outlook 2011’, *International Energy Agency* (Retrieved 2015-08-24. <http://www.worldenergyoutlook.org/publications/weo-2011/>).
- Ikonen, T. and Dumbrajs, O. [2005], ‘Search for deterministic chaos in ELM time series of ASDEX upgrade Tokamak’, *IEEE Transactions on Plasma Science* **33**(3), 1115–1122.
- Jacquinet, J., Bhatnagar, V., Cordey, J. et al. [1999], ‘Overview of ITER physics deuterium-tritium experiments in JET’, *Nuclear Fusion* **39**(2), 235–253.
- Ju, M., Kim, J. and Team, K. [2000], ‘A predictive study of non-inductive current driven KSTAR tokamak discharge modes using a new transport/heating simulation package’, *Nuclear Fusion* **40**(11), 1859–1866.
- Kamiya, K., Asakura, N., Boedo, J. et al. [2007], ‘Edge localized modes: recent experimental findings and related issues’, *Plasma Physics and Controlled Fusion* **49**(7), S43–S62.
- Kirk, A., Chapman, I., Liu, Y. et al. [2013], ‘Understanding edge-localized mode mitigation by resonant magnetic perturbations on MAST’, *Nuclear Fusion* **53**(4), 043007.
- Klinger, T., Latten, A., Piel, A. et al. [1997], ‘Chaos and turbulence studies in low beta plasmas’, *Plasma Physics and Controlled Fusion* **39**(12B), B145–B156.
- Kojima, A., Oyama, N., Sakamoto, Y. et al. [2009], ‘Fast dynamics of type I and grassy ELMs in JT-60U’, *Nuclear Fusion* **49**(11), 115008.
- Krasheninnikov, S. I. [2001], ‘On scrape off layer plasma transport’, *Physics Letters A* **283**(5-6), 368–370.
- Krasheninnikov, S. I., D’Ippolito, D. A. and Myra, J. R. [2008], ‘Recent theoretical progress in understanding coherent structures in edge and SOL turbulence’, *Journal of Plasma Physics* **74**(05), 679–717.

- Krashennnikov, S. I., Pigarov, A. Y., Galkin, S. A. et al. [2003], Blobs and Cross-Field Transport in the Tokamak Edge Plasmas, *in* ‘19th Fusion Energy Conference 14 - 19 October 2002 Lyon, France’, pp. 4–1.
- Lang, P., Alonso, A., Alper, B. et al. [2011], ‘ELM pacing investigations at JET with the new pellet launcher’, *Nuclear Fusion* **51**(3), 033010.
- Lang, P., Loarte, a., Saibene, G. et al. [2013], ‘ELM control strategies and tools: status and potential for ITER’, *Nuclear Fusion* **53**(4), 043004.
- Lang, P. T., Alper, B., Baylor, L. R. et al. [2002], ‘High density operation at JET by pellet refuelling’, *Plasma Physics and Controlled Fusion* **44**(9), 1919–1928.
- Layne, R., Capel, A., Cook, N. et al. [2012], ‘Long term preservation of scientific data: Lessons from jet and other domains’, *Fusion Engineering and Design* **87**(12), 2209–2212.
- Layne, R. and Wheatley, M. [2002], ‘New data storage and retrieval systems for JET data’, *Fusion Engineering and Design* **60**(3), 333–339.
- Lennholm, M., Beaumont, P., Carvalho, I. et al. [2015], ‘ELM frequency feedback control on JET’, *Nuclear Fusion* **55**(6), 063004.
- Libchaber, A., Fauve, S. and Laroche, C. [1983], ‘Two-parameter study of the routes to chaos’, *Physica D: Nonlinear Phenomena* **7**(1-3), 73–84.
- Lipatov, A. [2002], *The hybrid multiscale simulation technology: an introduction with application to space and plasma physics*, Springer.
- Litaudon, X., Crisanti, F., Alper, B. et al. [2002], ‘Towards fully non-inductive current drive operation in JET’, *Plasma Physics and Controlled Fusion* **44**(7), 1057–1086.
- Lönnroth, J.-S., Parail, V. V., Corrigan, G. et al. [2003], ‘Integrated predictive modelling of the effect of neutral gas puffing in ELMy H-mode plasmas’, *Plasma Physics and Controlled Fusion* **45**(9), 1689–1711.

- Maqueda, R., Stotler, D. and Zweben, S. [2011], ‘Intermittency in the scrape-off layer of the National Spherical Torus Experiment during H-mode confinement’, *Journal of Nuclear Materials* **415**(1), S459–S462.
- Martin, Y. R., Degeling, A. W. and Lister, J. B. [2002], ‘Search for determinism in ELM time series in TCV’.
- Matsoukis, S., Chapman, S. C. and Rowlands, G. [2000], ‘Does stochasticity due to whistler mode wave coupling persist in self-consistent systems?’, *Physica D: Nonlinear Phenomena* **138**(3-4), 251–266.
- Matthews, A. P. [1994], ‘Current Advance Method and Cyclic Leapfrog for 2D Multispecies Hybrid Plasma Simulations’, *Journal of Computational Physics* **112**(1), 102–116.
- McBride, V. A., Wilms, J., Kreykenbohm, I. et al. [2007], ‘On the cyclotron line in Cepheus X-4’, *Astronomy and Astrophysics* **470**(3), 1065–1070.
- McDonald, D. C., Andrew, Y., Huysmans, G. T. A. et al. [2008], ‘Chapter 3: ELMy H-Mode Operation in JET’, *Fusion Science and Technology* **53**(4), 891–957.
- Murari, A., Pisano, F., Vega, J. et al. [2014], ‘Extensive statistical analysis of ELMs on JET with a carbon wall’, *Plasma Physics and Controlled Fusion* **56**(11), 114007.
- Myra, J. R. [2007], ‘Current carrying blob filaments and edge-localized-mode dynamics’, *Physics of Plasmas* **14**(10), 102314.
- Myra, J. R. and D’Ippolito, D. A. [2005], ‘Edge instability regimes with applications to blob transport and the quasicohherent mode’, *Physics of Plasmas* **12**(9), 092511.
- Myra, J. R., D’Ippolito, D. A., Stotler, D. P. et al. [2006], ‘Blob birth and transport in the tokamak edge plasma: Analysis of imaging data’, *Physics of Plasmas* **13**(9), 092509.
- Myra, J. R., D’Ippolito, D. A., Xu, X. Q. et al. [2000*a*], ‘Resistive modes in the edge and scrape-off layer of diverted tokamaks’, *Physics of Plasmas* **7**(11), 4622.

- Myra, J. R., D'Ippolito, D. A., Xu, X. Q. et al. [2000*b*], ‘Resistive X-point modes in tokamak boundary plasmas’, *Physics of Plasmas* **7**(6), 2290.
- Myra, J. R., Russell, D. A. and D'Ippolito, D. A. [2008], ‘Transport of perpendicular edge momentum by drift-interchange turbulence and blobs’, *Physics of Plasmas* **15**(3), 032304.
- Myra, J. R., Russell, D. A. and D'Ippolito, D. A. [2012], ‘Diffusive-convective transition for scrape-off layer transport and the heat-flux width’, *Plasma Physics and Controlled Fusion* **54**(5), 055008.
- Naulin, V. [2007], ‘Turbulent transport and the plasma edge’, *Journal of Nuclear Materials* **363-365**(1-3), 24–31.
- Nave, M. F. F., Lomas, P., Gowers, C. et al. [2000], ‘Plasma current dependence of the edge pedestal height in JET ELM-free H-modes’, *Plasma Physics and Controlled Fusion* **42**(5A), A89–A96.
- Newhouse, S., Ruelle, D. and Takens, F. [1978], ‘Occurrence of strange Axiom A attractors near quasiperiodic flows on T^m , $m \geq 3$ ’, *Communications in Mathematical Physics* **64**(1), 35–40.
- Ongena, J. and Oost, G. V. [2012], ‘Energy for Future Centuries: Prospects for Fusion Power as a Future Energy Source’, *Fusion Science and Technology* **61**(2T), 3–16.
- Pamela, J., Ongena, J. and Contributors, J.-E. [2005], ‘Overview of JET results’, *Nuclear Fusion* **45**(10), S63–S85.
- Pamela, S. J. P., Huysmans, G. T. A., Beurskens, M. N. A. et al. [2011], ‘Non-linear MHD simulations of edge-localized-modes in JET’, *Plasma Physics and Controlled Fusion* **53**(5), 054014.
- Pipa, G., Grün, S. and van Vreeswijk, C. [2013], ‘Impact of spike train auto-structure on probability distribution of joint spike events’, *Neural computation* **25**(5), 1123–63.
- Pitzschke, A., Behn, R., Sauter, O. et al. [2012], ‘Electron temperature and density profile evolution during the edge-localized mode cycle in ohmic and

- electron cyclotron-heated H-mode plasmas in TCV', *Plasma Physics and Controlled Fusion* **54**(1), 015007.
- Pritchett, P. [2000], 'Particle-in-cell simulations of magnetosphere electrodynamics', *IEEE Transactions on Plasma Science* **28**(6), 1976–1990.
- Raffray, A. R., Akiba, M., Chuyanov, V. et al. [2002], 'Breeding blanket concepts for fusion and materials requirements', *Journal of Nuclear Materials* **307-311**(1 SUPPL.), 21–30.
- Romanelli, F. [2012], EFDA, Fusion Electricity: A roadmap to the realisation of fusion energy, Technical report.
URL: <https://www.euro-fusion.org/eurofusion/the-road-to-fusion-electricity/>
- Rozhansky, V. and Kirk, A. [2008], 'Possible mechanism for filament motion in the SOL of a tokamak', *Plasma Physics and Controlled Fusion* **50**(2), 025008.
- Ruelle, D. and Takens, F. [1971], 'On the nature of turbulence', *Communications in Mathematical Physics* **20**(3), 167–192.
- Saibene, G., Horton, L., Sartori, R. et al. [1999], 'The influence of isotope mass, edge magnetic shear and input power on high density ELMy H modes in JET', *Nuclear Fusion* **39**(9), 1133–1156.
- Sakharov, A. D. [1958], *Fizika Plazmy i Problema Upravlyaemykh Termoyadernykh Reaktsii (Plasma Physics and the Problem of Controlled Thermo-nuclear Reactions)*, translated edn, Pergamon Press 1961.
- Saltzman, J. [1994], 'An Unsplit 3D Upwind Method for Hyperbolic Conservation Laws', *Journal of Computational Physics* **115**(1), 153–168.
- Sartori, F., Lomas, P., Piccolo, F. et al. [2008], Synchronous ELM Pacing at JET Using the Vertical Stabilisation Controller, in '35th EPS Conference on Plasma Physics', p. 5.045.
- Sauthoff, N., Von Goeler, S. and Stodiek, W. [1978], 'A study of disruptive instabilities in the PLT tokamak using X-ray techniques', *Nuclear Fusion* **18**(10), 1445–1458.

- Schreiber, T. and Schmitz, A. [2000], ‘Surrogate time series’, *Physica D: Non-linear Phenomena* **142**(3-4), 346–382.
- Schulz, N. S., Kahabka, P. and Zinnecker, H. [1995], ‘A new outburst of the transient X-ray pulsar Cephei X-4’, *Astronomy and Astrophysics (ISSN 0004-6361)* **295**, 413–419.
- Singh, R., Kaw, P., Diamond, P. et al. [2012], ‘A model for the power required to access the H-mode in tokamaks and projections for ITER’, *Proceedings 24th IAEA FEC, San Diego 8-13 October 2012*.
- Stix, T. H. [1997], *Waves in Plasmas*, 1992 edn, American Institute of Physics.
- Strachan, J. D., Batha, S., Beer, M. et al. [1997], ‘TFTR DT experiments’, *Plasma Physics and Controlled Fusion* **39**(12B), B103–B114.
- Swanson, D. G. [2003], ‘Plasma Waves (2nd edition)’, *Plasma Physics and Controlled Fusion* **45**(6), 1069–1069.
- Terry, J. L., Zweben, S. J., Hallatschek, K. et al. [2003], ‘Observations of the turbulence in the scrape-off-layer of Alcator C-Mod and comparisons with simulation’, *Physics of Plasmas* **10**(5), 1739.
- Thomas, P. R., Andrew, P., Balet, B. et al. [1998], ‘Observation of Alpha Heating in JET DT Plasmas’, *Physical Review Letters* **80**(25), 5548–5551.
- Trefethen, L. N., Trefethen, A. E., Reddy, S. C. et al. [1993], ‘Hydrodynamic Stability Without Eigenvalues’, *Science* **261**(5121), 578–584.
- Treumann, R. A. and Baumjohann, W. [1997], *Advanced Space Plasma Physics*, Imperial College Press.
- Valovic, M., Rapp, J., Cordey, J. G. et al. [2002], ‘Long timescale density peaking in JET’, *Plasma Physics and Controlled Fusion* **44**(9), 1911–1917.
- Von Goeler, S., Stodiek, W. and Sauthoff, N. [1974], ‘Studies of Internal Disruptions and $m = 1$ Oscillations in Tokamak Discharges with Soft-X-Ray Techniques’, *Physical Review Letters* **33**(20), 1201–1203.

- Wagner, F., Becker, G., Behringer, K. et al. [1982], ‘Regime of Improved Confinement and High Beta in Neutral-Beam-Heated Divertor Discharges of the ASDEX Tokamak’, *Physical Review Letters* **49**(19), 1408–1412.
- Webster, A. [2012], ‘Edge Localised Plasma Instabilities in the Joint European Torus (JET) Acknowledgements :’.
- Webster, A. J. and Dendy, R. O. [2013], ‘Statistical Characterization and Classification of Edge-Localized Plasma Instabilities’, *Physical Review Letters* **110**(15), 155004.
- Webster, A. J., Dendy, R. O., Calderon, F. A. et al. [2014], ‘Time-resonant tokamak plasma edge instabilities?’, *Plasma Physics and Controlled Fusion* **56**(7), 075017.
- Wesson, J. [2004], *Tokamaks*, third edn, Oxford University Press.
- Wilson, H. R., Cowley, S. C., Kirk, a. et al. [2006], ‘Magneto-hydrodynamic stability of the H-mode transport barrier as a model for edge localized modes: an overview’, *Plasma Physics and Controlled Fusion* **48**(5A), A71–A84.
- Winske, D. [1985], ‘Hybrid simulation codes with application to shocks and upstream waves’, *Space Science Reviews* **42**(1-2), 53–66.
- Winske, D. and Omid, N. [1996], ‘A nonspecialist's guide to kinetic simulations of space plasmas’, *Journal of Geophysical Research* **101**(A8), 17287.
- Winske, D. and Quest, K. B. [1988], ‘Magnetic field and density fluctuations at perpendicular supercritical collisionless shocks’, *Journal of Geophysical Research* **93**(A9), 9681.
- WNA [2015], ‘Nuclear Power in Germany’, *World Nuclear Association* (Retrieved 2015-08-24. <http://www.world-nuclear.org/info/country-profiles/countries-g-n/germany/>).
- Xu, G., Naulin, V., Fundamenski, W. et al. [2009], ‘Blob/hole formation and zonal-flow generation in the edge plasma of the JET tokamak’, *Nuclear Fusion* **49**(9), 092002.

- Xu, X. Q., Cohen, R. H., Rognlien, T. D. et al. [2000], ‘Low-to-high confinement transition simulations in divertor geometry’, *Physics of Plasmas* **7**(5), 1951.
- Yee, K. S. [1966], ‘Numerical solution of initial boundary value problems involving maxwell's equations in isotropic media’, *IEEE Transactions on Antennas and Propagation* **14**(3), 302–307.
- Yu, G. Q. and Krasheninnikov, S. I. [2003], ‘Dynamics of blobs in scrape-off-layer/shadow regions of tokamaks and linear devices’, *Physics of Plasmas* **10**(11), 4413.
- Zohm, H. [1996], ‘Edge localized modes (ELMs)’, *Plasma Physics and Controlled Fusion* **38**(2), 105–128.
- Zvejnieks, G., Kuzovkov, V. N., Dumbrajs, O. et al. [2004], ‘Autoregressive moving average model for analyzing edge localized mode time series on Axially Symmetric Divertor Experiment (ASDEX) Upgrade tokamak’, *Physics of Plasmas* **11**(12), 5658.